KfK 4418
EUR 10541e
Juli 1988

Nuclear Fusion Project Semi-annual Report of the Association KfK/EURATOM

October 1987 - March 1988

Projekt Kernfusion

Kernforschungszentrum Karlsruhe

KfK 4418
EUR 10541e

Nuclear Fusion Project Semi-annual Report of the Association KfK/EURATOM

October 1987 - March 1988

compiled by
G. Kast

Kernforschungszentrum Karlsruhe GmbH

Kernforschungszentrum Karlsruhe GmbH
Postfach 3640, 7500 Karlsruhe 1

ISSN 0303-4003

Contents

B1 Blanket Design Studies

Two design concepts are studied by KfK: a helium-cooled ceramic blanket and a blanket with Pb-17Li eutectic as breeder material and coolant. The study includes small-scale experiments and collaboration with industry for special feasibility problems. The studies are coordinated with efforts of CEA and UKAEA in a common working group.

In both of the designs blanket and first wall (F.W.) form a unit with a common coolant flow. Thus, the first wall studies are included here and described in more detail under task N 1, Plasma Facing Components.

1. Helium-cooled Ceramic Breeder Blanket

In spite of the fact that in NET blanket test objects will only be inserted as outboard segments or subsegments a study has been conducted on an inboard blanket including a divertor.

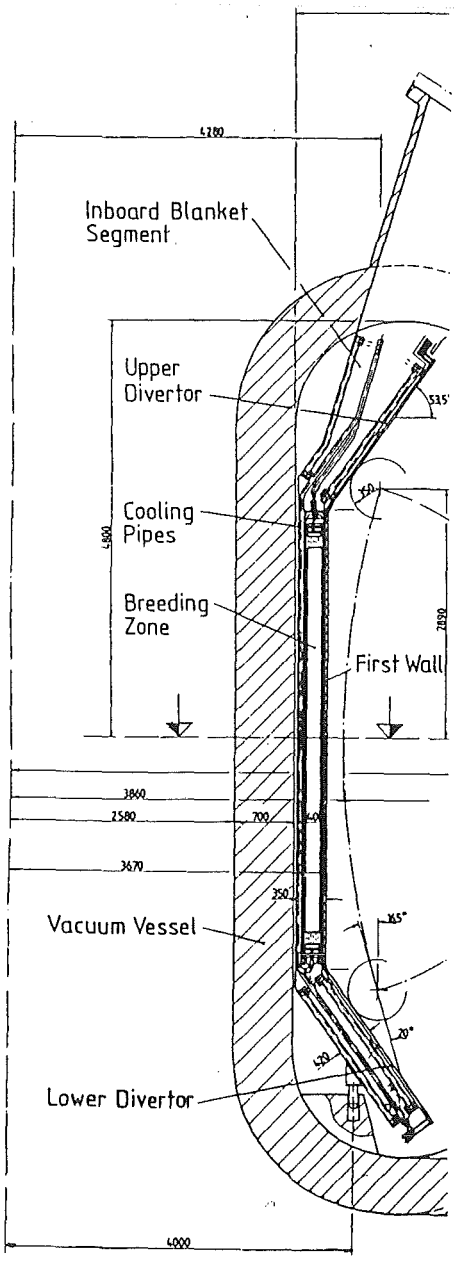

Fig. 1: NET-DN cross section inboard blanket

This was done in order to assess the technical feasibility and to identify the engineering problems. In addition, an inboard blanket concept is needed to confirm the DEMO relevance of the concept.

Fig. 1 gives a general view of the inboard blanket. Two separate cooling systems are foreseen, a high-pressure system (about 9 MPa) for cooling in series upper divertor, first wall and lower divertor, and a low-pressure system (6 MPa) for cooling the blanket. The supply tubes are running on the back side of the structure with coolant inlet at the bottom. The principle of the inboard blanket with poloidally running tubes was described in the last but one progress report (KfK 4276). Two separate coolant loops are foreseen for the blanket cooling, which are alternately connected to the coolant tubes in a row. This guarantees afterheat removal is case of failure of one of the coolant loops. Manifolding is done via distributor plates. The same principle was used for the first wall and divertors.

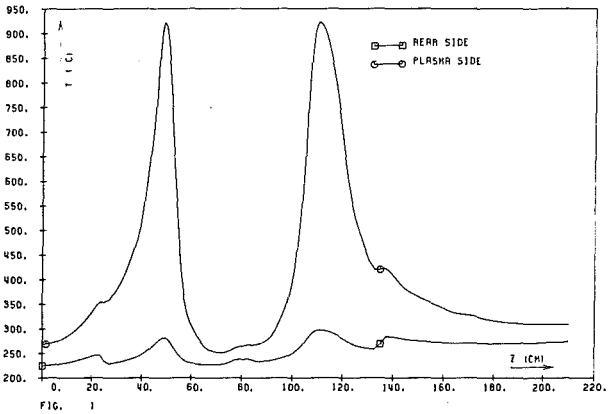

Fig. 2: Temperature distribution on the upper divertor plate

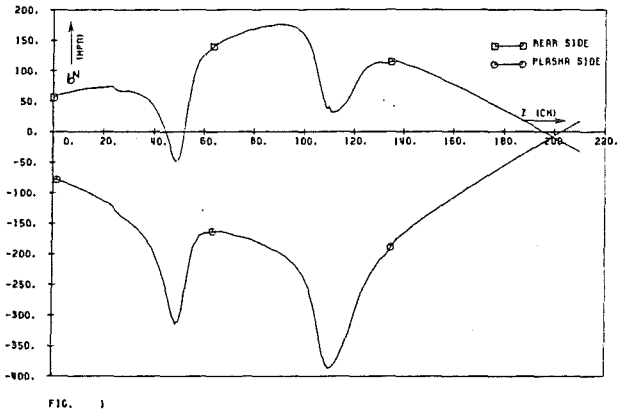

Fig. 3: TZM thermal stresses parallel to the coolant channel

The divertor plate consists of poloidally arranged molybdenum bars with one coolant channel each and was described in the progress report KfK 4165. Stress calculations with the computer code ABAQUS have been performed. Fig. 2 shows the temperature distribution of the

Breeding material:	0.5 mm Li_4SiO_4 pebbles (total weight = 20 t)
Li6 enrichment:	90 %
Multiplier:	beryllium (total weight = 90 t)
First wall protection:	graphite tiles 20 mm thick inboard and 15 mm thick outboard
Blanket form:	poloidal inboard and with canisters outboard
Tritium breeding ratio:	1.04 (3 dimen. calc.), 1.37 (1 dimens. calc.)
Tritium production rate.	96 g/d
Total blanket power:	540 MW + 134 MW in the shields + 142 MW in the divertors
Nominal heat flux on the first wall:	10 W/cm²
Max. local heat flux on first wall:	40 W/cm² (outboard)
Helium coolant pressure:	6 MPa (blanket), 8 MPa or 9 MPa in divertors
F.W. and blanket helium pressure drops:	0.21 MPa
F.W. and blanket helium inlet and outlet temp.:	200 °C and 450 °C
F.W. max. steel temp.:	511 °C
Max. equiv. thermal stress in F.W. steel:	325 MPa
Max. temp. of graphite tiles:	1650 °C
Max. temp. in the blanket steel pressure tubes:	480 °C
Max. temp. in beryllium:	480 °C
Max. temp. at beryllium - pebble bed interface:	480 °C
Max. temp. in pebble bed:	600 °C
Min. temp. in pebble bed:	300 °C
Max. temp. in divertor (TZM):	925 °C
Max. equiv. thermal stress in TZM:	385 MPa
Helium pressure in purge flow system:	0.1 MPa
Tritium inventory in Li_4SiO_4 pebbles:	250 g (o.1 % H_2 in purge helium)

Total tritium losses from plant < 10 Ci/d (oxidizing atmosph. in helium main circuit).

Table 1 : Main characteristics to the ceramic blanket for NET

upper divertor plate where the helium inlet temperature in the divertor cooling tubes is the highest (203°C).

The dominant thermal stresses which are in poloidal direction are shown on Fig. 3. They correspond to an optimum system of supports. The maximum of Mises stress of 385 MPa is probably acceptable for TZM at tempertures below 1100°C.

Three-dimensional Monte Carlo calculations were made for the shielding requirements in the divertor region. 7 cm steel equivalent is needed in NET behind the divertor structure.

The design of the outboard blanket was also slightly modified and detailed. Fig. 4 shows the most recent canister design. The main characteristics of the blanket are summarized in Table 1.

A comprehensive description of the helium-cooled ceramic breeder blanket is given in /1/ with a shorter version in /2/. The results of the neutronics analysis are described in /3/ and /4/.

Staff:

E.Bojarsky, M. Dalle Donne, U. Fischer, M. Küchle, P.Norajitra, H. Reiser, G. Schumacher, G. Sordon

2. Liquid Metal Cooled Blanket

The development of a self-cooled blanket in which the same liquid metal (Pb-17Li) serves as both tritium breeder and coolant has been continued. Work has been concentrated mainly on the investigation of the thermo-mechanical behavior of an outboard blanket. In co-operation with the NIS-Ingenieurgesellschaft mbH, a stress analysis is being performed which consists of a two-step procedure.

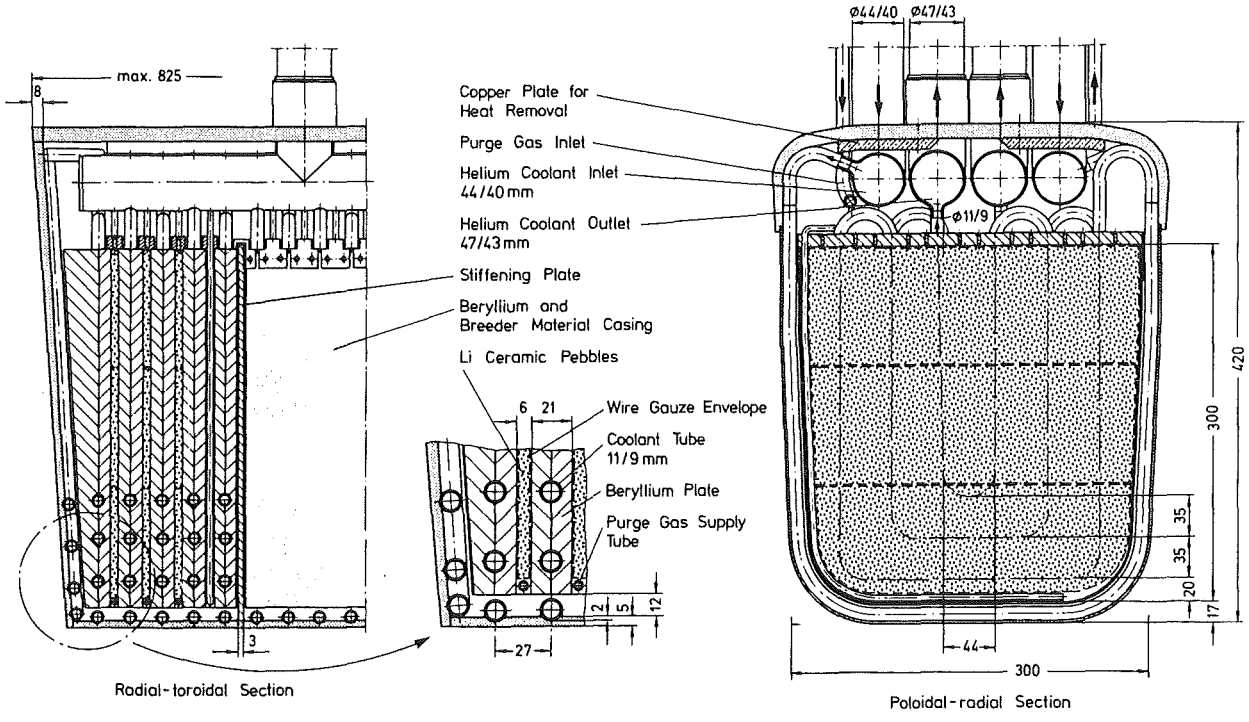

Fig. 4: Canister design

The first step was carried out to identify regions of critical stress. The results of the global analysis have led to a number of design changes which were reported already in the semi-annual report KfK 4276.

After using simple and rather conservative analytical models in the first step, phase A of the second step has been performed using thermo-elastical theory. For that purpose, a representative poloidal sector of an outboard blanket segment has been modelled by finite elements (FE). Stress distributions and displacements have been calculated by utilizing the SHELL-5 computer code. In addition, the corrugated first wall has been described by a fine FE-mesh. Loadings considered in the present study are mainly those due to coolant pressure and temperature gradients caused by surface heat flux and volumetric nuclear heating.

	length m	average velocity m/s	bulk temp. rise K	MHD pressure drop MPa
poloidal inlet channels	7.0	0.7	5	0.25
poloidal outlet channels	7.0	0.6	20	0.6
toroidal front channels	0.8	0.9 (1.8 max.)	50	0.3 (incl. bends)
U-turn at bottom end	---	0.6 - 0.7	--	0.1
access tubes inlet outlet	4.0 4.0	1.2 1.2	0 0	0.4 0.4
total			75	2.05 (1.25 in blanket)

Table 2: Key data of thermal-hydraulic and pressure drop analyses

The structural analysis received input from thermal and MHD analyses. Details are given in Table 2 based on current understanding and requirements for the modified outboard blanket segment.

The stresses so far computed for steady state conditions have been categorized as primary and secondary stresses. Multi-axial stress states have been evaluated and compared with the relevant ASME criteria for austenitic stainless steels, i.e. AISI 316L.

The stress analysis has led to the following results:

- Behavior of the total segment
  The blanket segment is fixed at its top end. The total bending at the bottom end amounts to about 6 mm due to internal pressure loading. This value is relatively unimportant in comparison to the thermal bending which causes a radial displacement of about 40 mm. A complete suppression of the thermal deformation would result in a total poloidal bending stress of about 82 MPa.
- Local stresses
  The box structure formed by the individual toroidal front channels is subject to bending forces and shear stresses. Following ASME/Tresca, the resulting stresses are mostly of secondary nature. At the plasma-facing summit of the corrugated first wall, the maximum resulting stress reaches a value of about 500 MPa.
  The equivalent stress in the diagonally oriented separating walls between the poloidal outlet channels amounts to 175 MPa.
  In the remaining part of the structure, as expected, stress levels do not become critical because of smaller temperature differences and the absence of wall thickness limitations.

So far the results of this study reflect the suitability of the present blanket design. On that basis, life-time predictions of the blanket will be made when operated in a cyclic mode. This problem will be the subject of future investigations (phase B of the second step of the structural analysis).

Tritium Removal from NaK by Cold Trapping

The selected tritium removal technique for the self-cooled Pb-17Li blanket with an intermediate NaK loop consists of tritium permeation into the NaK and precipitation as tritide in a cold trap. For tritium recovery, the cold trap is heated up and the tritium is pumped off.

Presently, the test loop for hydrogen (protium) precipitation is built up. In the following, experiments are described to recover the hydrogen by thermal decomposition of the hydride.

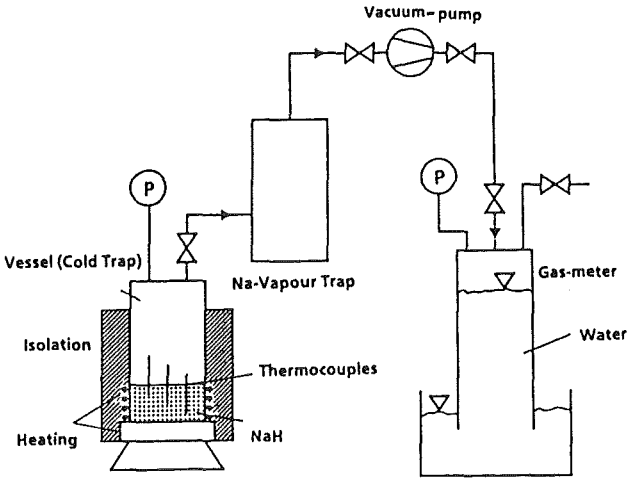

Fig. 5: Apparatus for decomposition of NaH-powder

In these screening tests, NaK was replaced by Na. In a first step, NaH-powder was decomposed in an electrically heated vessel (see Fig. 5). In some experiments, NaH was mixed with Na_2O to investigate the influence of oxygen. The hydrogen release rate $\dot{m}$ was measured with the gas-meter. The rate constant k was defined by

$$\dot{m} = km^n$$

where m is the available hydrogen mass (as NaH) and the exponent n characterizes the order of the reaction. It was found that n is about unity and k is represented by a straight curve in the diagram shown in Fig. 6. This figure shows good agreement with previous work.

The specific surface of the NaH powder is expected to be different from that of NaH-crystals in cold traps. Therefore, in a second step, NaH-crystals were generated in the test facility shown in Fig. 7. The main part is the crystallizer

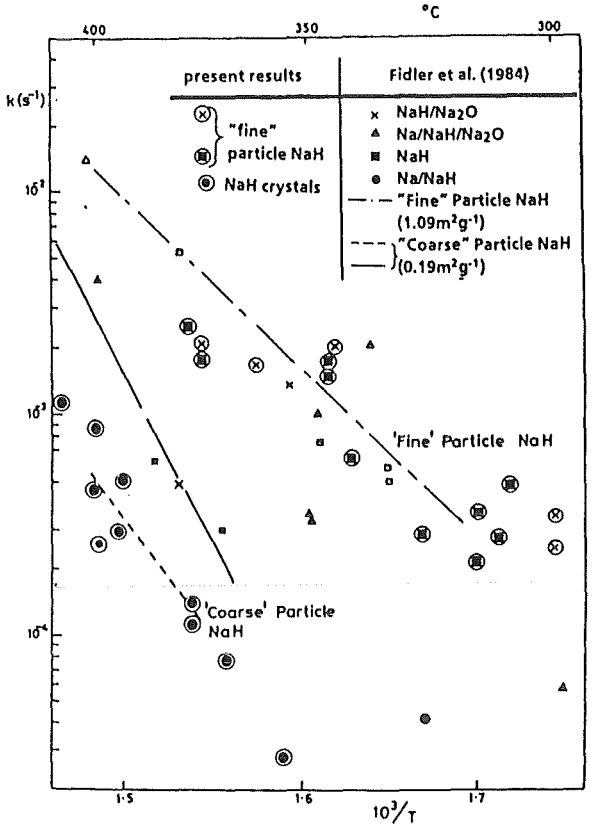

Fig. 6: Arrhenius plot of rate constant

which consists of a vessel which can be heated at the cylindrical wall and cooled at the bottom. An inner cylinder forms a thermal convection flow which transports the sodium from the interface to the bottom. Hydrogen is absorbed at the interface and crystals are expected to grow at the bottom. For hydrogen release, the cooling is switched off.

Figure 6 contains also results from these release experiments: the rate constant is smaller by more than one order of magnitude. The fitting curve agrees quite well with previous experiments using "coarse" NaH-powder.

The release at higher temperatures (T>350 °C) is characterized by hydrogen bubbling. Therefore, hydrogen diffusion in the sodium bulk does not appear to be a rate limiting step. The release rates should not differ significantly if the sodium is drained from the vessel.

Staff:
DI. K. Arheidt
H.J. Brinkmann
G. Eisele
DI. H. John
DI. S. Malang
Dr. J. Reimann
DI. K. Rust

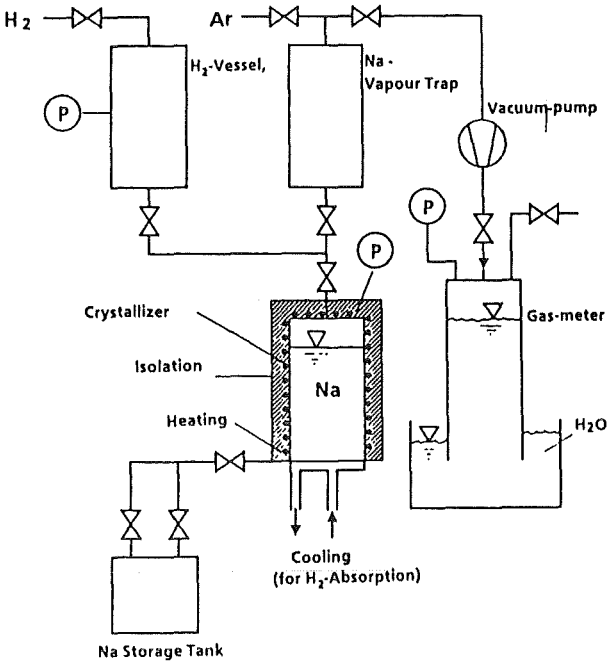

Fig. 7: Apparatus for generation and decomposition of NaH-crystals

References:

1. M. Dalle Donne et al. "Pebble Bed Canister: The Karlsruhe Ceramic Breeder Blanket Design for NET" submitted for publication in Fusion Technology

2. M. Dalle Donne et al. "The KfK-Design of a Helium Cooled Ceramic Blanket for NET" Intern. Symp. on Fusion Technology, Tokyo 10.-15.4.1988

3. U. Fischer "Multi-dimensional Neutronics Analysis of the Canister Blanket for NET" KfK-4255 (1987)

4. U. Fischer "Multi-dimensional Neutronics Analysis in the Double Null Configuration of NET" Intern. Symp. on Fusion Technology, Tokyo 10.-15.4.1988

B2 Development of Computational Tools for Neutronics

The KfK-activities to improve the computational tools for fusion neutronics comprise the evaluation and processing of relevant nuclear data, the development of new calculational procedures as well as the adoption of existing methods and programmes for use in fusion neutronics.

The efforts to develop a general anisotropic transport code system for a rigorous treatment of the neutron scattering have been f continued urther. At present the efforts are concentrated on the development of the two-dimensional transport module ANTRA 2. The numerical scheme, which had been developed for the one-dimensional module ANTRA 1, is now being introduced into the 2d-transport programme TWOTRAN . The Fortran -77 version of the TWOTRAN-code, adapted to the KfK programme system KAPROS, serves as basic version for the development of ANTRA2.

A study on the multiplication of 14-MeV neutrons in lead, based on the consistent use of lead double-differential cross-section data (DDX) from the European Fusion File EFF-1, has been completed and published /1/ . A major issue from this study has been the necessity for a reevaluation of the lead nuclear data involving an increased 14-Mev (n, 2n) - cross-section.

A study on the multiplication of 14-MeV neutrons in beryllium has been started. Again the DDX-data on EFF-1 and their consistent use in the transport calculation forms the basis of the study. The beryllium DDX-data on EFF-1 are based on the LANL-evaluation of P. Young and are stored in the so-called "pseudo-level" representation on the file. Therefore they can be processed by the SDXDDX-module that has been developed during the lead neutron multiplication study from the NJOY-code for processing the DDX-data for elastic and discrete-inelastic neutron scattering. First results (Table 3) indicate that with respect to the total neutron multiplication again there is no difference between the conventional transport calculations in the S_N / P_l approximation and the rigorous method using angle-discretized scattering matrices. This does not hold with respect to the spectral distribution of the leakage neutrons; thus there will be an impact on the neutronic performance of a fusion reactor blanket with a beryllium multiplier. Note, however, that the neutron multiplication calculated with the LANL-Be^9-data is lower by 8 to 15 % compared to calculations with ENDF/B-IV-data.

For fusion neutronics applications the Monte Carlo code MCNP is in use at KfK. The actual version 3A has been implemented now on the local computer Siemens 7890. The IBM-VS Fortran compiler has been used for compiling the source programme. In general the sample problems ran successfully. Minor problems were caused by errors in the data structure of the nuclear cross-section library. Severe data errors have been detected in some neutron emission spectra of the Livermore nuclear data library ENDL 85, which is part of the MCNP/3A data library.

The Monte Carlo code MCNP also has been used for the three-dimensional shielding analysis of NET. The shielding problems have been treated by means of the importance sampling technique with a limited expense of computing times. To check the reliability of the MCNP shielding calculations a one-dimensional shielding benchmark has been analyzed. MCNP shielding calculations have been proven to be very reliable, whereas S_N-calculations, using available group nuclear data, tend to overestimate the shielding effectiveness. The missing resonance shielding in the group constants seems to be the major source of this over-estimation: this is the subject of a more detailed analysis which is in progress.

The work concerning the preparation of a coupled neutron-photon group constant library for transport calculations has been continued. In this context the KfK-version of the NJOY-code has been tested and corrected with respect to the processing of photon production data.

As was reported previously, the spectra of neutrons produced by continuum inelastic scattering reactions with Cu have been calculated with KfK-codes that take into account pre-equilibrium processes. Satisfactory agreement was found between our calculated "test data" and a more recent

	shell thickness (cm)	4.5		13.5		19.9	
transport code	data base	L a)	M b)	L	M	L	M
ANTRA 1	EFF-1 (LANL)	1.29	1.31	1.80	1.90	2.01	2.19
ONETRAN	EFF-1 (LANL)	1.29	1.31	1.80	1.90	2.03	2.20
MCNP	LANL	1.28	1.31	1.79	1.90	1.99	2.20
ONETRAN	ENDF/B IV	1.38	1.42	2.06	2.23	2.27	2.58

Table 3:Neutron Multiplication in beryllium: Results from different transport calculations with different nuclear data.

a) L = neutron Leakage
b) M = total neutron multiplication

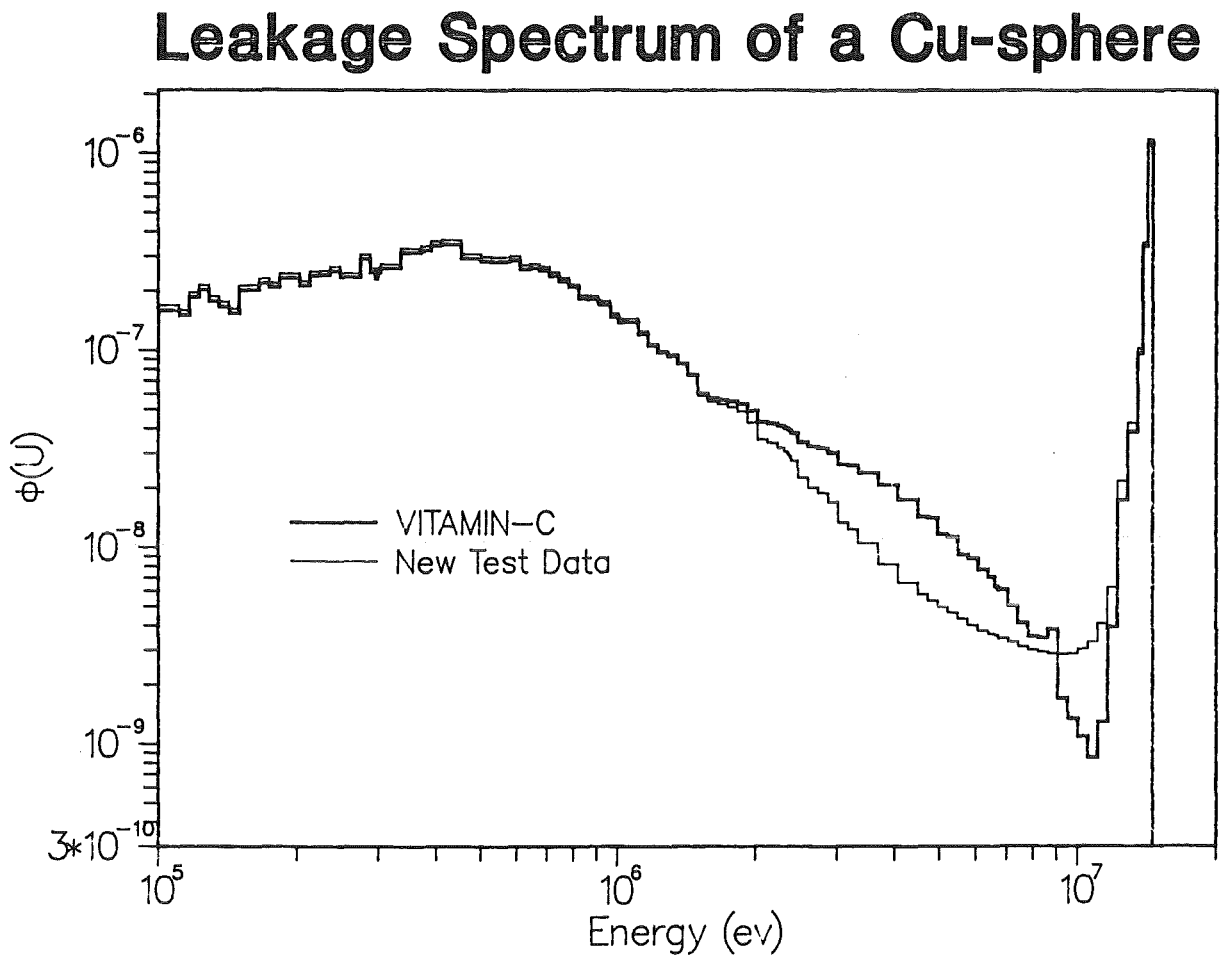

Table 4: Leakage Spectrum of a Cu-sphere

evaluation by H. Vonach, I RK Wien, that is based on experimental data.

We also anlyzed the impact of our "test data" on the leakage spectrum of a 14-MeV neutron source surrounded by a spherical copper shell of 18 cm thickness. The spectra shown in Table 4 have been obtained from a S_8/P_3-calculation with the KfK-version of the ONETRAN-code. The leakage spectrum calculated with the VITAMINC-data shows a depression in the energy region around 10 Mev. The same effect was found in the calculation using the EFF-1 data. The new "test data" clearly reduce this depression. This is due to high energy neutrons produced in pre-equilibrium processes, which probably have not been taken into account in both of the data files mentioned.

Publications:

[1] U Fischer, A. Schwenk-Ferrero, E. Wiegner: Neutron Multiplication in Lead: A Comparative Study Based on a New Calculational Procedure and New Nuclear Data, paper submitted to Int. Symp. FusionTechnology, Tokyo, Japan, 10-15 April, 1988.

Staff:

I. Broeders
U. Fischer
B. Krieg
H. Küsters
A. Schwenk-Ferrero
E. Stein
E. Wiegner

B 6 Corrosion of Structural Materials in Flowing Pb-17 Li

The loop PICOLO was constructed for corrosion studies of fusion reactor blanket materials in flowing Pb-17 Li.

The first run of PICOLO has been evaluated with respect to corrosion kinetics and phenomena of the specimens of the NET batch of steel 1.4914. The test parameters were:

Test temperature	550°C (823K)
Flow velocity	0.3 m/s
Reynolds number	20950
Temperature gradient	~ 250 K

The loss of material which is demonstrated in Fig. 6.1 can be expressed by the equation:

$$r\,(mm) = -0.0288 + 4.604 \cdot 10^{-5} \cdot t\,(h)$$

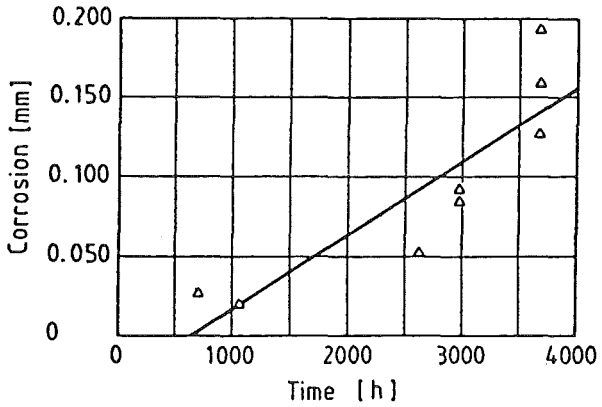

Fig.8: Loss of thickness of the specimens 1.4914 in flowing Pb-17 Li due to corrosion at 550°C

The choking of the loop after ~3700 h of operation was caused by the deposition of corrosion products in the cold leg of the loop. The magnetic precipitates were mainly deposited in the magnetic trap, the pump and the flow meter. Fig. 9 shows the size and auter appearance of such deposits in the magnetic trap. Chemical analyses indicate that the material of the trap contained around 10 vol % (~10,5 at -%) of the magnetic material (10 at -% Fe, 0.4 at -% Cr, 0.1 at -% Ni). The magnetic particles consisted mainly of iron and considerable amounts of chromiun. The visual properties of the crystals leads to the conclusion that they grew at their final position in the trap, while smaller crystals might have been transported to the trap or the magnetic fieds of the pump or flow meter. The oxygen content of the eutectic in the magnetic trap was very high (c_o = 0.033 ±0.07 wt- %) indicating the formation of some oxides of steel constituents. After the repair of the cold leg components PICOLO was restarted in January 1988. The temperature was decreased to 500°C (773K) while the other parameters remained unchanged. The second test run is again dedicated to study the corrosion behaviour of the martensitic steel 1.4914. The first observations do not indicate a significant effect on the pump power due to lower corrosion rates at lower temperatures.

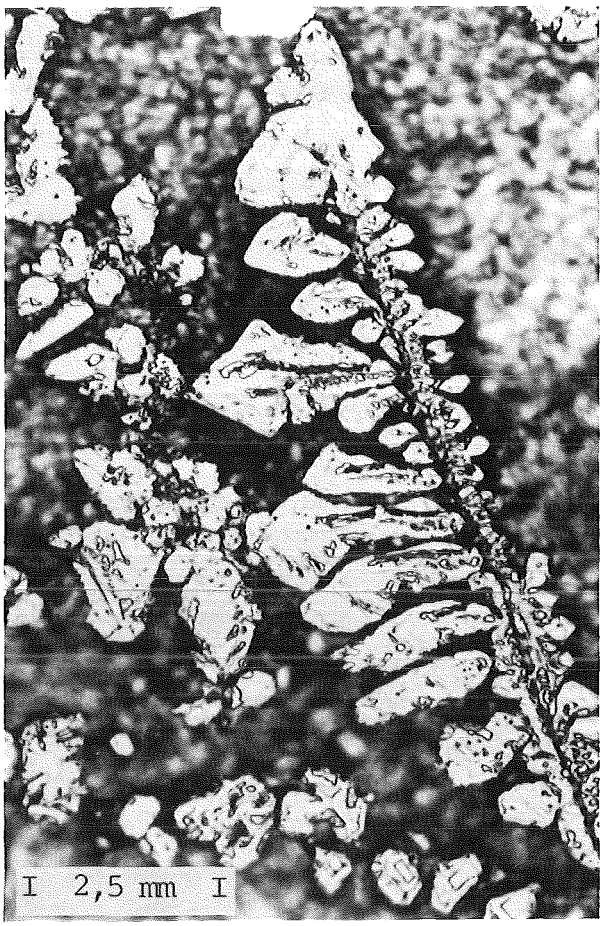

Fig. 9: Appearance of deposited crystals in the magnetic trap of PICOLO

Staff:
Ch. Adelhelm
H.U. Borgstedt
G. Drechsler
G. Frees
Z. Perić
G. Streib
S. Winkler

Publication:

H.U. Borgstedt, G. Drechsler, G. Frees, Z. Perić

Corrosion testing of steel X 18 Cr Mo V Nb 12 1 (1.4914) in a Pb-17Li pumped loop. 3rd. Internat. Conf. on Fusion Reactor Materials, Karlsruhe, Oct. 4-8, 1987, to be printed in J. Nucl. Materials

B 6.3 Fatigue of Structural Material in Pb-17Li

Low cycle fatigue tests in stagnant liquid Pb-17Li at 550°C (823K) were performed with specimens of the martensitic steel X18 Cr Mo V Nb 12 1 (1.4914). The NET batch of this steel was used to fabricate hour glass shaped specimens (gauge length 21 mm, minimal diameter 8.8 mm, radius 120 mm). These specimens were heat treated as recommended for this material:

2 h at 950°C - 980°C

0.5 h at 1975°C rapid cooling

and 2 h at 750°C

The number of cycles to failure (before rupture was completed at $\Delta\sigma \sim 0.5 \cdot \Delta\sigma_{max.}$), the variation of the stress amplitude with the number of cycles and the plastic strain were measured at total strain amplitudes in the range 0.010 to 0.0175. Some results are listed in Table 5

Fig. 10 shows the results gained so far in this test series.

Total strain amplitude	number of cycles to failure	average
0.010	13900; 18400	16150
0.0125	4900; 5950	5425
0.0150	3500; 3700	3600
0.0175	2150; 2600	2375

Table 5: Results of LCF-tests in Pb-17 Li at 550°C

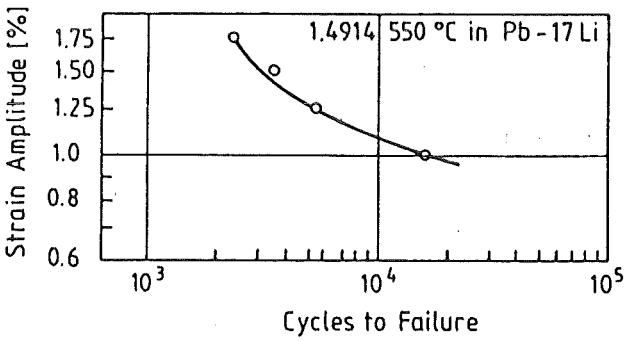

Fig. 10: Dependence of the number of cycles to failure on the total strain amplitude

Staff:
H.U. Borgstedt
M. Grundmann
Z. Peric
B. Seith

B9 Tritium Extraction from Liquid Pb-17Li by the Use of Solid Getters

Several methods were proposed to extract tritium from the liquid Pb-17Li blanket material. Task B9 is concerned with the use of solid getters.

The loop TRITEX is now in the start-up phase. About 100 kg of Pb-17Li were filled in the dump tank. Vacuum-degassing is underway. Static tests to study the compatibility of different metals with the eutectic are going on. First results were published [1]. For preliminary investigations of the hydrogen transport by liquid Pb-17Li, a small thermal convection loop, THERCOL-2, was constructed.

Figure 11 shows a photo of this loop. It was made of stainless steel 1.4571. The main piping inner diameter was 10 mm. The total inventory of Pb-17Li was 4.5 kg. THERCOL-2 was operated for 15 days at temperatures of 480/550°C. The flow of the liquid metal was counter-clockwise with a velocity of about 6 cm/s.

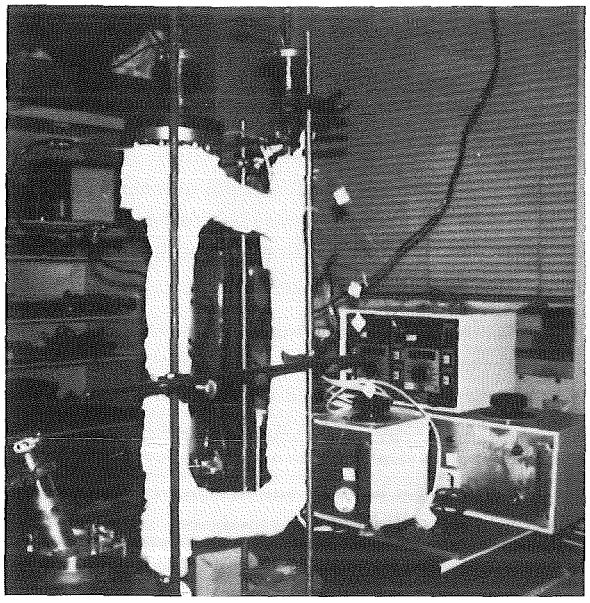

Fig. 11: Thermal Convection Loop THERCOL-2

In the main expansion tank of the loop 78 cm^2 of liquid eutectic surface were in contact with a slowly flowing gas phase. Two different gases were used: 0.97 and 9.81 vol% D_2 in argon. In order to determine the dissolution rate of deuterium in the liquid Pb-17Li, the gas was analyzed before and after the expansion tank with a HP5890 gas chromatograph. Furthermore degassing rates into argon were determined in a small second expansion tank with a liquid metal surface of only 0.8 cm^2.

Results

Using the gas with 0.97 vol% D_2, 0.034 cm^3 per hour deuterium were dissolved in the liquid metal. In case of the gas with 9.81vol% D_2, the respective value was 0.21 cm^3/h. In both cases the degassing rate was in the range of 0.005 cm^3/h.

Because of the large wetted surface of the loop, most of the dissolved deuterium was lost by permeation. Only a small fraction reached the second expansion tank. With the small liquid metal surface the degassing rate was very low.

For higher hydrogen pressures, Polcaro (J.Nucl.Mat.199 (1983), 291) measured the uptake of hydrogen by liquid Pb-17Li at 400°C. Extrapolating his initial values to the partial pressures of the used gases gives about 1000 times higher values for the dissolution rates. Besides some other effects, a thin oxide layer, floating on the surface of the eutectic in the expansion tank, is probably responsible for the low values found with THERCOL-2. After some other tests with this loop, the surface was covered with 120 mg/cm^2 oxide. No deuterium uptake could be detected any more.

Summarizing it can be concluded, that it is possible to dissolve sufficient hydrogen in the liquid Pb-17Li from a gas phase for experiments. Oxide-layers on the surface of the liquid metal however reduce the dissolution rate considerably. Furthermore, loss of D_2 from the liquid metal by permeation was high in the experiments. Nevertheless D_2-degassing could be measured. In the loop TRITEX an improved technique to dissolve more deuterium in the eutectic will be used.

References:

[1] H. Gräbner et.al, ICFRM-3, J. of Nucl. Mat. 135E (1988)

Staff:
H. Feuerstein
H. Gräbner
S. Horn

B11 - 16 Development of Ceramic Breeder Materials

The KfK contribution concentrates on the Li-Silicates and includes all the steps necessary to achieve a product to be used in the helium-cooled blanket design. The development starts with fabrication and characterization of pellets and pebbles. Physical, mechanical and chemical properties are measured before and after irradiation. The irradiation program makes use of several reactors within the European and the Beatrix Cooperation. Lithium-Orthosilicate has been proven to be the most promising candidate for the NET reference ceramic breeder material.

1. Fabrication and Characterization of Breeder Materials (B11, B12)

The preparation and characterization of lithium containing monosilicates, especially Li_2SiO_3 and Li_4SiO_4, are under development to be used as breeder materials for fusion reactors within the European Fusion Program (Task B11 and B12). Different samples of Li_4SiO_4 pellets and pebbles have been prepared for irradiation experiment ELIMA-3. Progress has been obtained in preparation of ceramic Li_4SiO_4 pebbles using an experimental fluidized-bed system for rounding and sintering of the prepared pebbles.

Preparation of Irradiation Samples for ELIMA-3

About 80 samples of Li_4SiO_4 pellets have been prepared for the irradiation experiment ELIMA-3 to examine thermal conductivity, Young's modulus, and thermal shock resistance after neutron irradiation and for material characterization. In addition about 100 cm^3 of ceramic pebbles have been prepared with 0.5 mm in diameter, densities of 85 to 90 % T.D., and a bulk density of 55 to 60 % to compare the pebble-bed behavior of ceramic and melted pebbles, the latter fabricated by SCHOTT company, under neutron irradiation. The pellets have to be assembled in form of test pins each containing 3x4 pellets for physical experiments and further four test pins for pebble-bed behavior (see table 6).

Number of Samples	Shape of Material	Density (% T.D.)	Remarks
16	pellets: 12.7 mm Ø 3 mm H	> 90	Thermal Conductivity
16	pellets: 10 mm Ø 5 mm H	> 90	Young's Modulus
16	pellets: 10 mm Ø 10 mm H	> 90	Thermal Shock Resistance
1 x 73 cm^3	ceramic pebbles	85-90 55-60 b.d.	Prepared by IMF III
31 x 73 cm^3	melted pebbles	95-98 63 b.d.	Prepared by SCHOTT Company

Table 6: Irradiation samples of Li_4SiO_4 for ELIMA-3

Characterization of Ceramic Breeder Materials

Besides some lithium metasilicate specimens mainly lithium orthosilicate specimens in the form of pellets and rounded granules had been fabricated for the irradiation experiments LISA-2 (Grenoble), TRIDEX (Jülich), ELIMA-1 (Karlsruhe), ELIMA-2 (Petten), and DELICE-03 (Saclay). The following procedures were used for the characterizing analysis of these specimens: ceramography, scanning electron microscopy, X-ray diffractometry, image analysis, measurement of sound velocity, mercury porosimetry, helium pycnometry, determination of gas permeability, and measurement of the specific surface area. The investigations of the open porosity of the various pellet specimens yielded the following results: The amount of open porosity found in the metasilicate samples by means of mercury porosimetry ranged between 90 and 100 % of the total porosity. One high-density sample resulted exceptionally in some 40 %. In the orthosilicate samples, however, a major dependence on the sample density of this percentage was observed. It ranged between some 10 % in a high-density sample and more than 90 % in a low-density sample.

The measurements performed by helium pycnometry indicated that, below the detection limit of measurement of the mercury porosimeter, there may be a rather high volume fraction of open porosity. This effect was particularly pronounced in the orthosilicate samples.

The results of the permeation property studies indicate that a cylindrical model represents a useful description of the network of open porosity based on the findings made by mercury porosimetry. However, the model seems to be inappropriate, if a relation is to be established between the measured specific surface area and structural parameters of open porosity determined by other methods.

In order to test industrial scale production a batch of 70 kg powder of lithium orthosilicate has been fabricated. This powder has a bulk density of 0.6 g/cm^3 (= 25 % T.D.). The specific surface area determined by applying the BET theory to volumetric nitrogen gas adsorption is 9.9 m^2/g. The rounded sinter granulates fabricated from this powder up to now (450 to 560 µm fraction) have a bulk density of 1.3 g/cm^3 (= 54 % T.D.). The specific surface area is 3.8 m^2/g. The granulates have a density of 2.06 g/cm^3 (= 86 % T.D.). The porosity of these granulates of 14 % is open porosity according to the helium pycnometry and mercury porosimeter measurements.

Preparation of Ceramic Pebbles

An experimental fluidized-bed system has been built up to optimize spherical shape, surface quality, and density of the ceramic pebbles prepared by powder metallurgical methods. The fluidized-bed, 5 cm in diameter and 120 cm in hight, can be heated-up to about 1200 °C. Batches of about 1 kg monosilicate pebbles can be sintered and rounded within this arrangement under fluidized conditions.

Staff:
B. Dörzapf
H. Elbel
E. Günther
R. Hanselmann
J. Heger
W. Laub
H. Nagel
R. Scherwinsky
Dr. D. Vollath
Dr. H. Wedemeyer
M. Wittmann

Publications:

D. Vollath, H. Wedemeyer: Advances in Ceramics (1988) in print, "Preparation of Aluminates and Silicates of Lithium in Aqueous and Alcoholic Media"

H. Elbel: J. Nucl. Mat. 154-156 (1988) in print, "Open Pore Structure Analysis of Lithium Bearing Ceramics"

W. Breitung, H. Elbel, J. Lebkücher, G. Schumacher, H. Werle: J. Nucl. Mat. 154-156 (1988) in print, "Out-of-pile Tritium Extraction from Lithium Silicate"

H. Werle, M. Briec, R.G. Clemmer, H. Elbel, H.E. Häfner, J. Masson, G. Schumacher, H. Wedemeyer: J. Nucl. Mat. 154-156 (1988) in print, "The LISA Experiment: In Situ - Tritium Release from Lithium Silicate"

G.W. Hollenberg, S. Casadio, B. Rasneur, H. Elbel, H. Wedemeyer, D. Walker, T. Takahashi, K. Noda, H. Akiyama: J. Nucl. Mat. 154-156 (1988) in print, "The Irradiation of Solid Breeder Pellets, Spheres and Single Crystals to Moderate High Burnup Levels in a Fast Neutron Flux, FUBR-18 in BEATRIX-1"

2. Measurement of Physical, Mechanical and Chemical Properties (B13)

Physical and Mechanical Properties

The measurements of thermophysical properties on γ-$LiAlO_2$ and Li_2SiO_3 are complete. On Li_4SiO_4 the thermal expansion has been measured:

$$\Delta l/l_0 = -0.00131 + 4.38 \cdot 10^{-6}\, T;\ [T] = K;\ R.T. < T < 850\ K$$

First results of the thermal diffusivity a of Li_4SiO_4 show lower values than those published in the literature.

An important result of the property measurements on ceramic breeder materials was the conclusion, that the resistance to thermal crack formation will be lowest for Li_4SiO_4. Therefore its change under irradiation is of major concern. The thermal shock resistance of irradiated Li_4SiO_4 pellets (8mm diam.) of the LISA 1 experiment (Siloë Grenoble, 7×10^{19} n/cm^2 at 600 °C) was measured by dipping the pellets into liquid tin. The results were compared with those of unirradiated pellets. Under the same test conditions the lowest temperature difference at which cracking occurred was 375 K for the irradiated pellets and 490 K for the unirradiated pellets. The thermal shock resistance of Li_2SiO_3 is higher. Irradiated Li_2SiO_3 pellets (8 mm diam.) of the same experiment (but at 700 °C) did not crack at temperature differences up to 800 K. However, a comparison with the unirradiated state was not possible because no unirradiated pellets were available.

Staff:
M. Blumhofer
G. Haase
B. Schulz
H. Zimmermann

Constitution, Interaction with Water Vapour

Besides Li_2O, $LiAlO_2$, Li_4SiO_4 and Li_2SiO_3 also the lithium zirconates Li_2ZrO_3 and Li_8ZrO_6 are under discussion as ceramic breeder candidates. Since the phase relations in the Li_2O-ZrO_2 system are unknown up to now, experimental work has been started to establish the Li_2O-ZrO_2 phase diagram. In the first step the efforts were concentrated on the Li_2ZrO_3 region. The polymorphism of Li_2ZrO_3 reported in the literature could not be confirmed; only the monoclinic "high temperature modification" was obtained in the temperature range between 900 °C and 1100 °C starting from ZrO_2 and LiOH as well as Li_2CO_3. Thermal analyses revealed the stability of this modification up to the congruent melting temperature at 1690 °C. By varying the Li_2O concentration towards higher Li:Zr ratios a eutectic temperature at 1290 °C was found.

A high temperature heat flux calorimeter was installed and is now being tested and calibrated for the measurement of thermodynamic data of ceramic breeder candidate compounds.

The investigations concerning the interaction with water vapour were continued with Li_4SiO_4 pellets fabricated from a granulated material (0,3 - 0,5 mm diameter, 92 % of theoretical density). Enhanced H_2O adsorption was observed at 400 °C by isothermal "effluent analyses" (time-dependent variation of the H_2O concentration in the flowing gas outlet after changing the inlet p_{H_2O}). Desorption occurs in a slow single step. Appreciable losses of weight (2 - 3 %) by vaporization were observed in isothermal tests at 1050 °C/1000 ppm H_2O after 30 hours. According to REM examinations of fracture surfaces, a second phase (Li_2SiO_3) had been formed.

The test for the simulation of the storing and handling conditions were continued with $LiAlO_2$ pellets. After 3 months at ambient temperature in air, a weight increase of 7.5 % was measured. X-ray diffraction examinations showed that LiOH, $LiOH \cdot H_2O$ and $LiAlO_2 \cdot H_2O$ were formed only temporarily, whereas the finally formed phases could not be identified.

Staff:
H. Kleykamp
V. Schauer
G. Schlickeiser
A. Skokan

The Solubility of Hydrogen in Lithium Metasilicate

For the evaluation of lithium as candidate ceramic breeder material the tritium inventory appears to be an important criterion. Under neutron irradiation the tritium steady state inventory is determined by the amounts trapped, dissolved and absorbed; tritium beyond that required for the potential driven diffusion will remain in the solid.

The solubility of hydrogen in lithium metasilicate pellets was measured by a gas volumetric technique in an apparatus already described in earlier reports. The results are summarized in Table 7

Tempe-rature [°C]	Hydrogen pressure [hPa]	Solubility S [mol H/ mol Li2SiO3]
450	499	2.3·10-5
450	468	2.2·10-5
450	548	2.6·10-5
500	547	3.6·10-5
550	541	4.3·10-5

Table 7: Hydrogen solubilities in lithium metasilicate at various temperatures

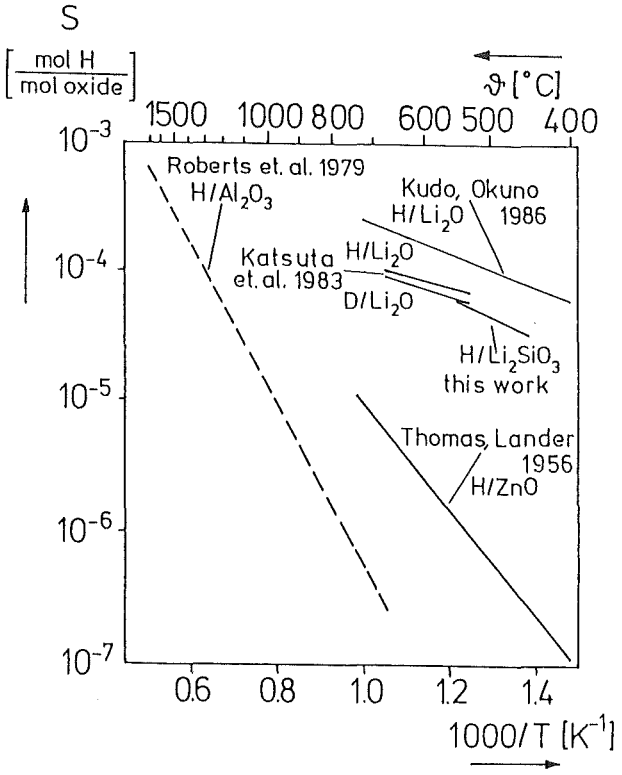

Fig. 12 : Solubility of hydrogen in different ceramics

For comparison purposes the measured solubilities were normalized by 1/p and plotted together with literature data on hydrogen solubilities in lithium oxide, aluminium oxide and zinc oxide (see Fig.12). Within the operational temperature window of a fusion reactor blanket the data for lithium oxide and lithium metasilicate appear to be comparable. From the slope of the Arrhenius plot a heat of solution of 29 kJ/mol for hydrogen in lithium metasilicate is estimated.

In addition, the equilibrium amount of hydrogen incorporation into lithium metasilicate pellets at a given temperature and pressure was determined directly using hydrogen containing trace amounts of tritium ($x_T = 4 \cdot 10^{-4}$): Carefully dried pellets were loaded with the hydrogen/tritium mixture at temperatures between 450°C and 600°C at pressures from 30 to 2800 h Pa. To analyse the pellets for incorporated tracer they were quenched to room temperature, the supernatant tritiated hydrogen pumped off down to about 10^{-5} hPa, the pellets dissolved in aqueous hydrofluoric acid and the tritium content measured by liquid scintillation counting with standard procedures.

A comparison of the hydrogen inventories obtained with the tracer technique and the volumetric technique at a hydrogen pressure of about 500 h Pa is shown in Figure 13. The higher inventories measured by the tracer technique at low temperatures, i.e. <500°C, appear to arise by tritium/hydrogen exchange with residual water present at ppm levels in the crystallattice and/or the surface of the lithium ceramic. As the loading temperature is raised enhanced release of trapped water causes the inventory to decrease and to become determined by physical solubility.

Staff:
M. Glugla
R. D. Penzhorn
K. H. Simon

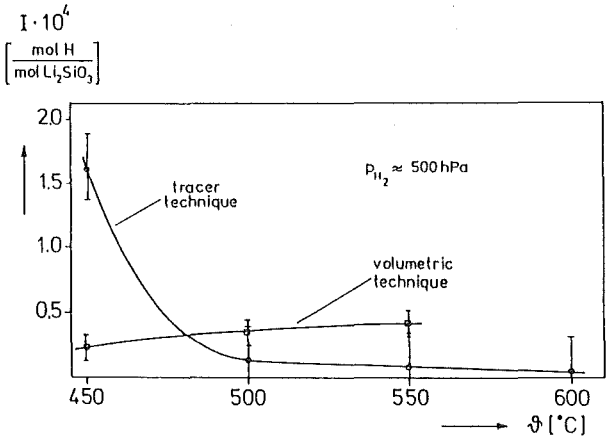

Fig. 13: Comparison of the amount of incorporated hydrogen as obtained by the tracer technique and the volumetric technique at constant hydrogen pressure of about 500 h Pa

3. Compatibility with Metallic Materials (B 14)

The capsule annealing tests made to investigate the chemical compatibility of Li_2O, Li_4SiO_4, and Li_2SiO_3 with potential cladding materials have been finished. Four different cladding materials were used for the last test series in the high temperature range of 800 to 1000 °C: the martensitic-ferritic Cr-steel 1.4914, the austenitic Cr-Ni-steel 316, and

the nickel alloys Hastelloy X and Inconel 625. Fig. 14 shows a survey of the results obtained after 100 h annealing. Li_2O caused by far the most violent attack on the cladding, even more pronounced at these very high temperatures, while the attack by Li_4SiO_4 was found to be unexpectedly moderate. The compatibility behavior of 316 is not considerably poorer than that of the nickel alloys. 1.4914 becomes problematic at temperatures ≥ 800 °C which, however, is not shown in Fig. 14.

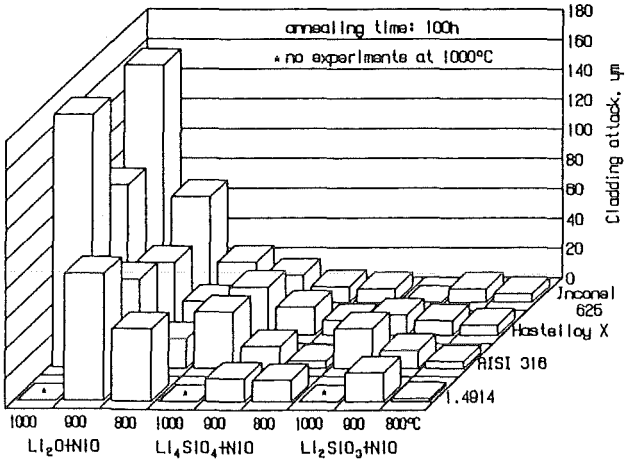

Fig. 14: Penetration depth of the chemical attack on four capsule materials with different ceramic breeder compounds (+ NiO to simulate the oxygen surplus under operation).

A preliminary evaluation of recent compatibility tests with metallic beryllium, which is of interest as a neutron multiplier, and Li_4SiO_4 resulted in smaller reaction rates than observed with Li_2SiO_3 at 700 and 750 °C. This may be due to the higher thermodynamic stability of Li_4SiO_4. At 650 °C the reaction rate seemed to be technically admissible, with a maximum penetration depth < 20 µm in 1000 h. But the reaction rate of beryllium with the stainless steel capsule (AISI 316) was considerably higher at 650 °C. Therefore the cladding temperature should be kept ≤ 600 °C.

Staff:
P. Hofmann
K.-H. Kurz
H. Metzger

4. Irradiation Testing of Ceramic Breeder Materials (B15 und B15.3)

In assessing the potential performance of solid breeders, tritium release rate and retention are important aspects. KfK concentrates on lithium silicates. In addition to the in-pile tests (B16), tritium release is studied in out-of-pile annealing experiments.

A series of annealing studies with different types of meta- and orthosilicate irradiated in the DIDO reactor at KFA Jülich and from the first in-pile test LISA-1 in the SILOE reactor have been performed. The time-dependence of the release rate was generally not consistent with diffusion, indicating that other processes, probably surface effects, are important. Therefore surface effects were studied in detail by varying the flow rate, pressure and chemistry (additions of H_2 and moisture) of the Ar purge gas. These tests confirmed that for our meta- and orthosilicate samples the release is strongly determined by surface effects. Various models have been developed to describe possible release-controlling processes. The good agreement between measured release and prediction by the "recombination" model indicates that recombination of chemisorbed tritium, according to $(OT^- + OH^-)_{surface} \rightarrow (O^{2-})_{surface} + HTO_{gas}$, is an important release process (Fig. 15).

One type of metasilicate pellets (density 1.63 g/cm³, TD 65 %, sample no. 41, stack no. F*6, stack height 40 mm, 7 pellets) of the first irradiation, DELICE 01, in the OSIRIS reactor have been annealed. These pellets were irradiated without cladding at a temperature of 700-720 °C. The thermal neutron fluence was $6.6 \cdot 10^{19}$ 1/cm², the total tritium production and the tritium production rate p per pellet was 0.7 C and 1.1 mC/h, respectively. Three pellets were annealed at increasing temperatures up to 730 °C. The total release, which can be assumed to be equal to the tritium inventory I, was 1.8 ± 0.1 mC. The fractional tritium retention therefore is 1.8 mC/0.7 C = 0.26 % and the residence time $\tau = I/p = 1.6$ h. The residence time is consistent with the in-pile and out-of-flux results for the metasilicate pellets of LISA-1 and about a factor hundred higher than those for the orthosilicate samples of LISA-2.

A remarkable weight loss was observed: before irradiation the pellet weight was ≥ 0.178 g, afterwards it was only 0.172 g. This is due to a loss of small particles from the surface during transportation and handling. Ceramographic studies are under way with the annealed pellets.

An advanced stage has been attained of preparatory work for the planned international comparative irradiation B15.3 of 36 cladded sample stacks each in the thermal neutron flux of the OSIRIS reactor and in a fast flux under cadmium in HFR/Petten, respectively. The ceramic breeding rods have already been assembled into the irradiation rigs ELIMA 2 in Petten and DELICE 03 in Saclay. Both irradiations will probably be completed in the course of 1988.

Staff:
W. Breitung
T. Eberle
H. Elbel
H.E. Häfner
K. Heckert
J. Lebkücher
K. Philipp
H.-J. Ritzhaupt-Kleissl
G. Schumacher
H. Werle

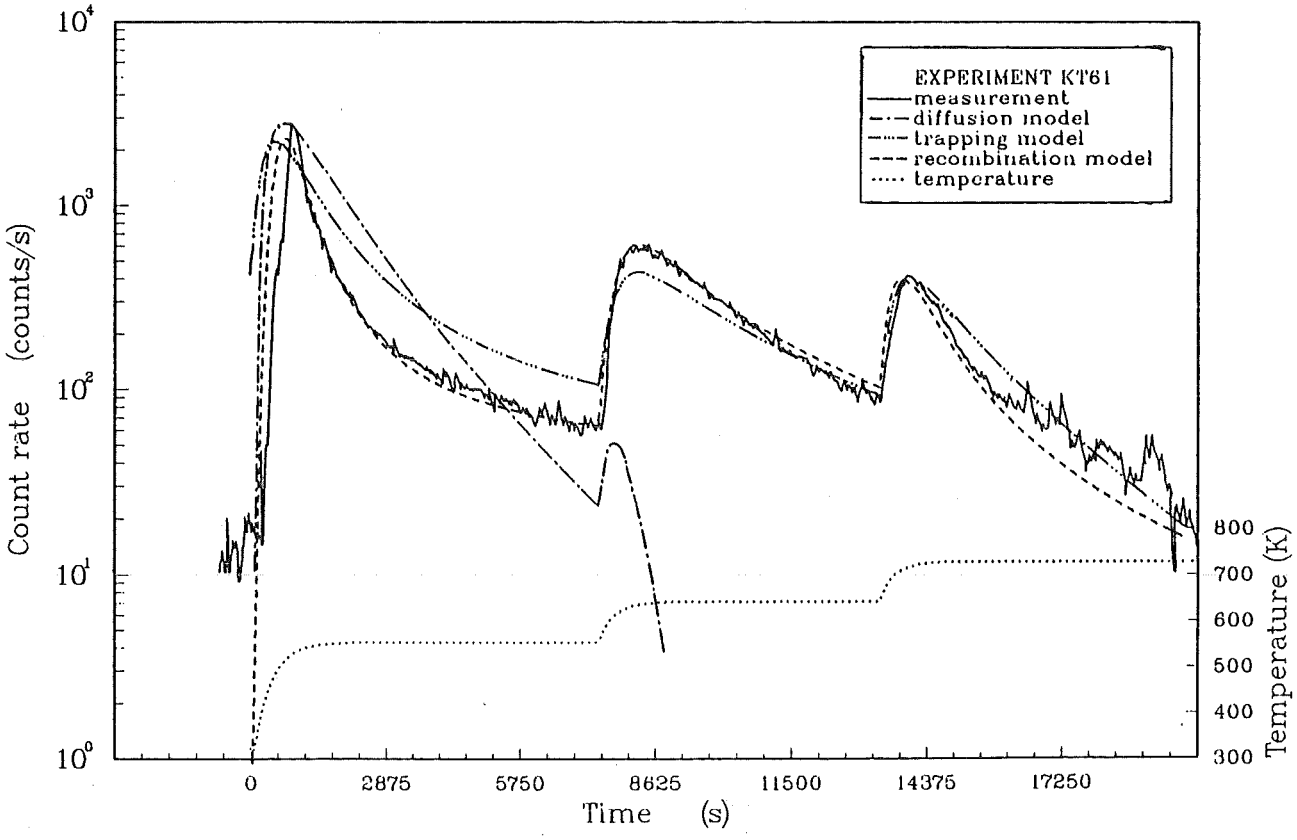

Fig. 15: Comparison of calculations and measurements for 0.3mm orthosilicate spheres (TD 95%)

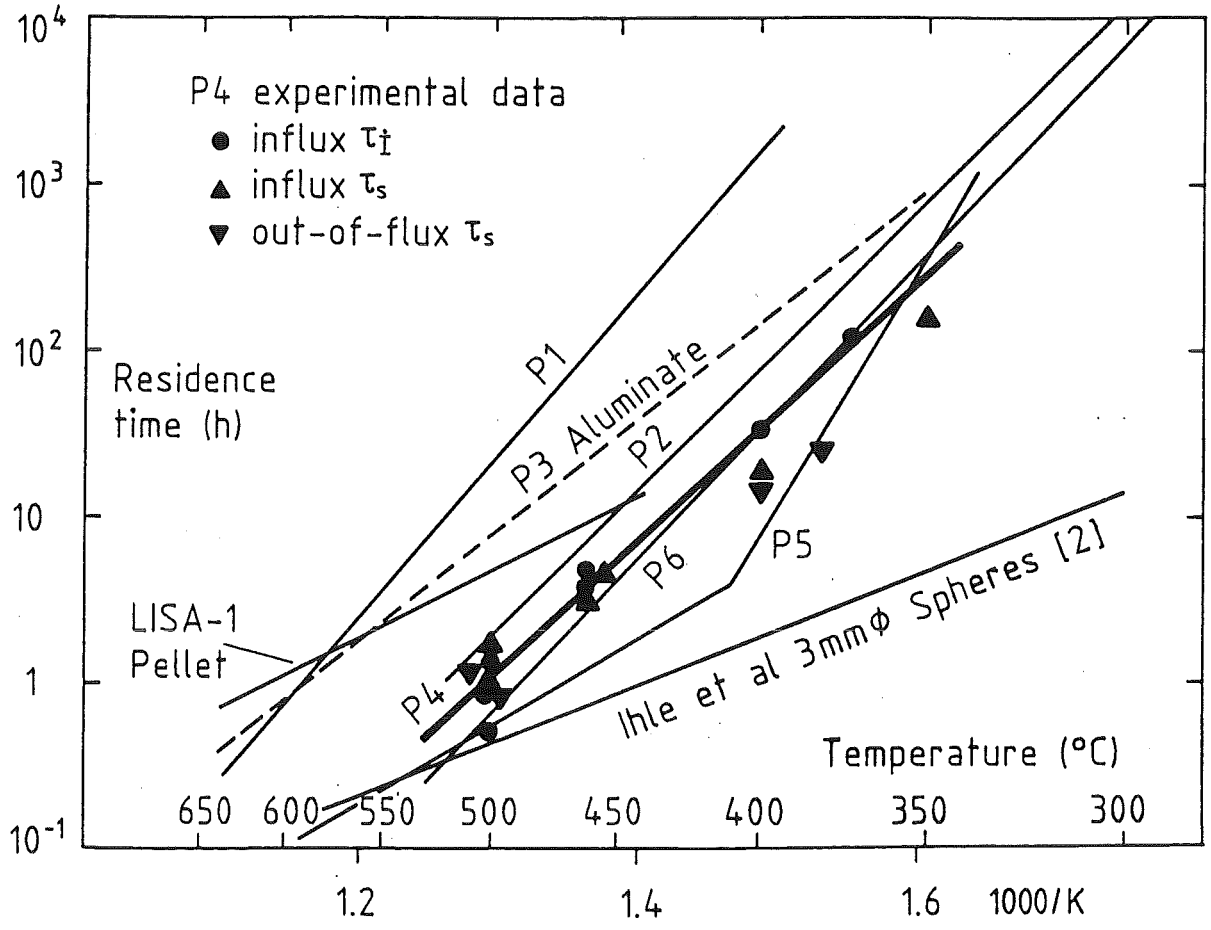

Fig. 16: Residence times for orthosilicate samples of LISA-2
(P1 0.5 mm granules, P3 aluminate pellet, P5 pellet, P2 0.5 mm spheres, P4 1.25 mm tempered spheres, P6 0.5 mm tempered spheres)

5. Tritium Recovery from Ceramic Breeder Material (B16)

Tritium recovery from ceramic breeder material is important in assessing the potential performance of breeder blankets. The behavior of lithium silicates is studied by KfK in the LISA-series of in-pile tests performed in the SILOE reactor at CEN/ Grenoble.

Because of the fast tritium release of orthosilicate observed in the first test LISA-1, the second test LISA-2 concentrated on this material and, to meet the requirements of the KfK pebble bed design for a NET blanket, especially on high-density (97 % TD) spheres and low temperatures. Irradiation started November 24 and was stopped December 2, 1986 because of a leak in the tank of SILOE. Therefore cycle 2 and 3 of LISA-2 were performed in the neighbouring MELUSINE reactor from October 19 to 30 and from December 10 to 23, 1987, respectively. Residence times have been evaluated by $\tau_I = I/p$ (I inventory, p production rate) and from the slopes to the time-dependent release (τ_s). They are shown in Fig. 16 for sample P1 together with the fits to the τ_I values of the other samples and with out-of-pile annealing data for 3 mm orthosilicate spheres (97 % TD) of Ihle et al. The residence times for our orthosilicate samples differ by up to a factor hundred (P1, P5). Above about 500 °C the residence times for our samples (except P1) are comparable with, but at 300 °C they are about three orders of magnitude larger than the annealing data for the 3 mm diameter spheres. This large discrepancy and the sensivity of tritium release on purge gas chemistry (additions of H_2, O_2, moisture), observed in the in-pile as well as in annealing experiments, strongly indicate that for our samples surface effects are dominant. Attempts are underway to model release-controlling surface processes and to prepare samples with smaller specific surface area.

Staff:
H. Elbel
H.E. Häfner
H. Werle

M 1 The Large Coil Task

The Large Coil Task is an experiment of the International Energy Agency with contributions of four nations. The goal of the experiment is to make the superconducting magnet technology available for Tokamaks. The European Community contributes to this experiment with one superconducting coil. The coil was designed, developed and constructed on behalf of Euratom by KfK-Karlsruhe together with two German companies: Vacuumschmelze, Hanau (conductor) and Siemens AG, Erlangen (coil). The test program ran since January 1986 at Oak Ridge Nat. Lab., USA. The Euratom coil passed successfully all"Standard Tests" and entered in April 86 the series of the "Extended Tests". The whole test program was successfully completed in September with outstanding results for the Euratom LCT coil.

After warming up of the facility and the coils through September and October 87 the lid of the vacuum vessel was removed on October 9, 87. The inspection of the torus showed, except for the driving mechanism of the pulse coil system which was inoperable, no larger damage.

Several screws were found loose. At some coils larger gaps (1-2 mm) were found between bucking post respectively torque rings and coils at the supporting areas. As already found by finite element calculations the force transmission in such a sophisticated mechanical structure was the most critical item especially in case of high out-of-plane forces.

In December 87 the preparation of the removal of the Euratom LCT coil from the vacuum vessel was started. In December 17, 87 the coil was lifted out of the vacuum vessel. The coil was packed with its special equipment and shipped in January 21, 88 from Oak Ridge to KfK - Karlsruhe, where the coil arrived in March 1, 88. The evaluation of the test results is running as a contribution to the joint summary report prepared together with the other participants.

The results of the loss of coolant measurements were evaluated and summarized in Fig. 17. This figure shows the temperature profiles at different critical locations of the hydraulic system of the winding. With exception of the temperature sensors mounted directly on the copper bar of the current feedthrough all other temperature sensors needed a helium flow for a correct indication. Therefore their indication was too high without flow and came down immediately after the installation of the flow. The temperature of the injected helium after a flow stoppage was drawn as a function of the stoppage time (Fig. 18). Combined with known current sharing temperatures of the coil conductor the critical time of flow stoppage was determined by that time, after which no reinstallation of the flow was possible without quenching the coil. This temperature was not reached at 8 kA current but for 11.4 kA only about 7 minutes were needed to exceed the current sharing temperature. It can be derived from these results that the coil should be capable of exceeding this time without quenching if the flow was not reinstalled. Therefore in the final experiment the flow was first stopped for 10 minutes and then the coil was ramped down without flow. The coil

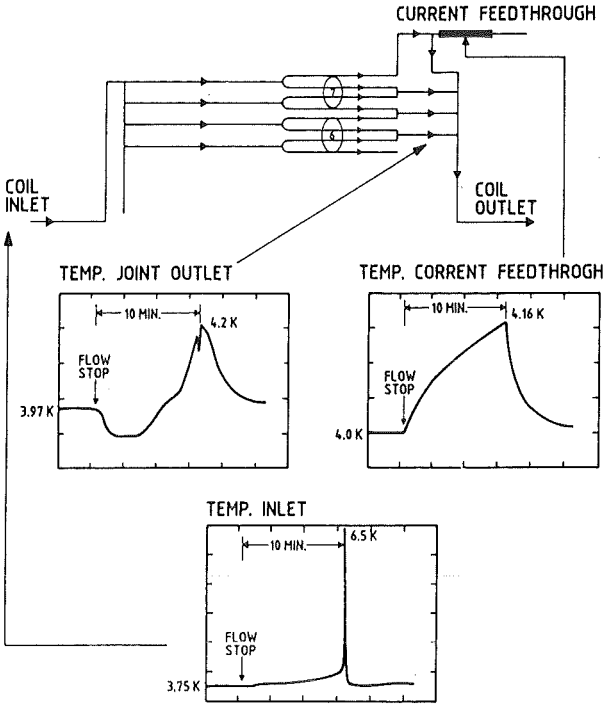

Fig. 17: Temperature profiles at different critical locations of the hydraulic paths of the winding.

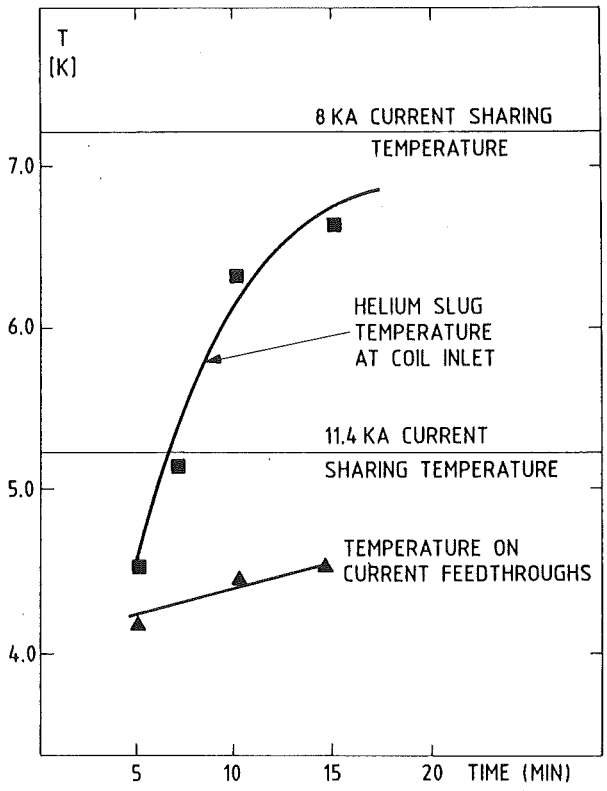

Fig. 18: The temperature of the helium slug which was injected in the coil after a flow stoppage as a function of duration of the flow interruption.

reached zero current without quenching and demonstrated impressively its thermal inertia and the safe operation without flow.

The evaluation of the out-of-plane load cases (one coil without current in the torus) brought some interesting results. The coil was exposed to a negative and positive out-of-plane load. The analysis of this load cases looked completely different. While in the first test the equivalent stresses were linear in current square (Fig. 19) for the second

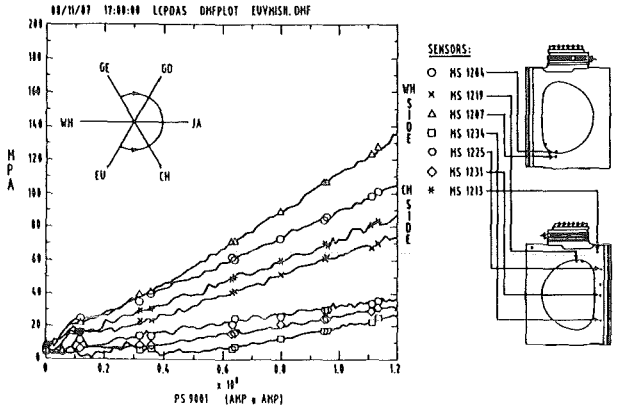

Fig. 19: Equivalent stresses as a function of current square for the EU-GE test (WH coil without current).

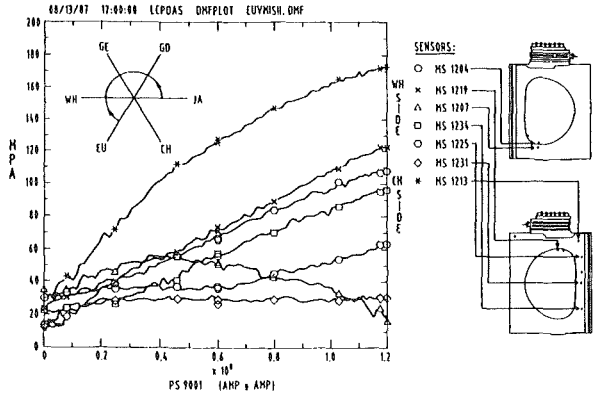

Fig. 20: Equivalent stresses as a function of current square for the EU-JA test (CH coil without current).

test some strong deviations from the linearity were observed (Fig. 20). Sensors were analyzed at the periphery of the upper and lower collar as well as sensors at the beams of the torque rings . Both load cases looked a little bit different but the spring constant of the facility structure was nearly the same (Fig. 21). A higher scan rate of one of the sensors presented idling at the beginning of the loading (Fig. 22). A big hysteresis effect was observed when the force was released after reaching its maximum. This effect demonstrated some problems of force transmission in the toroidal structure. The boundary conditions at the supporting points of the coil were not those which were assumed for the finite element calculations. This could be concluded from the observed non-linearities of the equivalent stresses in the second out-of-plane load case. These results of the tests and the findings of the inspection

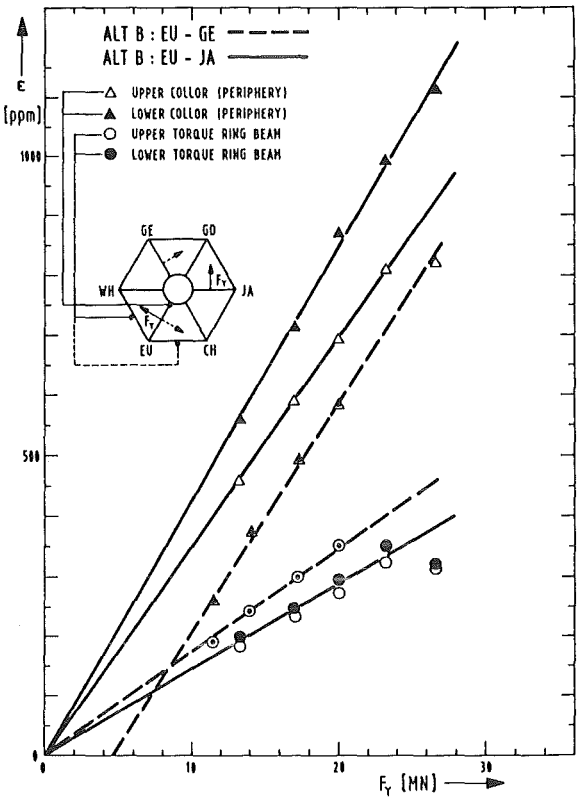

Fig. 21: Strain gauges at the periphery of the upper and lower collar as well as at the beams of the upper and lower torque ring. The strain was plotted against the out-of-plane force for both tests EU-Ge and EU-JA.

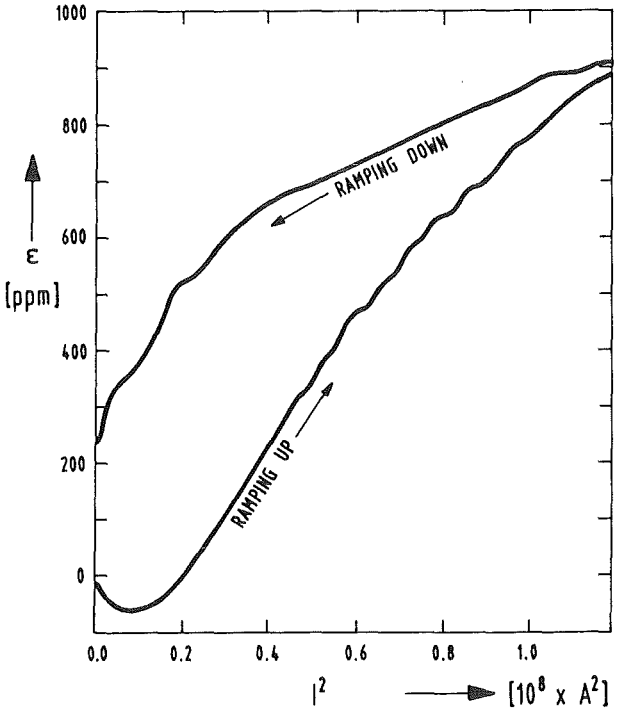

Fig. 22: The strain of the upper collar measured with a higher scan rate demonstrating back lashing and hysteresis.

demonstrate that some development is needed to have suitable elements available for a backlash-free structure for this dimension and these forces.

Staff:
H. Bayer
G. Friesinger
S. Gauss (till Jan. 31, 1988)
W. Herz
W. Maurer
A. Ulbricht
F. Wüchner
G. Zahn

M 3 Development of High Field Composite Conductors

Effect of Transverse Compressive Stresses on I_c of Ta alloyed Nb_3Sn Wires

The compressive stress rig described in the last semi-annual report was designed for our Karlsruhe facility with a 13.5 T split coil magnet. Due to the importance of the results for the NET conductor design, the investigation was extended from binary Nb_3Sn to Ta alloyed Nb_3Sn commercial wires. In addition, a new rig with smaller compression area was constructed in order to determine a possible influence of the edges on I_c. In order to understand better the field dependence of the effect, the new rig (see Fig. 1) was designed to fit into a polyhelix hybrid magnet of the High Field Laboratory in Grenoble, France.

The direction of the magnetic field, B, is perpendicular to the axis of the sample and parallel to the applied force, F. The mechanical load is generated outside of the cyrostat by a screw system and transferred to the sample through a force gauge and a compression bar. In the lower cold part of the test rig (Fig. 23) the transverse stress on the sample is produced by slowly pushing the movable pressure block against the (fixed) lower pressure block by means of the compression bar. These blocks consist of fibre glass reinforced plastic with a high compressive strength (660 N/mm², Stesalit 4411 W). The total compressed length of the conductor amounts to 4 mm, the compressed cross section thus being 4 x 0,85 mm². The sample is soldered into the current terminals, the free length between these terminals being 15 mm. The voltage taps, V, are soldered to the sample immediately besides the compressed zone. The upper limits for electrical current, I, and transverse stress, σ_t, for this test rig are about 200 A and 200 MPa, respectively.

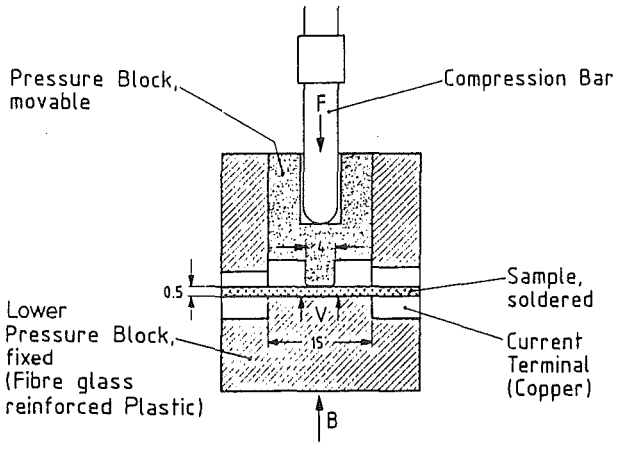

Fig. 23: Lower part of test rig G used in this investi-gation for applying transverse compressive stress to the wire in a solenoid magnet

The characteristics of I_c/I_{cm} vs. B at constant compressive stresses for the Ta alloyed wire is illustrated in Fig. 24, showing a slightly smaller decrease of the critical current with magnetic field than for the binary wire. Comparing again at σ_t = 100 MPa, it seems that I_c/I_{cm} falls from 0.85 at 10 T to 0.30 at 20 T.

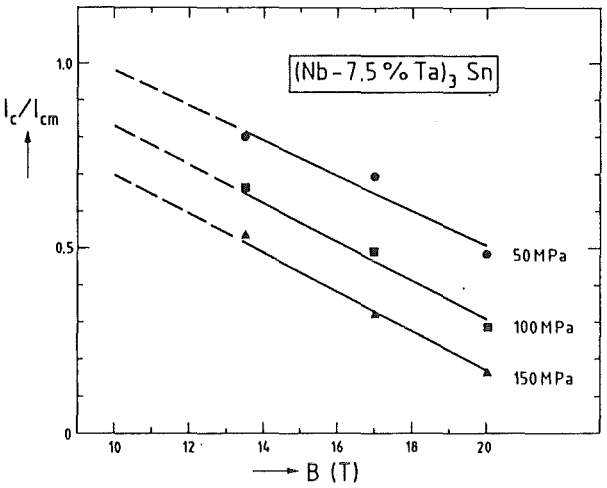

Fig. 24: Normalized critical currents, I_c/I_{cm}, versus magnetic field, B, for constant transverse compressive stresses of 50, 100 and 150 MPa for (Nb-7.5 Ta)$_3$Sn wires.

The effect of transverse compressive stress on critical current and upper critical field of both binary and Ta alloyed Nb_3Sn multifilamentary wires in the high field region has been investigated. These materials show a degradation of both I_c and B_{c2} vs. σ_t, which is more pronounced for the binary wire. This effect is much stronger than that of axial tensile stress and is enhanced with increasing magnetic field.

The question arises whether the transverse stress may affect e.g. the performance of the conductor for the NET-TF coils, where calculations predict local transverse stresses up to 149 MPa/5/, occuring in the low field region, while in the high field region (11T) the stresses still reach 140 MPa. In the NET conductor design /8/ the Nb_3Sn strands are surrounded by a steel conduit (40% of the total cross section) which strongly reduces the stress acting directly on the strands. It is very hard to predict the effective stress fraction reaching the Nb_3Sn strands, but assuming the latter would be submitted to 50% of the peak stress (σ_t = 70 MPa) a I_c degradation of the order of 30% for binary Nb_3Sn and above 15% for (Nb-7.5 Ta)$_3$Sn wire would be expected at 11 T. It follows that this effect must be taken into account for the design of the NET-TF conductor.

Staff:

W. Barth
M. Beckenbach
M. Brünner
P. Duelli
U. Fath
R. Flükiger
S. Förster
F. Gauland
W. Goldacker
A. Kling
B. Lott
G. Nöther
A. Nyilas
H. Olschulko
H. Raber
T. Schneide
W. Specking
S. Stumpf
P. Turowski

M 4 Superconducting Poloidal Field Coil Development

The aim of task M4 is to develop and test a superconducting poloidal model coil relevant for Tore Supra and NET and to simulate in the test similar load conditions. The model coil of 3 m ø is under design to be operated in the KfK-TOSKA test facility in 1989. Both tasks M 4 and M 8 are joint efforts of KfK and CEA.

Conductor fabrication

For the final fabrication stage of the conductor the required drawing maschine was now made available. Pieces up to 700 m length of the quarter section profiles were produced within the specified tolerances suitable for laser beam welding. Two quarter profiles were successfully laser beam welded to an U-profile of 120 m for the first lengths of prototype conductor production. 75 m length of the central cable were manufactured and the protection tube was drawn on the cable within the required tolerances. After production of components of the Polo cable the welding production line with a 6 kW laser operating at 2 kW was taken into operation. The laser is equipped with a beam splitting device generating two beams which can weld simultaneously the two U-profiles to a vacuum tight conduit. In a first attempt 50 m conduit including 25 m dummy cable have been welded in the production line. Difficulties in the availability of the laser itself and the stability of the beam splitting device are presently investigated and the system is being improved.

Basic electrical investigation for the conductor concept.

The transverse resistivity was measured in a series of laboratory made cable samples. The degree of compaction of the cable was varied by the tight drawing procedure of the outer tube. The transverse resistivity measured at helium temperature for the different samples is presented in Fig.25. The results showed clearly that as well the Kapton insulation between inner tube-cable and between outer tube-cable as the CuNi tape wrapped around the subcables contributed to the increasing transverse resistance. Some samples were investigated by measurements of time constants and AC loss measurements, too. While the time constant measurements result in too high values compared with simple calculations the AC loss measurements gave a fairly good agreement with losses calculated from the resistance measurements (Fig. 26).

The hysteresis losses extrapolated from these measurements agreed well with the expectations. From calculations it can be derived that the CuNi wrapped subcables with a transverse resistance of R_0L = 5 μΩm can withstand the specified plasma disruption without exceeding the transient removable heat load. The transient removable heat load (1.2 mJ/cm²) is smaller than the maximum removable heat load (2 mJ/cm²).

For the investigation of the conductor stability an experiment with a loop made from the Polo cable without the rectangular conduit is running. First measurements of the

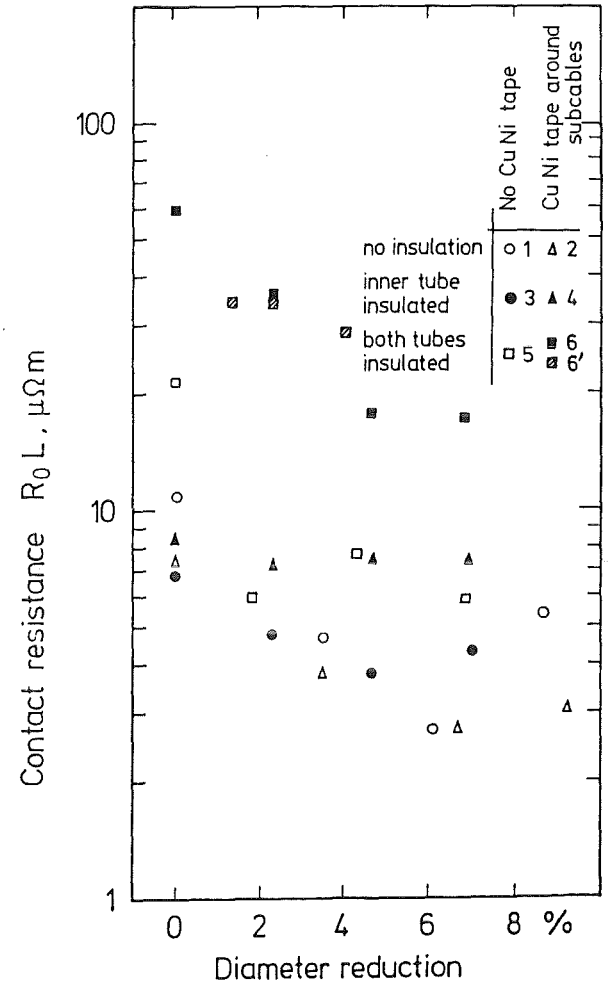

Fig. 25: The transverse resistance as a function of the degree of compaction of the cable by diameter reduction of the outer tube. Subcables are wrapped by a CuNi tape.

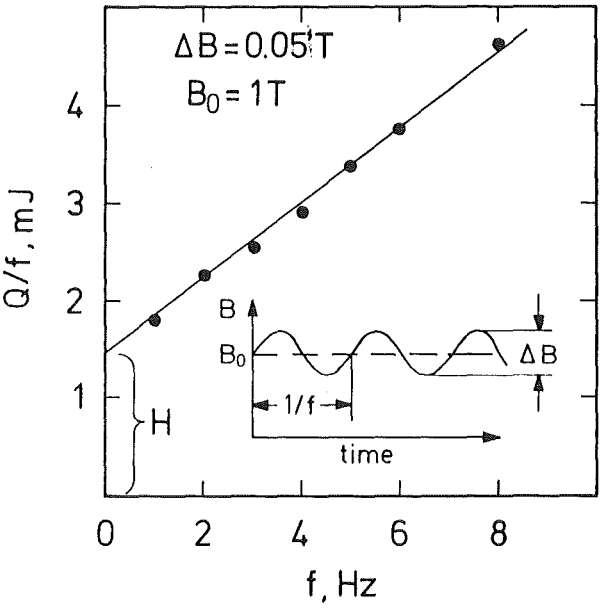

Fig. 26: Measured AC losses for 1 cycle for sample No. 3 with 7% diameter reduction

critical current were performed. The measured critical current was lower than expected. Possible reasons are being investigated and are supposed to come from the cable connection.

Basic thermo-hydraulic investigation for the conductor concept

The measurements of the 2-phase flow experiment were evaluated. The measured pressure drop of the two-phase flow is in good agreement with the theoretically expected values (Fig. 27). The experiment confirmed that a cooling system

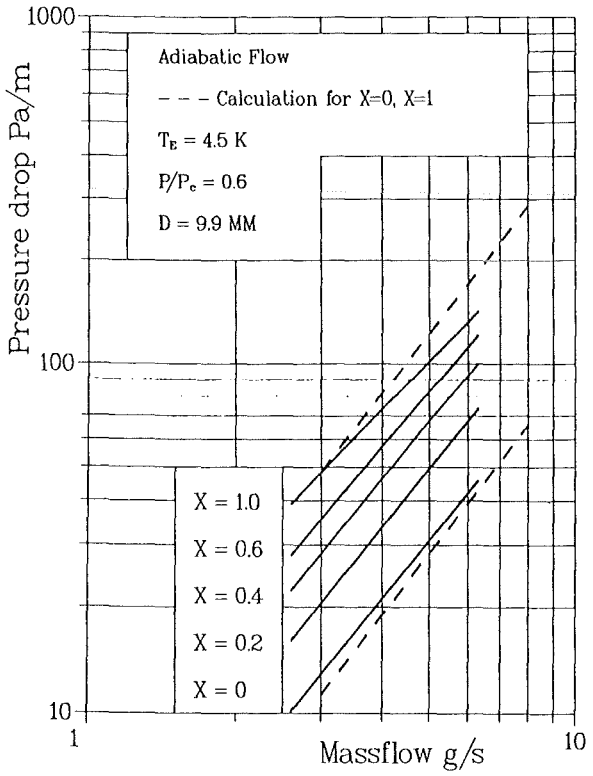

Fig. 27: Comparison of measured and calculated pressure drop for a two-phase Helium flow as a function of the mass flow rate with void fraction a parameter

with two-phase Helium can be operated stably under the specified heat loads.

Construction of the model coil

The model coil is in the design phase by the manufacturing company (Alsthom, France). Accompanying material investigations and investigations to assure manufacturing concepts were performed at KfK.

In a joint effort of KfK and Alsthom investigations on the shear stresses of the different insulation systems canditates of the model coil were performed. Two kinds of samples, double lap shear samples and short beam samples were used. At three temperatures the shear stress was determined. The results are presented in Fig. 28. A finite element calculation of the lap-shear sample elucidated the discrepancies between the two methods and contributed considerably to the understanding of the two test methods. It was assured that the short-beam test gave the correct values. Therefore there existed sufficient margin for the expected shear stresses of about 11 MPa for the load cases of the model coil. In the high-voltage laboratory an evaporating cryostat was taken into operation for investigations of the breakthrough voltage of materials. Times for cooldown (warmup) from room temperature to 10 K of less than 15 minutes were obtained without test samples. About one hour was needed within the test sample which has to be improved. Samples (analog to short-beam tests) of insulation system candidates were investigated up to 10^7 voltage pulses. A degradation of the starting of the partial discharge activity was clearly observed for GFK/Kapton insulation. This was much less the case for the GFK insulation. The breakthrough voltage of the samples was 13-16 kV and therefore about 3 times higher than the rated voltage. The ground insulation consisting of 7 layers Kapton/glass fabric showed a starting of the partial discharge activity far below 23 kV. This fact is not understood up to now and has to be investigated. In collaboration with the High-Voltage Institute of the University of Karlsruhe some axial and radial insulation breaks were calculated and optimized (Fig. 29). A cryostat insert for testing these insulation breaks electrically and thermohydraulically is under construction. Tests up to 46 kV at He temperatures and pressure cycles up to 2.5 MPa can be performed.

It was worked on the design of the model coil together with Alsthom. First of all all components were considered which were on the critical path of the manufacturing of the model coil. Problems concerning the impregnation technique, the mould, the pancake joints, the insulation system, the high voltage breaks, the conductor support in the joint area, the conductor terminations and the short circuit ring, were discussed in detail. A design for all these parts and the manufacturing technique is now available. Alsthom perfomed calculations for the pressure rise in the conductor during a quench. It was shown that the pressure did not exceed 30 MPa within 3 sec at a current of 15 kA. In this time the safety discharge is already completed. The pressure of 3 MPa was far below the pressure of 120 MPa which was obtained for adiabatic conditions. The four times lower pressure was caused by the compressibility of the helium.

Welding tests were performed between flanges and conductors in order to demonstrate that the conductor insulation inside was not damaged during the welding procedure. The tools for the winding procedure are available so that the winding fabrication test with the conduit can start.

Modifications of the test facility TOSKA

The taking into operation of the power switch system of 23 kV and 30 kA is still running. Some delay ocurred because the normal-conducting load coil was not available.

The support structure of the model coil and the short circuit ring in the TOSKA vacuum vessel were designed. The oscillation behaviour of the coil under the transient load during a fast discharge was calculated. This results in a bending of the coil of 14 mm, which entails shear stresses in the winding of 11 MPa.

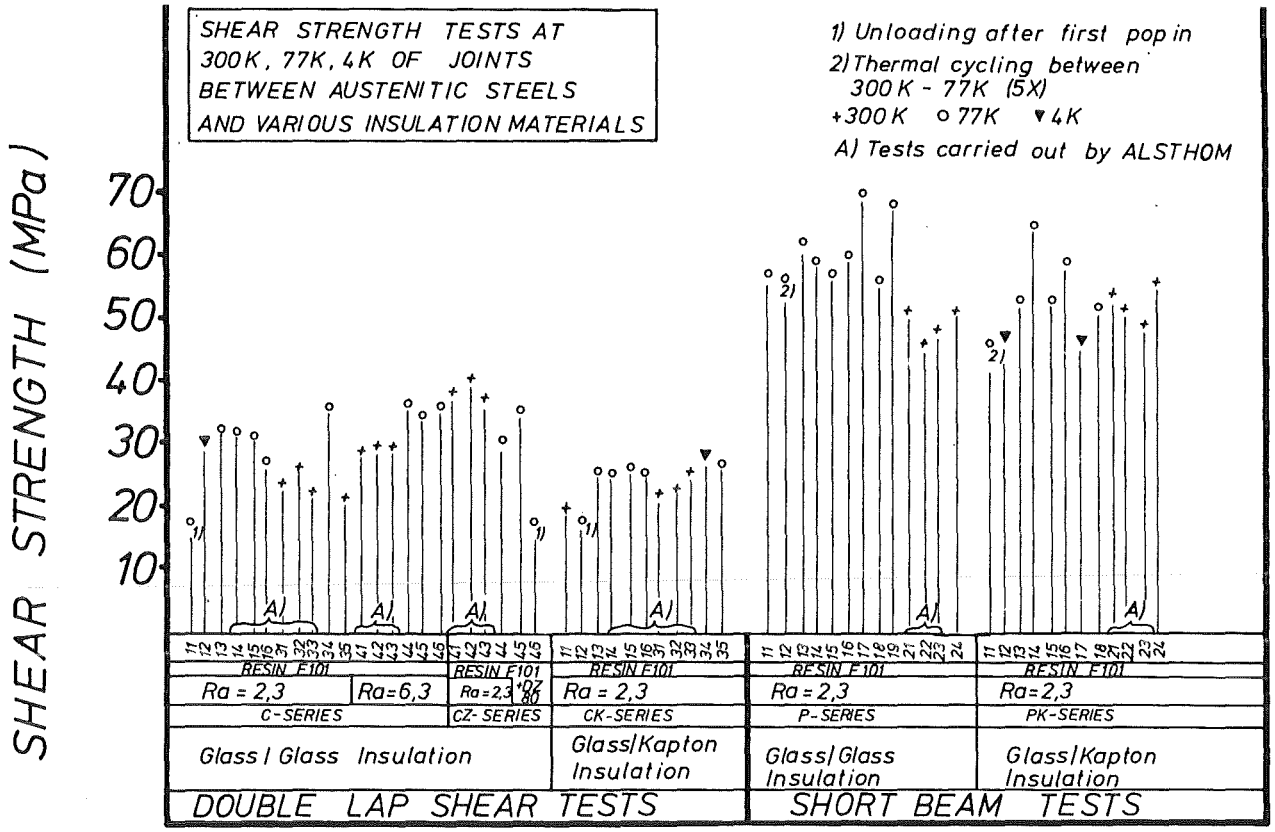

Fig. 28: Measurements of shear stresses of the insulation candidates glass fabrice/glass fabrice and glass fabrice/Kapton/glass fabrice for two sample geometries lap shear, short beam and 3 temperatures.

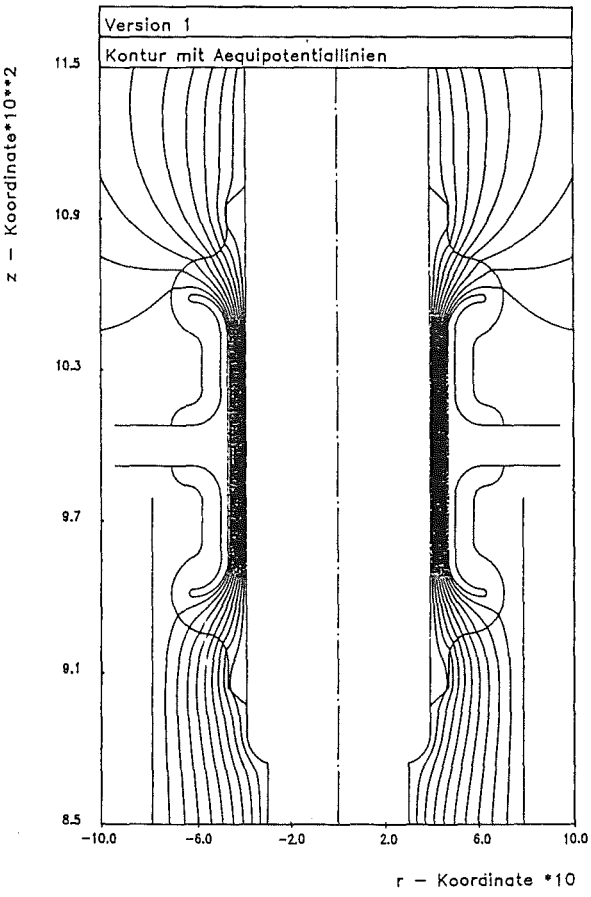

Fig. 29: Calculated equipotential lines for radial insulation break of the current feedthroughs of the model coil.

A software proposal was written for data acquisition system with the VAX computer. Diagrams for the acquisition of data in the different time windows during the discharge procedure in the different operation modes (inverter mode, safety discharge, high-voltage discharge, partial coil discharge and operation with and without electromechanical load) were outlined.

Staff:

H. Bayer	L. Schappals
I. Donner	G. Schenk
P. Duelli	C. Schmidt
S. Förster	K. Schweickert
P. Gruber	E. Specht
T. Hardy	H.-J. Spiegel
W. Heep	J. Seibert
U. Jeske	F. Süß
H. Katheder	M. Süßer
B. Mertens	A. Ulbricht
G. Nöther	D. Weigert
A. Nyilas	F. Wüchner
M. Oehmann	M. Wozniak
U. Padligur	V. Zwecker
R. Rietzschel	

M 8 Design and Construction of a Poloidal Field Coil for TORE SUPRA as NET-Prototype Coil

The objective of the task is the development and test of an Equilibrium Field Coil (EF Coil) with parameters relevant for NET. The reliable operation of a superconducting PF-coil shall be demonstrated in a real Tokamak environment with the rapid field variations due to start-up, plasma position control and disruptions. The development has to confirm the coil construction process proposed for NET on a fairly large scale.

For this purpose, the upper coil "E_h" of TORE SUPRA will be replaced by a superconducting coil "EHS". Design and construction will be based on the results of the already running task M 4.

A 12 kA vapour-cooled current lead designed and built for the TORE SUPRA coil by CEA Grenoble was tested at KfK in collaboration with CEA. The current-carrying conductor of vapour-cooled lead has two designs. One lead used a constant conductor cross-section and the other one a varying cross-section. A test cryostat and a 30 kA power supply were prepared and operated by ITP/KfK. The vapour-cooled leads were tested successfully up to 15 kA. The test was finished in December 87. Evaluations are running.

Cost estimation of the TORE SUPRA coil led to the result that a realization of the coil under the given specification is too expensive. A revision of the design using the experience of measurements and investigations (compare M 4, omitting all insulation materials in the conductor) is running.

Staff:
S. Förster
U. Jeske
H. Katheder
L. Schappals
G. Schenk
C. Schmidt

M 9 Structural Materials Fatigue Characterization at 4 K

Bulk material properties

In the reporting period mechanical tests have been carried out with the main objective to characterize the candidate bulk material properties at 4 K. The Cryogenic test rig was upgraded. The tensile testing unit is now capable to carry out tensile or fracture tests with four specimens simultaneously at liquid helium temperatures.

Preliminary results with the plate material 1.4429 (similar to 316 LN) show the interesting fact of the improvement of the cryogenic strength characteristics. This can be attributed partly to the heat chemistry and to some extent to the improved microstructure. Composition of the steel investigated here is shown in comparison with the material of the LCT Euratom coil casing in Table 9.

Especially the low sulphur content of the investigated material can be made responsible for the high 4 K fracture toughness performance. The high nitrogen content on the other hand shifts the tensile strength of the material to higher values. The obtained 4 K elasto-plastic J_I-integral results are shown in Fig 30.

Compared to the former plate material results (Euratom LCT) the increase of the critical J_I-value is obvious. The evaluated critical J_I-values for the rolling directions (TL) and perpendicular to this are ~ 420 N/mm and ~ 610 N/mm, respectively. The same Figure shows also the measured critical J_I-value of a forged block produced with the material 1.4429. It is evident that the critical J_I-value can be increased due to a microstructural refinement process (low quantity of impurities).

Material	C	Si	Mn	P	S	Cr	Ni	Mo	N
LCT plate	0,032	0,41	1,26	0,016	0,016	16,7	13,7	2,7	0,16
Investigated Material	0,023	0,34	1,50	0,028	0,003	16,8	12,6	2,6	0,17

Table 9: Heat chemistry of the nitrogen-strengthened stainless steel (1.4429) in weight %.

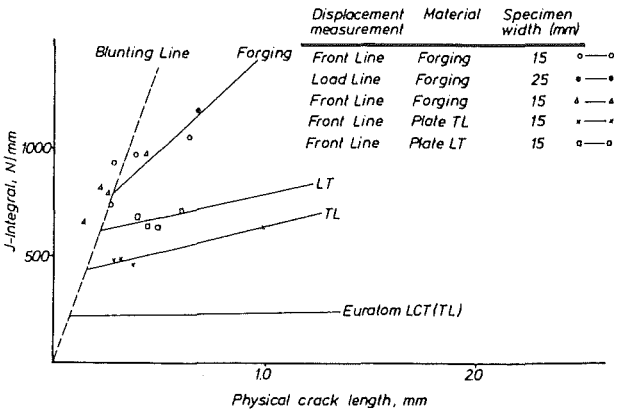

Fig. 30: J-integral values vs. the physical crack length obtained for the different heats of the material 1.4429 at 4 K

Tensile measurements at 4 K show also the enhanced tensile strength values of the investigated material. In addition, the difference between the yield and tensile strength is increased (by nearly a factor of three). This difference indicates higher fracture toughness of the materials. Table 8 shows the obtained tensile values at 4 K.

Material	Yield MPa	UTS MPa	Elongation %	Reduction of area %
LCT plate Mean of TL and LT	1195	1363	35	65
Investigated Material TL	932 926	1507 1527	41,8 40,6	53,8 53,8
Investigated Material LT	988 988	1527 1538	39,7 36,3	49,6 40,7

Table 8: Mechanical properties of the nitrogen- strengthened stainless steel (1.4429) measured at 4 K

The evaluation of these results is still going on. Machining of the different specimens from the materials 1.4306 and 1.4435 and the positioning of the specimens in the welds is under progress.

Staff:
S. Fischer
H.P. Raber
A. Nyilas

M12 Low Electrical Conductivity Structures Development

Fibre Composites with Radiation Resistant Matrices

With respect to low thermal and electrical conductivities polymeric fibre composites will be applied in fusion technology as magnet support elements, coil casing or spacers.

Materials used for those applications are polymeric fibre composites. Glass-fibre composites are cheap but exhibit a low bending tensile modulus; for carbon fibre composites the contrary is true. Many elements used in fusion technology are subjected to radioactive irradiation, which may cause degradation of the matrix. The highest resistivity against irradiation is exhibited by aromatic amin epoxy resins (EP), polyimides (PI), polyetherimides (PEI) and polyetheretherketones (PEEK). The latter are thermoplastic polymers, whereas PI exists as thermoplastic and duroplastic polymer. Recent studies revealed that just those matrices exhibit a rather good fibre-matrix bond, which is reflected in a high interlaminar shear strength τ_{ILS}. Values of τ_{ILS} up to 190 MPa at 4.2K were achieved with PEEK matrices. Common standard matrices allow for values of about 120 MPa. Also the bending modulus is rather high.

Results

With respect to applications in fusion technology only matrices with a high resistance against radioactive irradiation were used (dose $\approx 5\text{-}10 \cdot 10^8$ gray).

The following properties were investigated:

Tensile fracture strength σ_t, tensile modulus E_t, tensile fracture strain ε_t (note for comparison that composites with 0/90° fibre arrangement theoretically should have about half the tensile fracture strength and half the tensile modulus of a unidirectional composite).

matrix	fibres	arrange-ment	σ_t MPa	E_t GPa	ε_t %	T K
EP	fibre glass	0/90°	420	26	2.2	293
			880	40	3.1	77
			930	39	3.8	5
PEI	"	"	683	31	2.8	293
			988	35	4.0	77
			1050	35	4.2	5
PEEK	carbon fibre	0°	2080	142	1.5	293
			2270	155	1.6	77
			2330	159	1.5	5

Table 10

Composite properties:

The mechanical fibre glass properties are strongly increased at low temperatures. A bending modulus (E_b) at 77K of about 47 GPa was achieved with fibre-glass/EP composites.

These results demonstrate that these materials will be promising candidates for application in fusion technology.

Further investigations of the fatigue behaviour of those composites are in preparation. The electrical conductivity of carbon fibre composites is another topic of measurements.

References:

G. Hartwig, Fibre Properties, Cryogenics, to be published April 1988; K. Ahlborn, Fatigue behaviour of carbon fibre reinforced plastic at cryogenic temperatures, Cryogenics, 28 (1988), pp.267; K. Ahlborn, Cryogenic mechanical behaviour of a thick walled carbon fibre, Cryogenics, 28 (1988), pp.273 ; S. Knaack, reinforced plastic structure, Cryogenics, to be published April 1988.

Staff:

K. Ahlborn
J. Fischer
G. Hartwig
S. Knaack
A. Nyilas
H.P. Raber

MAT1.6 Development and Qualification of MANET 1

In order to qualify the NET-heat MANET 1 (Steel 1.4914; Chg. 5.3645) the dynamic toughness of charpy V-specimens is measured in instrumented notch impact bending tests. The ductile to brittle transition temperature (DBTT) is 25°C, and the upper shelf energy (USE) is about 130 Joule. These values are in a normal range of such a steel with a heat treatment of 950°C/2h + 1075°C/0.5h + 750°C/2h. The DBTT for subsize charpy V-specimens (3x4x27mm) is found to be 0°C, because of the smaller ligament and the lower constraint in comparison to the full size (10x10x55 mm) Charpy-V-specimens.

Staff:
B. Dafferner
L. Schäfer
C. Wassilew

MAT 1.9 Pre- and Post-Irradiation Fatigue Properties of 1.4914 Martensitic Steel

Thermal cycling of large components is a serious problem for the designer. The structure considered in the present case is the first wall of a fusion reactor. Its surface, in the present design concept, will be subjected to radiation heating from the plasma facing graphite tiles, which may lead to severe thermal stresses. Due to the discontinuous operational mode thermal cycling will generate oscillating temperature gradients. These, depending on the loading conditions, will cause elastic or elasto-plastic reversed deformation giving rise to thermal fatigue which at present is considered as the most detrimental lifetime-limiting phenomenon for the structure considered. The investigations of MAT 1.9 are devoted to this problem.

In the absence of stress gradients (idealized case) the so-called mechanical loading equivalent for thermal cycling can be obtained from calculations. Such investigations, in which calculated strain cycles are imposed on test specimens at a constant temperature in MAT 1.9, precede the actual thermal cycling fatigue tests. These were already described the previous Semiannual Report.

The studies to be reported within MAT 1.9 are:

- Fabrication and testing of GRIM specimens of MANET 1 (W.Nr. 1.4914).
- Calculations of the strain distribution in GRIM-specimens and the estimate of the reference length L_G for these specimens.
- Operational start of the first thermal cycling test rig.
- Calculation of the isothermal temperature distribution in the H-GRIM-specimen to be used in T-cycling experiments.

1. Isothermal fatigue

For the fabrication of H-GRIM specimens the requirements concerning precision are higher as compared to the manufacturing of solid specimens (S-GRIM). A very good indicator for sample quality is the standard deviation of the number of cycles to failure N_f in LCF-tests. This standard deviation is given in Table I for three different materials (AISI 304, AISI 316L and W.Nr. 1.4914) and two types of specimens (H-GRIM and S-GRIM samples). Therefrom it is obvious that these values are relatively small and comparable with those of other plastic properties e.g. the yield strength. Probably the somewhat higher standard deviation for the martensitic specimens is material specific.

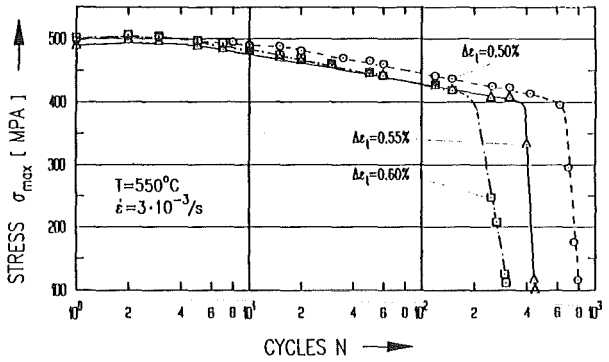

Fig. 31: Maximum tensile stress vs. number of cycles for W.Nr. 1.4914(H-GRIM-Specimen)

The influence of strain range $\Delta\varepsilon_t$ upon the number of cycles to fracture N_f of martensitic H-GRIM specimens is shown in Fig. 31. The variation of the strain range ($\Delta\varepsilon_t$ = 0.5 over 0.55 to 0.6%) causes only a slight increase of maximum tensile stress σ_{max}. The N_f-values, however, decrease significantly with $\Delta\varepsilon_t$ from 794 over 446 to 305. Since the stress σ_{max} is rather independent of $\Delta\varepsilon_t$ it is expected that in contrast to the austenitic steel AISI 316L for the martensitic material loaded under the same conditions the fatigue damage is the dominant failure mechanism.

2. Temperature cycling experiments

The first test rig consisting of a heating device, a load frame and the data acquisition system - containing also the load and strain transducer feeding electronics - is under operation since the beginning of 1988. A preceding test program was defined, to examine the axial temperature distribution during static temperature loading in a temperature range

Material	Type of specimen (S=solid) (H=hollow)	Strain range [%]	Mean value Nf	Standard deviation [%]	Number of samples
AISI 304	H-GRIM	1.0	200	± 6	6
AISI 316L	H-GRIM	0.6	2230	± 6	6
(ISPRA)	H-GRIM	0.6	2290	± 4	8
1.4914	S-GRIM	1.0	12001	± 8	4
1.4914	S-GRIM	1.0	16202	± 5	6

Table 11: Reproducibility of N_f for different materials ($T = 550\,°C$, $\dot{\varepsilon} = 3 \cdot 10^{-3}$/s)

1 Fabrication after heat-treatment
2 Fabrication before heat-treatment

between 250 °C and 550 °C as well as during cyclic temperature loading in the same temperature range. The additional test conditions of the cyclic tests are: Constant ΔT = 300 °C and heating and cooling rates of 1 to 10 K/s.

For the examination of the above parameters an H-GRIM-specimen was prepared with seven thin Ni-CrNi-thermocouples welded to the test specimen as indicated in Fig. 32.

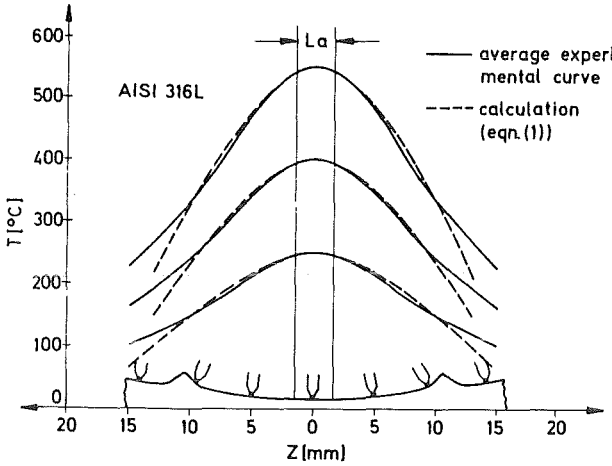

Fig. 32 : Comparison of experimental and calculated axial temperature distribution of isothermal H-GRIM specimen at250 °C, 400 °C and 550 °C

The thermocouple at z = 0 was used as the control element. In addition to the reading of the seven thermocouples the electrical current and the thermal elongation of the sample and that of the watercooled pullrods were measured.

The experimental data at 250 °C, 400 °C and 550 °C are plotted in Fig. 32 and compared with numerical calculations. These are based on the assumption of uniform heat generation (along the length of a cylinder) of longitudinal heat transfer by conduction and of radial heat transfer by convection and radiation respectively. The solution of the energy balance equation for an infinitesimal element dz of a hollow cylinder leads to

$$(d^2T/dz^2) - (hp/\lambda A)(T-T_r) + (I^2/A^2\sigma\lambda) = 0 \qquad (1)$$

with : h = Newton heat-transfer coefficient; p = cylindrical circumference; λ = coefficient of heat conduction of a solid; A = cross section of the hollow cylinder; T_r = room temperature; I = electrical current; σ = electrical conductivity.

Because the hourglass shape of the H-GRIM-specimen has to be taken into account a numerical integration of the differential equation (1) by Euler's method was applied to obtain the dotted curves in Fig. 32. There is considerable agreement between measurement and calculations for the middle part of the gauge length.

The z(T)-dependence leads to ΔL[z(T)]-dependences which can be evaluated numerically from the equation:

$$\Delta l_{T,i} = (\alpha_{(T)}(T-20) - 5\alpha_{(20)})\,\Delta z_i \qquad (2)$$

with : α = linear thermal expansion coefficient; T = actual temperature for a Δz_i interval = 1mm. Summarizing the contributions of each interval, this leads to :

$$\Delta L[z(T)] = 2 \Sigma \Delta l_{T,i}$$

where ΔL[z(T)] is the total elongation due to heating.

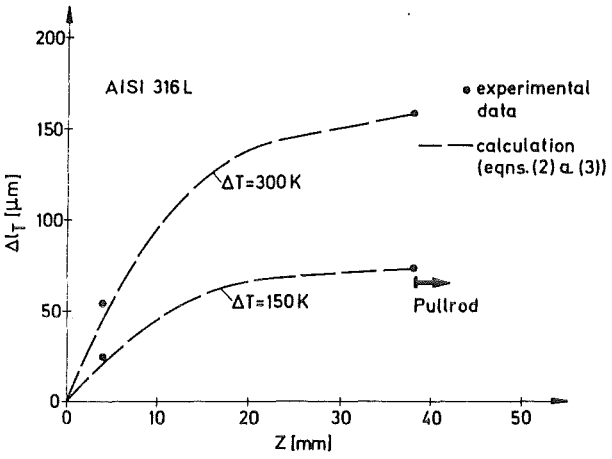

Fig. 33: Axial thermal elongation of the half H-GRIM specimen for aΔT of 150K and 300K on the basis of 250 °C-values

The factor 2 takes into account the symmetry of temperature distribution with respect to z = 0. Fig. 33 shows the additional amount of thermal elongation for two ΔT-values, as a function of z, where the thermal elongation Δl_T generated by the temperature distribution at 250 °C was set to O. The comparison between calculation and measurement is performed for two ΔT-values of (150 °C and 300 °C). The measured values are available for z = 4mm and for 38mm. The discrepancy between calculation and measurement at z = 4mm is rather high.

3. Strain distribution in S- and H-GRIM specimens

In order to compare deformation data from GRIM specimens (index G) with those from cylindrical specimens (index C) it is necessary to settle a reference length L_G for GRIM specimens so that for a given strain ε_C (which is independent of the specimen - axis z, see Fig. 34) a corresponding strain ε_G results for which it is

$$\varepsilon_C = \Delta L_C/L_C = \varepsilon_G = \Delta L_G/L_G. \qquad (3)$$

L_C is the reference length of the cylindrical specimen and ΔL_C, ΔL_G are the corresponding length changes.

First the strain distributions ε(z) for S- and H-GRIM specimens were calculated for elastic and ideally plastic unidirectional deformation respectively.

3.1 Elastic deformation

3.1.1 S-GRIM specimens

The strain distribution $\varepsilon_S(z)$ for S-GRIM specimens is derived from

$$\sigma_{e,S}(z) = F/A_S(z) = E\varepsilon_{e,S}(z), \qquad (4)$$

F is the (tensile) force, $A_S(z)$ is the cross section, E is Young's modulus and $\varepsilon_{e,S}$ is the elastic strain (the index e denotes elasticity). From Fig. 34 one derives

$$A_S(z) \doteq A_{S,o}(1+q_S z^2) \qquad (5)$$

with $q_S = 1/(\rho_S R_{S,o})$, where (see Fig. 34) ρ_S is the radius of curvature and $R_{S,o}$ is the specimen radius for z = 0 which is equal to the radius R_C of the cylindrical specimen.

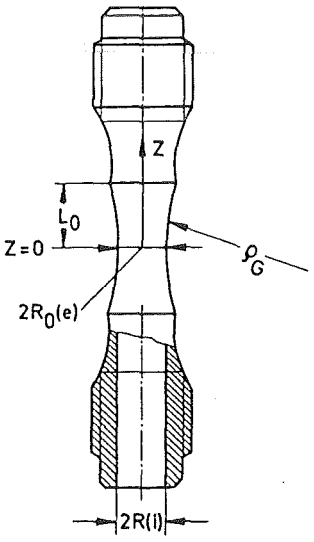

Fig. 34 : Scheme of S- and H-GRIM specimen respectively

Combining (4) and (5) it is

$$\varepsilon_{e,S}(z) = \varepsilon_{S,o}/(1+q_S z^2), \qquad (6)$$

where $\varepsilon_{S,o} = F/EA_{S,o}$ is the strain of the cylindrical specimen for the same force F and the cross section $A_{S,o}$. The graph of Eq. (6) is shown in Fig. 35, curve (a)

.We define a mean strain by

$$\varepsilon_{e,S} = \frac{1}{L} \qquad (7)$$
$$0\int_0^{L_0} \varepsilon_{e,S}(z)\,dz$$

where L_0 is half the distance between the shoulders of the GRIM specimen (see Fig. 34). Inserting (6) into (7) it is

$$\bar{\varepsilon}_{e,S} = (\varepsilon_{S,o}/L_0\sqrt{q_S})\,\mathrm{arctg}(L_0\sqrt{q_S}). \qquad (8)$$

For $L_0 = 10.5$ mm, $\rho_S = 100$, $R_{S,o} = 4{,}4$ mm we obtain

$$\bar{\varepsilon}_{e,S}/\varepsilon_{S,o} = 0.93 \qquad (9)$$

Inserting this value into Eq. (6) the corresponding z-value is

$$z_{e,S} = 5.75 \text{ mm} \qquad (10a)$$

or

$$z_{e,S}/L_0 = 0.55 \qquad (10b)$$

(see crosses in Fig. 35).

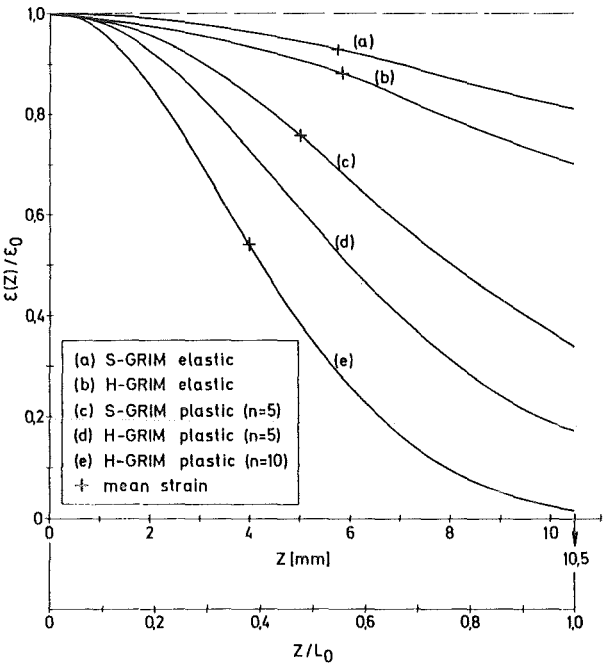

Fig. 35 : Axial distribution of elastic and plastic strain ratio for both types of GRIM specimens.

3.1.2 H-Grim specimens

Similarly to Eq. (5) one obtains for the cross sections of H-GRIM specimens (see Fig. 35).

$$A_H(z) \doteq A_{H,o}(1+q_H z^2) \qquad (11)$$

with $q_H = 1/[2\pi R_o(e)\,\rho_H\,(1-R(i)/R_o(e))]$ where $R_o(e)$ is the external and R(i) the internal radius for z = 0. $A_{H,o}$ is the cross section for z = 0. By means of Eq. (8) we obtain, replacing the indexation by that of H-GRIM notation, for L_o = 10.5 mm, ρ_H = 100 mm, R_o (e) = 4.4 mm and R(i) = 4.0 mm. $\bar{\varepsilon}_{e,H}/\varepsilon_{H,o} = 0.88$ and $z_{e,H} = 5.85$ mm or $z_{e,H}/L_o \doteq 0.56$

The z_e-values for both types of specimens are approximately the same (see Fig. 35).

3.2 Plastic deformation

For high temperature plasticity the following relationship holds between the plastic strain rate $\dot{\varepsilon}_p$ and the yield stress σ_y

$$\dot{\varepsilon}_p \sim \sigma_y^n,$$

where $10 \geq n \geq 4$ is the stress exponent. If the work hardening behaviour as well as other relevant properties are the same for cylindrical and GRIM-specimens, according to the above we obtain

$$\dot{\varepsilon}_p(z)/\dot{\varepsilon}_{p,C} = (\sigma_y(z)/\sigma_{y,C})^n = \varepsilon_p(z)/\varepsilon_{p,C} \qquad (12)$$

where $\dot{\varepsilon}_{p,C} = \dot{\varepsilon}_{p,o}$ and $\varepsilon_{p,C} = \varepsilon_{p,o}$ $\varepsilon_{p,C} = \varepsilon_{p,o}$ .The index o refers to GRIM-specimens for z = o. Hence $\dot{\varepsilon}_{p,o}$, $\varepsilon_{p,o}$ is the strain rate and strain of the corresponding cylindrical

specimen loaded to the yield strength $\sigma_{y,C} \neq f(z)$ resp. This is equal to the yield strength $\sigma_{y,o}$ of the GRIM-specimen for z = o.

For ideal plasticity $\sigma_{y,C}$ belongs to the elastic region and so does the stress $\sigma_y(z)$. In order to preserve the geometry of the specimen, the unidirectional plastic loading must be restricted to a very small time interval, i.e. $\varepsilon_p \leq \varepsilon_e$. Denoting by ε_y the plastics train for $\sigma = \sigma_y$ we obtain according to Eq. (12)

$$(\sigma_y(z)/\sigma_{y,o})^n = (\varepsilon_y(z)/\varepsilon_{y,o})^n \approx \varepsilon_p(z)/\varepsilon_{p,o} \qquad (13)$$

where $\sigma_y(z) = F_y/A(z) = \varepsilon_y(z)E$ and $\sigma_{y,o} = F_y/A_o = \varepsilon_{y,o}E$

Rewriting Eq. (13) it is

$$(A_o/A(z))^n = (\varepsilon_e(z)/\varepsilon_{e,o})^n \approx \varepsilon_p(z)/\varepsilon_{p,o} \qquad (14)$$

and consequently $\varepsilon_p(z)$ depends upon the material parameter n.

In Fig. 35 strain distributions $\varepsilon_p(z)/\varepsilon_{p,o}$ are shown for both types of GRIM specimens. Notice , that with increasing n, due to the high stress sensitivity of $\dot{\varepsilon}_p$, the plastic strain ε_p concentrates in the middle section of the GRIM specimens (Triggering effect due to sample's geometry;. note that GRIM specimens are unstable in plastic tension).

For the mean values one obtains

$$\bar{\varepsilon}_{p,S}/\varepsilon_{p,o} \doteq (1/L_o\sqrt{nq_S})\,\mathrm{arctg}\,(L_o\sqrt{nq_S}). \qquad (15)$$

For n = 5, $q_S = 2{,}3\cdot10^{-3}$ mm^{-2}, $L_o = 10.5$ mm it is $\varepsilon_{p,S}/\varepsilon_{p,o} = 0.75$ the corresponding $\bar{z}$-value is $\bar{z}_{p,S} = 5$ mm or $\bar{z}_{p,S}/L_o = 0.48$

The mean strain for the H-GRIM specimen replacing the indexation in eq. (15) by that of H-GRIM notation, is for n = 10, $q_H = 4\cdot10^{-3}$ mm^{-2}, $L_o = 10.5$ mm

(curve (e) in Fig. 5): $\bar{\varepsilon}_{p,H}/\varepsilon_{p,o} = 0{,}54$ and $\bar{z}_{p,H} = 4$ mm or $\bar{z}_{p,H}/L_o = 0.38$.

3.3 The reference length L_G

From Eq. (4) we have

$$\sigma_{G,o} = F_G/A_{G,o} = (\Delta L_G/L_G)\,E = \varepsilon_{G,o}E \qquad (16a)$$

and

$$\sigma_C = F_C/A_C = (\Delta L_C/L_C)\,E = \varepsilon_C E \qquad (16b)$$

L_G is considered as a reference length the value of which is determined by means of particular conditions. In the present case L_G is considered as a length which defines a given strain ε_C.

Make sure that the material properties of the samples to be compared are the same and set

$$L_G = L_o = L_C, \qquad (17)$$

where L_C is the well defined reference length of a cylindrical specimen. Define by $\varepsilon_{G,o}$ the strain of a GRIM specimen at z = 0 and put $\varepsilon_C = \varepsilon_{G,o}$ .i.e. for the corresponding elongations it is $\Delta L_C = \Delta L_G$.

Then from Eq. (16) it is

$$(F_C A_{G,o}/F_G A_C) \equiv \Lambda = 1, \qquad (18)$$

where F_G, F_C are the forces correlated with ΔL_G, ΔL_C respectively. Eq. (18) can be checked experimentally. If $\Lambda \neq 1$ then the assumption of Eq. (17) is not obeyed. It is easily shown that

$$\Lambda \begin{cases} > 1 \text{ for } L_G < L_o \\ = 1 \text{ for } L_G = L_o \\ < 1 \text{ for } L_G > L_o \end{cases} \qquad (19)$$

For $\Lambda \neq 1$ we have $\Lambda x = 1$, where $x = \varepsilon_{G,o}/\varepsilon_C = 1/\Lambda \neq 1$

and therefrom it is $\Delta L_C/L_C = \varepsilon_C = \varepsilon_{G,o}\Lambda = (\Delta L_G/L_G)\Lambda$.

Putting $\Delta L_G = \Delta L_C$ we have finally

$$L_G = L_C/\Lambda . \qquad (20)$$

Hence the reference length can be obtained from measurable quantities.

Due to a preliminary comparison by means of data from experiments conducted in the past on S-GRIM and cylindrical specimens resp. it follows, that $L_G \approx \bar{z}_{e,S} \approx 6\,\mathrm{mm} = 0.57\,L_o$, (see Eq. (10a)) and therefrom $\varepsilon_{e,C} \approx \bar{\varepsilon}_{e,S} = \Delta L_G/z_{e,G}$.

Accordingly in order to achieve comparable conditions, for GRIM specimens the value $\varepsilon_{e,C}$ should be taken equal to $\bar{\varepsilon}_{e,S}$ consequently we obtain

$$\Delta L_G = \bar{\varepsilon}_{e,S}\,\bar{z}_{e,S} . \qquad (21)$$

Experiments are on the way to check the present calculations. Moreover, these should also give evidence whether the present results obtained for unidirectional loading are applicable for cyclic strain loading as well.

Unpublished investigations conducted by Hornberger and Tinivella have shown that far above of total strains applied in LCF loading for both the types of GRIM specimens the ratio tangential to axial stress, $\sigma_\theta/\sigma_Z \approx 10^{-5}$. Therefore, the stress state is practically uniaxial. This result is a prerequisite for the calculations presented above.

Staff:
W. Baumgärtner
M. Boček
C. Petersen
D. Rodrian
W. Scheibe
R. Schmitt
H. Schneider
W. Schweiger

MAT1.11 Post-Irradiation Fracture Toughness of Type 1.4914 Martensitic Steel

It is found that for various similar heats the DBTT after irradiation at temperatures in the range of 150-320°C increases to ~ 140°C

MAT 2.2 In-Pile Creep-Fatigue Testing of Type 316 and 1.4914 Steels

In-reactor deformation behavior of 1.4914 and 316 L steels under cycling load.

It is planned to study the in-reactor deformation and fracture behavior of the two candidate structural materials, namely 1.4914 and 316 L, under the conditions of load cycling in tension. The irradiation will be performed in the central position of KNK II.

The first in a series of several irradiations is now scheduled for 1989. The aim of this irradiation, denominated LOADCYCLE 1.36-5, is to show which of the two possible in-pile creep mechanisms, namely classical irradiation-creep or radiation-enhanced thermal creep, will be dominant in the martensitic steel 1.4914 under the imposed irradiation and stress conditions. A comparison of the deformation under load cycling will be made with dimensional changes resulting from constant load experiments with stress levels $\bar{\sigma}$ and σ, which correspond to the effective stress for the two deformation mechanisms mentioned above. The proposed loading scheme is summarized in Tab. 11.

The minimum achievable specimen temperature is dictated by the γ-heating and amounts for this experimental set-up to 450-475°C for the specimen A-D and about 500°C for E-H at a reactor power of 60%. Fig. 36 shows in addition the temperature variation of the capsules A-H for the case of 100% reactor power and the axial neutron flux distribution.

The exact load levels $\bar{\sigma}$ and $\tilde{\sigma}$ and the variation of the inner pressure Δp with time will be decided upon after prerunning out-of-pile experiments and model calculations.

Material	Load conditions	Specimen denomination	
		at 475°C*	at 550°C*
Manet (1.4914)	Cycling load Δp [Δp 10-400 bar, t_p ~ 100 s]	A, C	E, H
	Constant load σ [σ is calculated from classical IPC mechanisms]	B	F
	Constant load σ [σ is calculated according to the "Enhanced thermal creep" model]	D	G

Tab. 11: Proposed loading scheme and test conditions for experiment LOADCYCLE 1.36-5 in KNK-II central position

Staff:

K. Ehrlich,
G. Reimann,
L. Schmidt

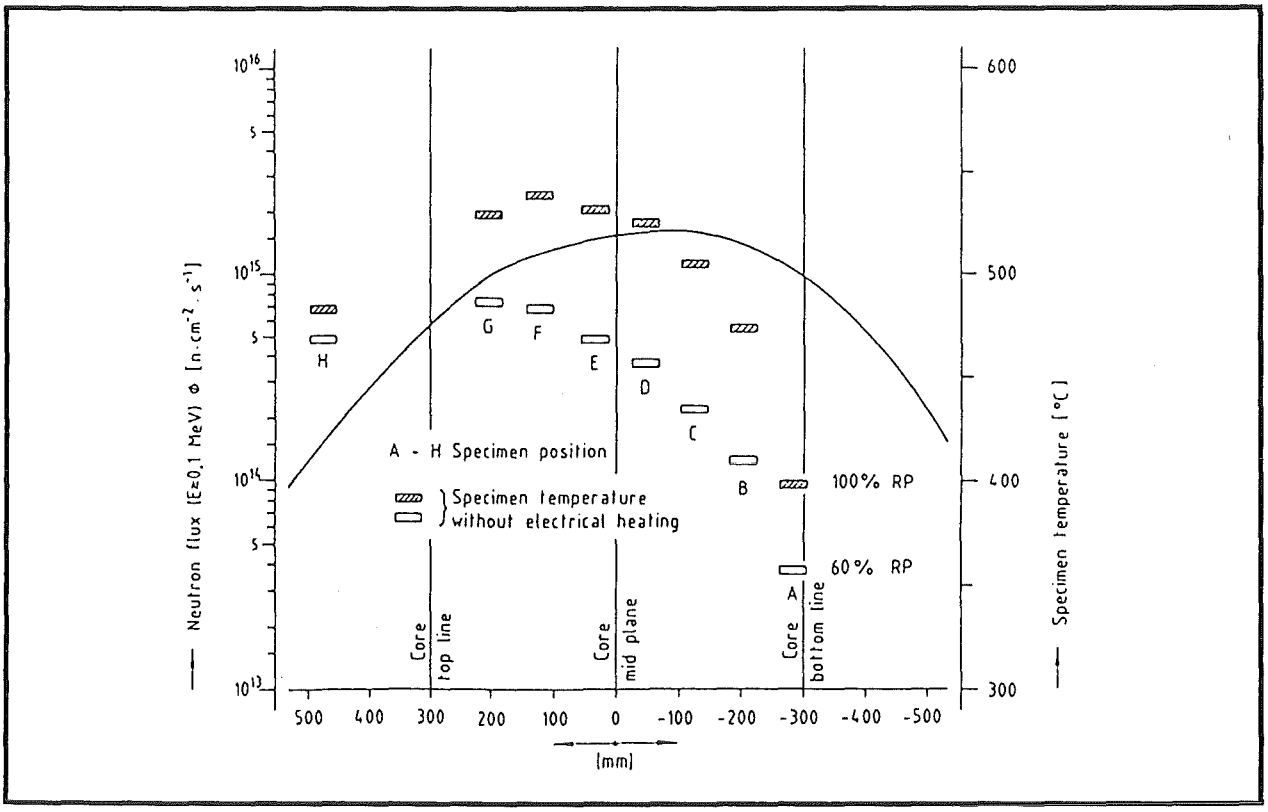

Fig.36: Neutron flux distribution and γ-induced specimen temperatures in the pressurized tube test facility in KNK-II central position (RP = reactor power)

MAT 6/MAT 13 Ceramics for First Wall Protection and for RF Windows

SiC qualities of industrial manufacturers are to be tested concerning the durability of tiles to protect the first wall against plasma instabilities and disruptions. Insulator materials (like Al_2O_3, $MgAl_2O_4$, AlN) are to be selected with regard to their resistance to thermal crack formation by dielectric loss in RF-windows. These windows shall be applied to separate wave guides for ECR heating from the plasma vacuum.

Measurements of the mechanical properties of SiC were continued. Fig. 37 gives a survey of Young's modulus data of different SiC types and charges. The influence of the microstructure appears to be governed by the porosity. Some high temperature bending tests on SSiC and HIP-SiC samples at 1400 °C resulted in mean bend strengths of 350 and 440 MPa, which are still in the scattering range of the room temperature data.

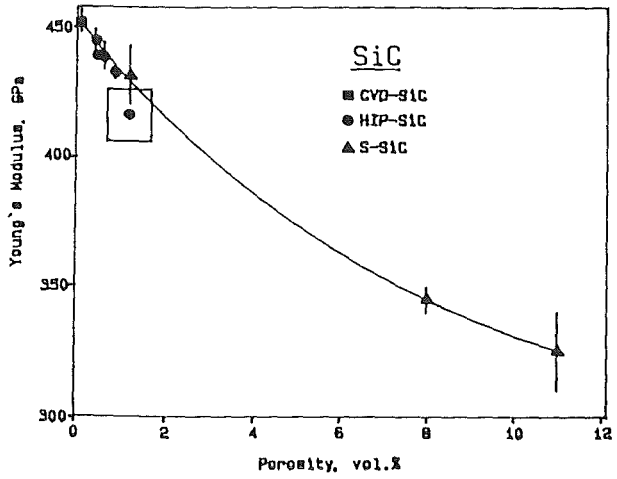

Fig. 37: Young's modulus of different SiC types and charges as a function of the porosity.

Concerning the resistance to thermal crack formation an estimation was made for SiC, which was based on the relevant property data measured and on some results of thermal shock tests at KFA Jülich. The critical stationary heat fluxes estimated are about 50 W/cm², and 70 W/cm² at the maximum. Concerning the plasma disruption conditions, cracking of SiC can hardly be excluded, but it seems that SiC with some wt.% AlN, which is being investigated at KFA Jülich, could endure. The main deteriorating influence of neutron irradiation is probably the decrease of the fracture strength which is still to be examined. The HFR irradiation experiment D217/1 (1200 °C, $1x10^{22}$ n/cm²) will be demounted end of March 1988.

As already reported, the evaporation of Si from SiC will restrict the operation temperature to the range ≤ 1700 °C. Fig. 38 shows the penetration rate of the decomposition dependent on the annealing time. The evaporation process leaves a carbon layer on the SiC body. In view of the high evaporation rate on the fresh surface one can expect, that in a fusion reactor the particle erosion rate of SiC near 1700 °C would be similar to that of graphite, but no worse on the other hand.

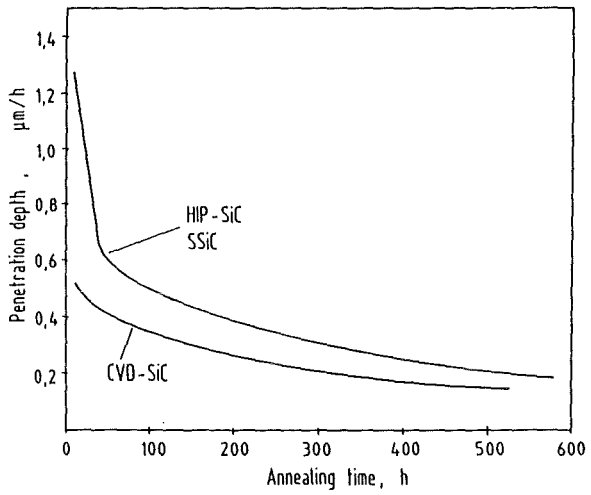

Fig. 38: Penetration rate of Si evaporation from SiC dependent on the annealing time (in high vacuum).

Different sintered SiC-materials have been chemically analyzed . Not only main components, but also metallic and nonmetallic impurities have been determined.

Several different charges of SiC have been examined for their thermal diffusivity a up to high temperatures. The room temperature value varies in the following manner: a = 0.561 cm²/sec (HIP-SiC A), a = 0.607 cm²/sec (HIP-SiC B), a = 0.447 cm²/sec (CVD-SiC). Above 900 K all effects influencing the thermal conductivity by lattice defects at lower temperatures diminish, and the thermal conductivity is independent of parameters concerning the preparation of the material. The thermal expansion has been measured on HIP-SiC up to 1100 K and follows the equation:

$$\Delta l/l_0 = -0.00126 + 4.05 \cdot 10^{-6} T; [T] = K; R.T. < T < 1100 K$$

The thermal diffusivity of neutron-irradiated HIP-SiC ($2.6 \cdot 10^{20}$ n/cm², 475 K) was measured in the laser-flash-equipment. The results are shown in Fig. 39.

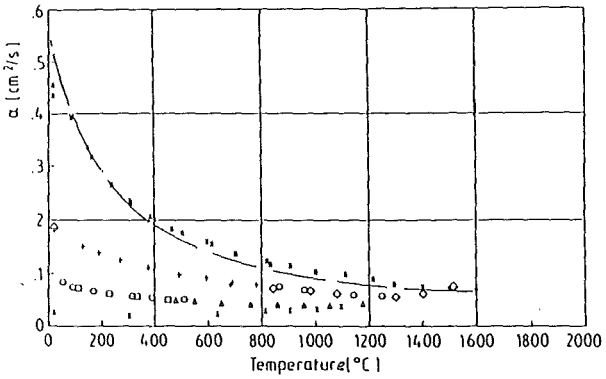

Fig. 39: Thermal diffusivity a of irradiated HIP-SiC measured in consecutive cycles from R.T. up to 1200 - 1500 °C, compared to unirradiated material (curve).

Concerning alumina window materials, it was shown that for AL 23, BIO-Al_2O_3 and sapphire the thermal conductivity from R.T. up to 1700 K follows the relationship

$$\lambda = (a + bT)^{-1}$$

Material	a (cmK/W)	b (cm/W)
AL 23	- 0.240	0.0108
BIO	+ 1.00	0.0100
Sapphire (c⊥heat flow)	+ 0.326	0.00958

Table 12

Neutron-irradiated AL 23 ($2.6 \cdot 10^{20}$ n/cm^2 at 475 K) has a much lower thermal conductivity, which recovers beyond 1275 K (Fig. 40). After complete annealing, the inverse of the thermal conductivity - temperature function shows the same slope (0.0108 cm/W) as the unirradiated material. The data are fully compatible with the simple Debye-theory of thermal conductivity of insulators, indicating that neutron irradiation may decrease the thermal conductivity of α-Al_2O_3 to a temperature-independent minimum value of 0.02 - 0.05 W/cmK.

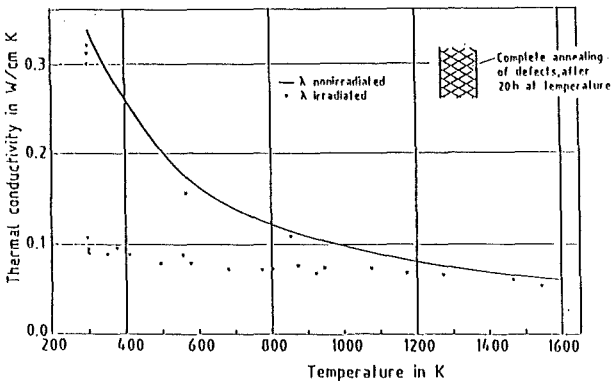

Fig. 40: Thermal conductivity of irradiated and nonirradiated α-Al_2O_3 (AL 23).

Especially for irradiated window materials etching methods have been developed for all candidate materials (Al_2O_3, $MgAl_2O_4$, AlN) which allow to reveal the microstructure at a temperature as low as ~ 475 K, in order to avoid recovery effects.

Concerning the investigation of ceramic insulator materials for RF windows a comprehensive study has been started for the dielectric properties at 40 - 50 MHz observed in materials suitable in structural parts for Ion Cyclotron Resonance Heating. Steatite ceramics (aluminium silicate based), which are considered for use at a first stage, have only a moderately low dielectric absorption ($\varepsilon_r' \approx 6$, $\tan\delta = 16 - 22 \times 10^{-4}$). Much better performance is found in pure alumina grades that reach $\tan\delta < 1 \times 10^{-4}$ and single crystals (Al_2O_3, $MgAl_2O_4$) that fall below the resolution minimum in loss ($\tan\delta < 0.3 \times 10^{-4}$). Machinable ceramics were compared for their potential as alternative structural materials. While STENAN (silicate based) and MACOR (glass/mica based) showed elevated dielectric loss, SHAPAL-M (AlN based) exhibited an attractively low loss figure ($\tan\delta = 4.1 \times 10^{-4}$).

In the dielectric measurements at 30 - 40 GHz, emphasis was given to materials that may improve the physical parameters decisive for the limitations of transmission windows in Electron Cyclotron Resonance Heating. The lowest values for $\tan\delta$ found in polycrystalline and single crystal alumina amounted to 3 - 5×10^{-4}. In new samples of sintered, translucent AlN promising $\tan\delta$ values were found, 10×10^{-4} instead of $> 40 \times 10^{-4}$ in hot isostatically pressed (HIP) materials. The sintered grade excelled from the HIP grade also in thermal conductivity and mechanical strength. Studies of AlN samples sintered at our institute indicated that dielectric loss is not strongly influenced by grain size and low porosity (< 10 %) but by the time and the temperature of the sintering process.

Staff:
Ch. Adelhelm
M. Blumhofer
W. Dienst
G. Gausmann
Ch. Gosgnach
G. Haase
R. Heidinger
V. Karcher
K.-H. Kurz
D. Linder
B. Schulz
H. Zimmermann

MAT9.2 Investigation of Fatique Under Dual -Beam Irradiation

The Dual-Beam Facility of KfK was developed as a research tool for materials within the European Technology Programme. The Dual-Beam Technique allows the production both of damage and helium in thick specimens by simultaneous irradiation with high energy protons ($\leq$ 40 MeV) and alpha particles ($\leq$ 104 MeV) produced by KfK cyclotrons. One of the objectives is to investigate the influence of helium on the mechanical properties of first-wall materials.

1. Development of the Irradiation Facility

In the reporting period the helium loop for the sample-cooling during the irradiations was supplemented by a by-pass in order to guarantee a high purity of the helium gas

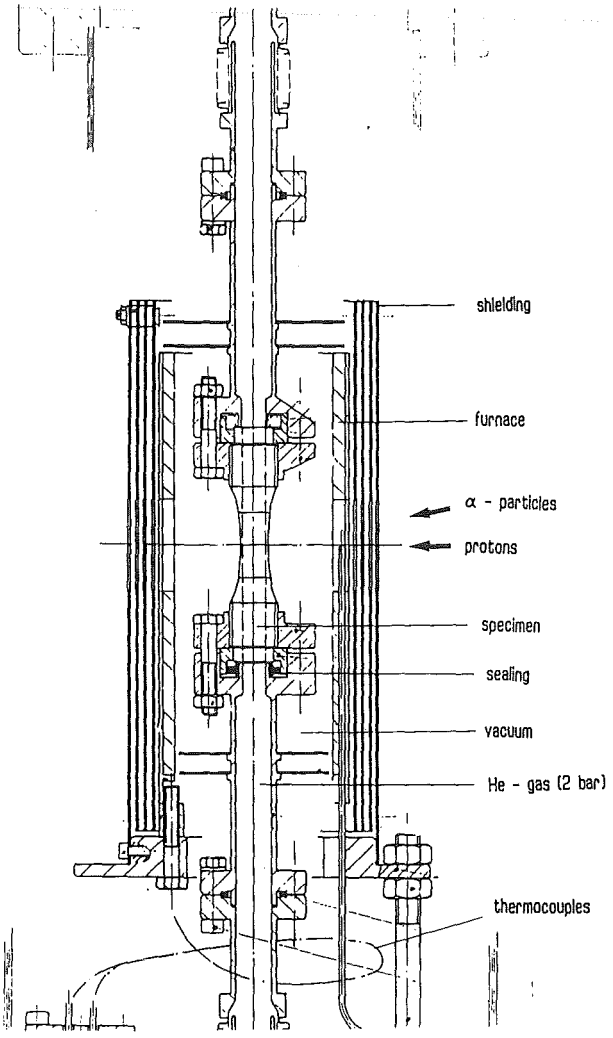

Fig.41: Dual-beam postirradiation device for LCF-specimes

even after several days of operation. The main loop was successfully tested together with this by-pass during a dual-beam test irradiation of a H-GRIM-LCF-specimen at helium pressures between 1 and 3 bar and at gas velocities up to 94% of the helium sound velocity.

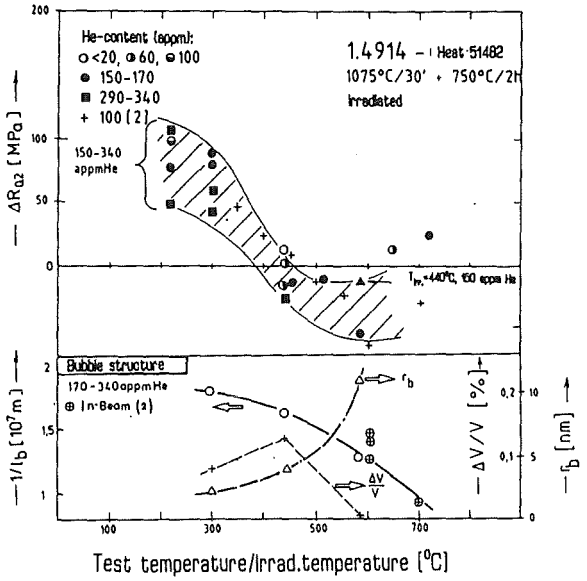

Fig.42: Change in yield strength $\Delta R_{0.2}$ and helium bubble evolution after helium implantation

Concerning the irradiation of hollow LCF-specimens the postirradiation device was completed and mounted into the irradiation chamber. Fig. 41 shows this device with a H-GRIM-LCF-specimen which is mounted stress-free at the cross point of the proton beam and the alpha particle beam. Below (800°C) the radiation furnace which was provided to maintain a constant specimen temperature is usally not needed , because of the high heat deposition of the beam current. Test irradiations together with tiny thermocouples welded at different parts on the specimen surfaces have shown that the reaction of the He-gas cooling to beam intensity fluctuations occurs within tenths of seconds. Therefore, quick variations of beam currents (I_α = 3μA, Ip $\leq$ 10 μA) do not significantly affect the temperature stability . Moreover temperature cycling experiments are easily possible up to about 5°K/s by changing the nominal temperature value with a ramp generator. To level out inhomogeneous beam density profiles the specimen rotates with about 3 Hz. During irradiation of rotating specimens a thermooptical system is envisaged for temperature control. It is expected that an open technical problem of such a system which is related to the vacuum window and the emissivity of the specimens can be solved during spring 1988.

Furthermore, for the handling of activated specimens and irradiation devices a glove box was completed together with several other shielding equipments.

2. Tensile experiments on helium-implanted 1.4914

Tensile specimens of martensitic steel 1.4914 with a gauge size 7 x 2 x 0.2 mm^3 were homogeneously He-implanted after a heat treatment at 1075°C/30' + 750°C/2h. During the reporting period the He-implantations were expanded to lower temperatures (220°C). The implantation and tensile test conditions were shown in the previous semi-annual report.

The upper part of Fig. 42 shows the temperature behavior of the change in yield strength $\Delta R_{0.2}$ caused by He-implantation while the lower part represents some data of the He-bubble morphology from TEM-observations: the swelling $\Delta V/V$, the average bubble radius r_b and the average bubble distance l_b which is the result of the concentration N_b according to $l_b = N_b^{-1/3}$. Below an irradiation temperature of 400-450°C an increase of the yield strength up to 120 MPa is observed, while above this temperature softening ($\Delta R_{0.2} \leq$ 70 MPa) occurs. Hardening is caused by He-defect clusters which are stable up to about 400°C and by He-bubbles visible in TEM-observations at temperatures above 300°C. It should be noted that the displacement damage during these helium implantations is small (<0.2 dpa) and therefore cannot explain the hardening behavior. It can be shown that the transition from hardening to softening with increasing temperature is a superposition of different mechanisms: softening is mainly caused by annealing of He-defect clusters and at higher temperatures by irradiation induced recovery of dislocations within the martensitic laths. Above 400-450°C this recovery effect is dominant and obviously correlates with the beginning swelling reduction. However, additional He-implantations and systematic investigations of the microstructural changes are necessary to determine the temperature and dose dependence of the softening and hardening mechanisms more quantitatively.

Staff:
G. Bürkle
R. Lindau
A. Möslang
D. Preininger
G. Przykutta

Publication:

A. Möslang and D. Preininger, "Effect of Helium Implantation on the Mechanical Properties and the Microstructure of the Martensitic 12% Cr-steel 1.4914". ICFRM-3-Conference, 4-8 October 1987 Karlsruhe Journal of Nucl. Mat. 154-156 (1988).

MAT18 Development of Low Activation Ferritic-Martensitic Steels

First wall and blanket structures of fusion machines will be made radioactiva during operation by the high neutron fluxes, giving rise to problems of reprocessing or waste disposal. To reduce these problems, it is necessary to avoid the presence of certain alloying elements (or some isotopes there of) and to minimize impurity elements exhibiting unfavourable activation properties. A literature survey has shown that in recent years 9-12% ferritic/martensitic steels have been devised in which mainly Mo and Nb have been replaced by additions of W or enhanced levels of V or Mn. The results obtained show that for the modified materials the standard of commercial alloys, like 1.4914, ore HT9, has not been reached, especially with regard to an adequate balance of tensile and impact properties. Research efforts under way at KfK/JEN to improve this situation have been described in recent semi-annual reports (KfK-reports 4165 and 4339).

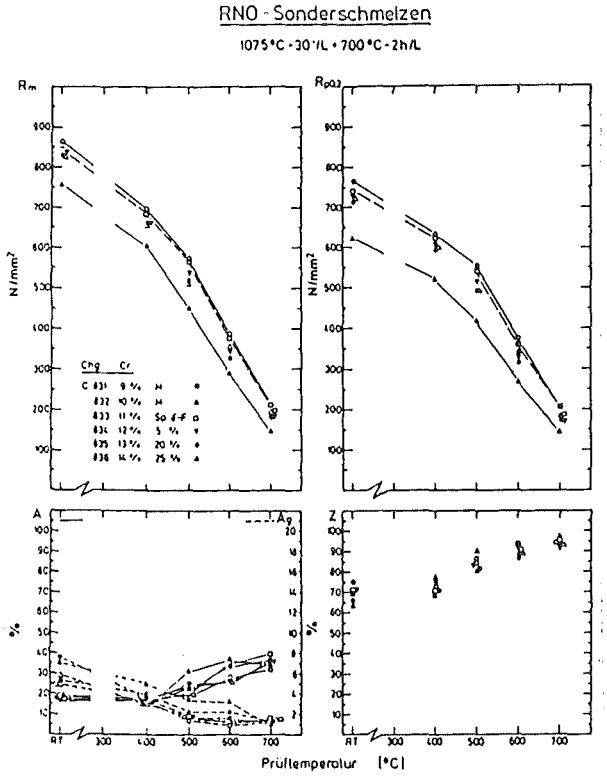

Fig.43: Effect of temperature and δ-ferrite content on tensile properties

a.) Investigation of the effect of Ce-, Ta-, Hf-additions:
Two melts No. 857 and 858 have been produced (Fa. Saarstahl, Völklingen) which are now available as forged, 25 mm square rods. These are Ce and Ta, and Ta and Hf bearing alloys, respectively. Metallographic studies have shown that both alloys have a finely grained structure (grain size 22-30μm) after quenching from a temperature range of 1000-1150°C. This means that the reference hardening temperature for steel DIN 1.4914, 1075°C, can also be used for the two experimental alloys. The annealing response between 200 and 900°C has been determined. There is a secondary hardening peak at 500±25°C; between 550 and 800°C hardness decreases appreciably as is well known for this type of alloys.

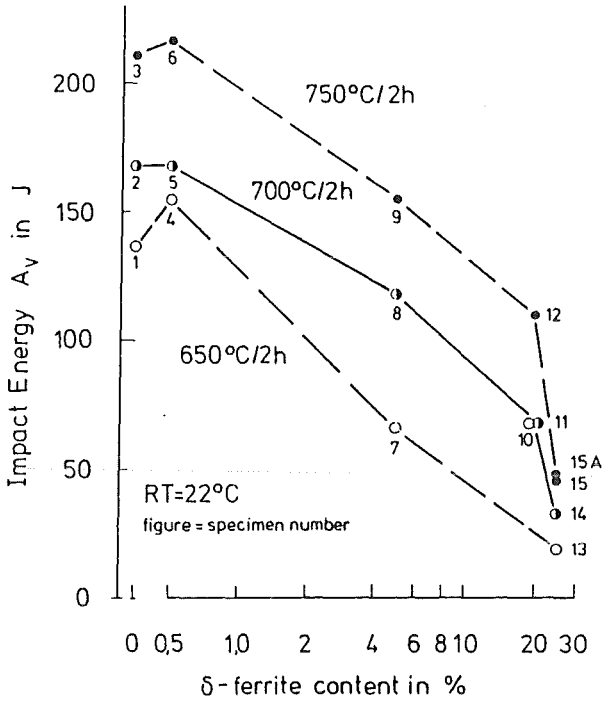

Fig.44: Effect of δ-ferrite content on the impact energy

b.) Variation of the δ-ferritic content:
A systematic study of the effect of the δ-ferritic phase on the mechanical properties of martensitic Cr-steels has been initiated. After quenching from 1075°C and different tempering treatments the tensile properties between RT and 700°C (Fig.43) as well as the impact properties at RT have been determined. The results of the instrumented impact tests are shown in Fig. 44. Above δ-ferritic contents of 0.5% the fracture energy decreases significantly. The load-deformation diagrams and SEM-investigations gave further information on the fracture process. Surprisingly, the softer δ-phase shows pure brittle fracture under impact loading and initiates quasi-cleavage fracture in the martensitic matrix. It appears that the fracture energy depends on the average spacing of the δ-ferritic particles in the microstructure,

Staff:
K. Anderko
W. Meyer
L. Schäfer
M. Schirra

N1 Design Study of Plasma Facing Components

First Wall Testing

A test program is planned at KfK for testing first wall (FW) sections in order to:

1. Provide an experimental basis to improve confidence in the prediction of thermal fatigue life by:

   (a) Validation of computational methods for
   - thermo-mechanical analysis
   - crack initiation by cycle plastic deformations
   - fatigue crack propagation

   in complicated geometries.

   (b) Life time determination including
   - observation during life
   - study of failure modes for prototypic FW sections under representative thermo-mechanical conditions.

2. Compare integral behavior of different FW concepts including protection.

   The test specimens will be fabricated with industrial methods and tested under mechanical boundary conditions and thermal loads as close as possible to those of NET; effects of neutron irradiation will be excluded.

   The design of a test apparatus raises different questions on the implementation of "representative thermo-mechanical boundary" conditions.

   Pre-calculations have been performed to some design issues:

   (I) size of FW segment

   (II) support conditions (mechanical boundary conditions)

   (III) simulation of volumetric heating (despite the lack of neutrons a representative temperature distribution can be achieved by selecting surface heat flux and coating of the metallic wall appropiately)

   (IV) acceleration of tests by higher heat fluxes and larger wall thicknesses and increased offburn times.

   Two three-dimensional FW models have been investigated. The geometry has been simplified keeping the major features of the FW-designs. The size has been varied up to 50 x 72 cm^2. In a first step these FW models have been considered as part of a blanket box and their integral behavior by imposing different constraints on the box has been studied. Based on these results further investigations have been performed on items (i), (ii), (iii) and (iv) above.

   The influence of support conditions is of great importance. They should result in a "representative" stress distribution which is to a large extent uniform in the direction of the coolant flow. Among five examined mechanical boundary conditions a support with solid side walls seems to be the most promising.

The FW test specimen will be positioned in a vacuum chamber, will be actively cooled and will be heated by thermal radiation in a cyclic manner. Crucial part of the test apparatus will be the high temperature and high heat flux of the heater. In order to transfer the necessary heat flux of between 50 and 100 W/cm^2 to the hot surface of the specimen protection tile a heater temperature of about 2200°C will be necessary. This would cause no problems when using a heater made of graphite or refractory metals. However the cyclic operating conditions with burn and off-burn times of only a few minutes corresponding the steep temperature gradients in the heater seem to make the time to failure of the heater unpredictable.

Therefore prior to design and construction of the FW test apparatus heater pre-tests with different heater materials including CFC were initiated. The pre-test divice is under construction and heater specimens have been ordered.

Staff:
E. Diegele
E. Eggert
G. Hofmann
K. Rust
G. Schweinfurther

Divertor Design

The main thermomechanical issues for the NET divertor are the high heat flux, the physical and chemical sputtering rates, and the surface erosion from plasma disruptions. Most of the divertor walls proposed so far consist of a metallic heat sink structure protected by a heat and erosion resistant surface material. In this duplex structure material compatibility, perfect bonding, temperature limits, and cycling shear stresses due to differential thermal expansion are the major concerns.

A two year testing program has been launched to examine the thermomechanical behavior of candidate material combinations and attachment procedures under operating temperature and stress cycles. In a first step a preselection will be made on the basis of thermal shock tests with simple samples (no active cooling) showing their vulnerability to ratcheting effects at relevant heat flux levels. In a second step the most promising configurations will undergo cycle tests with actively cooled samples. For this test program a contract and a list of proposed test materials have been negotiated with the NET team.

The tests will be done in an existing plasma spray device, which needs to be up-graded. This involves a cooling circuit, which has been installed. The circuit is operated with demineralized water at a maximum pressure of 16 bar and a variable flow rate up to 2 l/s. The second major equipment is a rotating sample holder, for which the conceptual design has been prepared. The instrumention and computerized process control have been initiated.

A series of pretests with dummy samples and precalculations is in progress to demonstrate that relevant temperature and stress amplitudes can be simulated in the thermal cycle tests with the envisaged non-cooled flat disc samples. From these investigations a preliminary set of test parameters has been established. Sample procurement is being prepared by the NET team.

Staff:
G. Class
K. Kleefeldt
K. Schramm
E. Stratmanns
E. Wolf

N2 Shield Design Studies

The design studies for the movable shield segment for NET were continued. Comparison of a water-cooled version with poloidally running tubes, a water-cooled box version, and a helium-cooled concept with helium pressure tubes inside large steel blocks revealed: The concept with poloidally running tubes is technically the simplest but does not have enough shielding effectiveness, the water-cooled box concept (see last progress report KfK 4339) is slightly more expensive but has good shielding properties. The most expensive, most complicated, and heaviest version is the one with helium cooling.

Three versions of the water-cooled box concept have been studied: one with an integrated first wall, one with a separate first wall box, and one with beryllium blocks in the front part. The latter is of interest for tritium breeding with a lithium salt solution. Breeding is much improved when a gap filled by the salt solution is left between beryllium and steel structure (see Fig. 45)

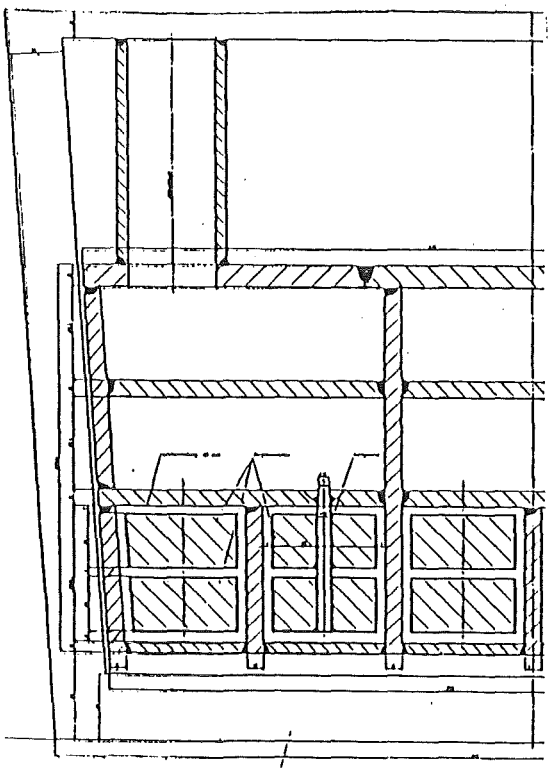

Fig. 45 Water cooled box concept with beryllium blocks in the front part

On the inboard side only a concept with an integrated first wall will give enough shielding effectiveness for the extended plasma version of NET. It is illustrated on Fig. 46

Temperature and stress distributions in the first wall with poloidally running water coolant tubes and radiatively cooled graphite tiles were calculated. A heat load of 40 W/cm^2 was assumed. The 8 mm first wall is cooled from both sides. Fig. 47 shows the temperature distribution. The maximum tile temperature is about 1800°C. A surface coating is assumed which leads to an emissivity variation between 0.9 in the region where the wall is in contact with the graphite tiles and 0.3 else. The stresses remain well within the limits.

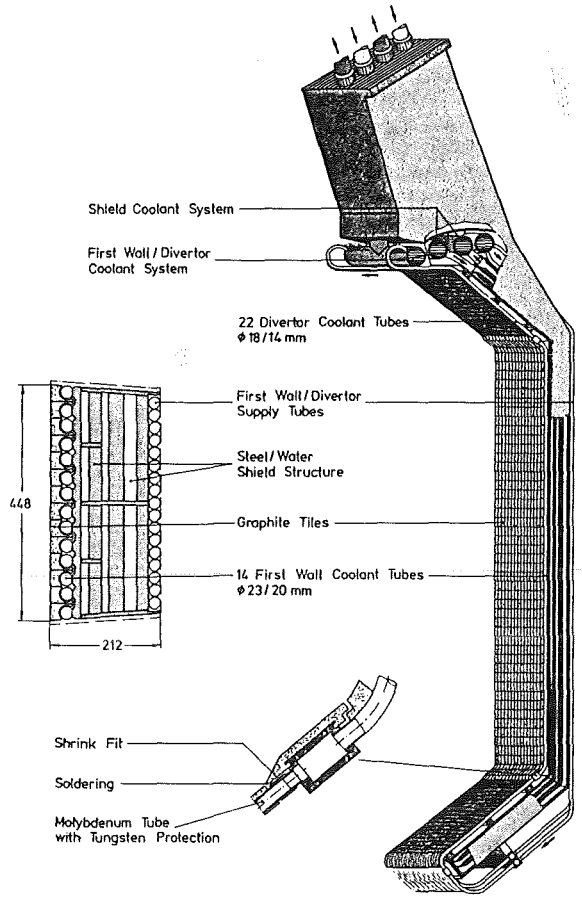

Fig. 46 Water cooled inboard blanket with integrated first wall, extended plasma version of NET.

The stress analysis will be extended to a larger part of the surface.

Except for the first wall studies the work on the NET shield module will be discontinued and documented, due to the reorganisation of tasks between NET and the European research associations.

Staff
E.Bojarsky
U.Fischer
G.Reimann
H.Reiser

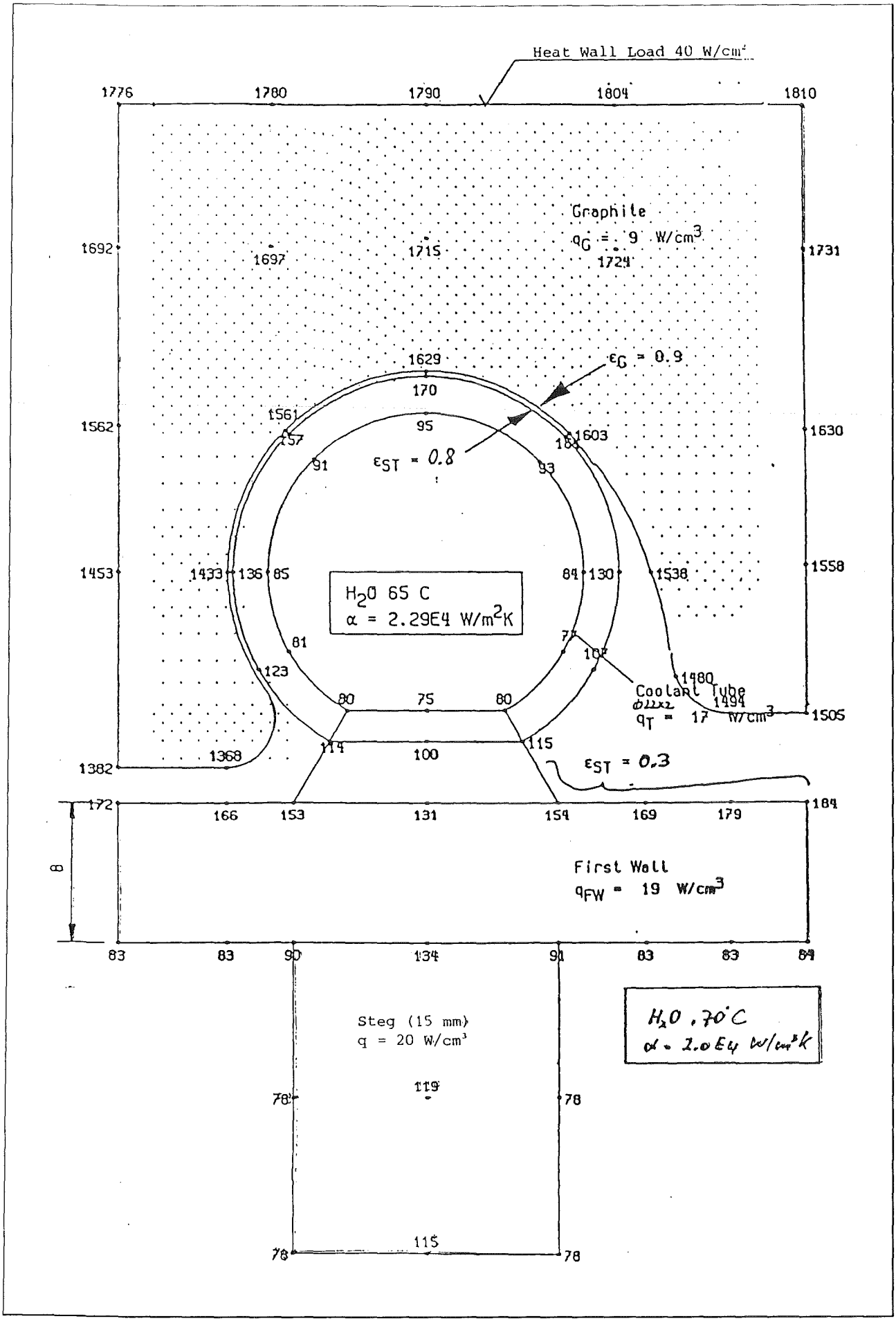

Fig. 47 Temperature distribution, first wall

N3 Development of Procedures and Tools for Structural Design Evaluation

Objective of the work is to accumulate knowledge on computational tools to get more and more reliable lifetime predictions for high heat flux components.

During the previous period developments work was dedicated to

- inelastic stress analysis
- crack growth analysis
- lifetime predictions considering fatigue crack growth

Inelastic stress analysis.

Performing low cycle fatigue (LCF) tests on samples with different geometries such as hollow cylinder specimen, GRIM specimens and GRIMH specimens, problems raise in comparing the experiments. Results are given as global measurements of the total force on the specimens versus the total elongation. However, lifetime predicting models make use of local stress-strain relations. The distinction between global and local variables is of great importance if the plastic deformation is restricted to a zone which is small compared to the length where the total elongation is measured. The transfer of results is clear for cylindrical samples but difficult if the specimens have geometrical non-linearities as there are varying wall thickness or varying curvature.

Investigations have been performed to correlate total elongation and local strains on difficult types of specimens. The calculations are so far restricted to a homogeneous temperature distribution on the specimens.

Improvement in crack growth analysis.

The weight function method for calculating stress intensity factors in first-wall components has been extended to compute the maximum crack opening and the resulting leak area for cracks which have totally penetrated the wall. A final crack can be described as a straight through crack. Corresponding crack opening and crack area values are available only for simple stress distributions.

Expressing the crack opening displacement of a mechanically loaded straight through crack by a power series representation, the maximum displacement and the leak area can be calculated by using the coefficients of these series for an arbitrary loading.

Lifetime Prediction by Fatigue Crack Growth

Fatigue crack growth data are determined in uniaxial mechanical tensile or bending tests. Stresses in high heat flux components are mainly caused by thermal loads and therefore are of multiaxial nature. To investigate the effect of the multiaxial stresses, crack propagation on a plate under thermoshock loading has been considered. Stress distributions have been calculated thermo-elastically and inelastically using a simple elastic-plastic model with kinematic hardening and using a more sophisticated material model (ORNL). In each case the stress distribution has been used to calculate the crack growth of an initially given crack and to compare the computed crack dimension with the size and shape of the crack which is found experimentally

Staff:
E. Diegele
T. Fett
D. Munz

N5 Development of Theory and Tools for Evaluation of Magnetic Field Effects on Liquid Breeder Blankets

In a blanket of a fusion reactor the heat deposition is concentrated near the first wall. If laminar slug flow of the liquid-metal is assumed, prevailing in the high magnetic field of NET, this kind of heat deposition distribution gives rise to a steep temperature gradient in the flow duct. This results in high temperatures of the liquid metal near the first wall so that the mean temperature rise has to be kept low to avoid increased corrosion attack. Decreasing the mean temperature rise means increasing the flow of the liquid metal resulting in increased pressure drop. As shown in [1] the overall heat transfer can be improved by "MHD Flow Control" without increasing the mean flow through.

A particular type of MHD flow control, named flow tailoring, achieves desirable non-uniform velocity profiles within a single duct by proper variation of flow tailoring, in which the dimension of a rectangular duct in the direction of the magnetic field changes linearly along the duct axis, is particularly appropriate as a first-wall coolant channel design. In such a design, the first wall is made of a series of adjacent poloidal ducts with expansions, contractions and uniform cross section segments. This arrangement guides the flow towards the first wall. The velocity adjacent to the first wall changes in the downstream direction but it remains always higher than the average velocity, thus improving heat transfer. Further heat transfer enhancement is possible due to the non-zero transverse velocity component.

The potential benefits of this configuration and its immediate applicability to blanket design have made it the best choice as the first joint ANL/KfK test on liquid-metal MHD. Testing has started in November, 1987, at ANL's ALEX facility with a test section fabricated at KfK.

The test section incorporates 37 pressure taps, 7 flanges for traversing probes, and 158 electrodes for obtaining detailed mappings of the pressure, velocity and voltage distributions throughout the flow field. Unique features of the test section include one explosively bonded, laminated copper/SS wall to simulate the thick second wall, and an electrically insulated strongback to relieve the remaining three thin test section walls from the pressure loads.

The design of the test section and the MHD-analysis carried out by a 3-D-computer code will be presented at the International Symposion on Fusion Nuclear Technology, Tokyo, April 10-15, 1988 [2]. The used computer code is an extension of the codes already developed by ANL and the University of Indiana for treating 3-D MHD effects in round and square ducts [3].

The first results of the voltage distribution measurements agree well with the 3-D computer calculations.

In order to get a deeper insight into the physics of MHD flow theoretical work is also done at KfK in which the governing MHD-equations are solved numerically by a finite difference method.

In mid-1987, work on a 2-D-code solving the equations for MHD flows in an infinitely long, rectangular channel was finished. With that program we were able to obtain results for flows with Hartmann-Numbers (Ha) up to 10^3. Parameters varried were Hartmann-Number, wall conductivity and angle between the magnetic field and the duct. In the meantime we developed a 3-D-code for calculating MHD-flows in rectangular ducts. The magnetic field and/or the wall conductivity change in axial direction, thus introducing 3-D-effects. Testing of this code is just underway and first results have been obtained. As an example the figure shows the structure of the flow in a non-conducting duct at Ha = 70, $N = 10^3$ (interaction parameter) at three different locations in the entrance region of a magnetic field.

Development of a Velocity Meter

To investigate MHD-flow distribution of liquid metal a velocity meter is being developed at KfK using the propagation time of artificially induced temperature pulses as process variables. The schematic set-up of the measuring device is shown below.

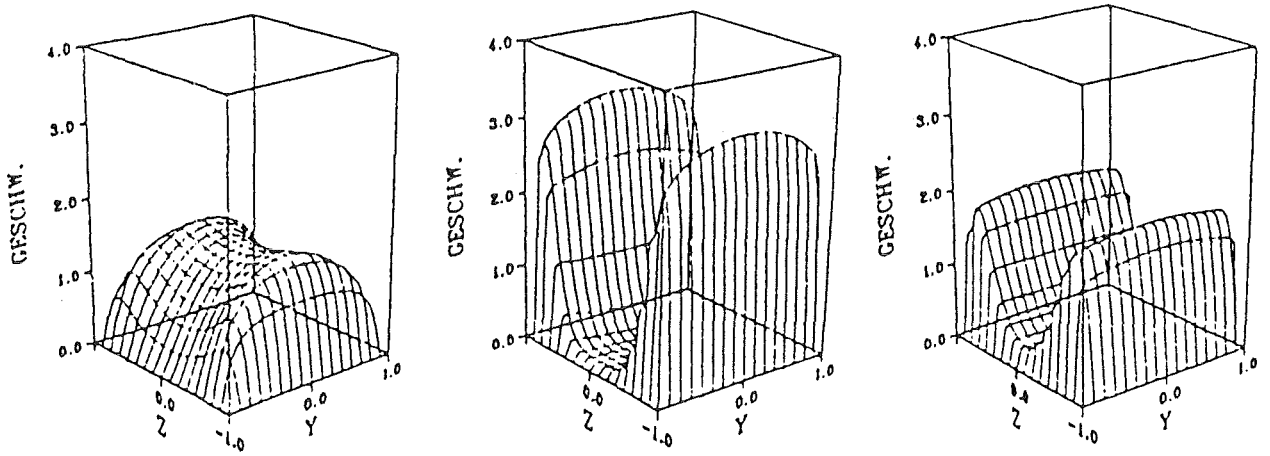

Fig. 48: Flow structure in a nonconducting duct in the entrance region of a magnetic field.

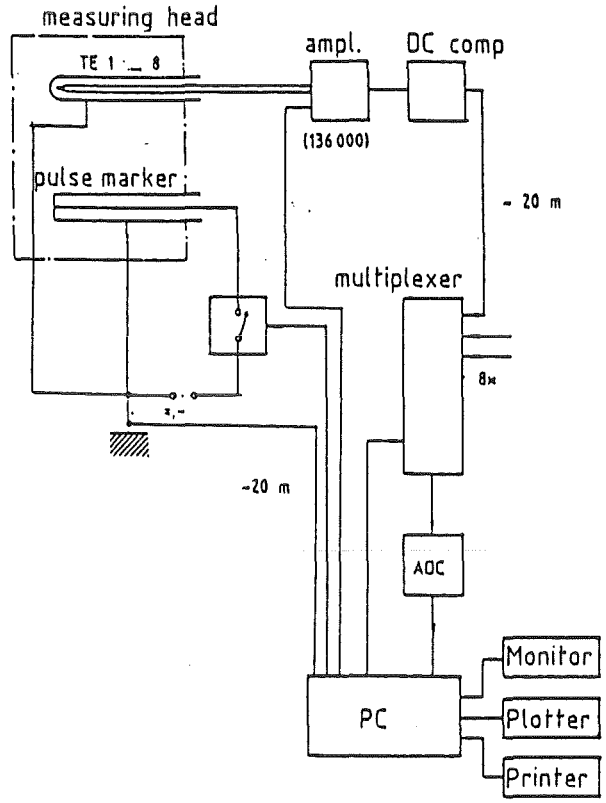

Fig. 49: Schematic set-up of measuring system

It consists of the measuring head (with pulse marker to create temperature pulses, sensors to detect them), a heating system operated by a PC, amplifiers for signal amplification, and a PC for process operation and data evaluation. Within the period to be reported testing has been completed. The stage of development of amplifier and data transmission is shown in the figure below.

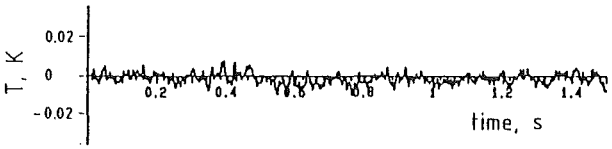

Fig. 50: Overall noise of data acquisiton system

It shows the total noise of the system including thermocouples installed in a sodium rig (used as signal detectors), amplifiers (amplification 136 000), and signal transmission lines of more than 20 m to a PC. It can be seen, that the total noise of the system is less than ±0.01 K. The constant temperature level of the test rig was 670 K. With this high performance of the data acquisition system, developed for this application, temperature signals with an amplitude of only 1/10 K can be easily evaluated. Consequently velocities evaluated from time-temperature-signals are of high accuracy. For data evaluation three modes have been developed:

- Evaluation by detection of propagation time of signal maxima.
- Fitting of theoretical equation to the measured signals.
- Cross correlation between signals obtained from 2 sensors in different positions.

The three modes of evaluation have different capabilities. The first mode can be applied over a large range of velocities; but it requires data sampling of a large number of signals (10) to obtain precise results. The second mode computes velocities with very low scatterings; its range of application is the region of low velocities (<0.2 m/s). The third mode delivers results with very low scattering, even when cross correlation is carried out between two individual signals. The range of application of this mode are higher velocities (>0.2 m/s). A result of measurements in sodium is shown in the next figure.It presents measured velocities as a function of

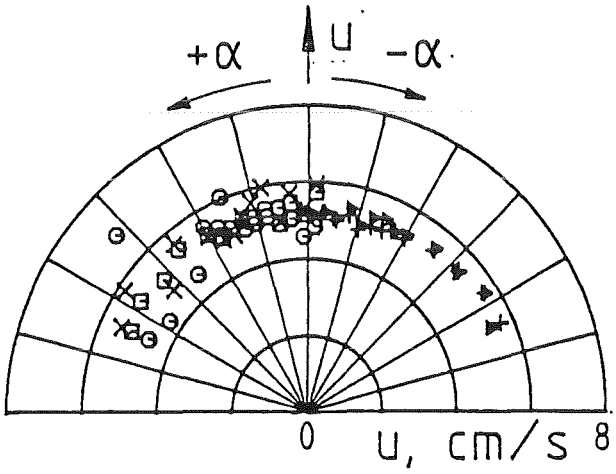

Fig. 51: Measured velocity as a function of flow direction α in sodium

flow direction α; α equals zero when the fluid is flowing from the pulse marker to the sensors placed at defined distances from it. The results at positive value of α are computed from signal maxima, the results at negative values of α are measured with the same sensors as the positive results but computed by fitting of theoretical equation. They are only plotted at negative values to make the diagram more clear. One can state: The results obtained are independent of flow direction α. This corresponds to theoretical considerations. Additionally it can be seen that both modes of evaluation achieve the same results; but results computed with the first mode (detection of signal maxima) scatter more than those obtained by fitting of the theoretical equation.

The stage of development obtained allows the application in experiments.

Staff:

G. Arnold
Dr. L. Barleon
DI. V. Casal
R. Kirchner
H. Kreuzinger
H. Kußmaul
K.J. Mack
DI. H. Miller
DP. A. Sterl
K. Thomauske

References:

[1] Nuclear Fusion Project, Semi-Annual Report of the Association KfK/EURATOM, April 1986-September 1986, KfK 4165/EUR 10534 e.

[2] T.Q. Hua, B.F. Picologlou, C.B. Reed, J. S. Walker, L. Barleon, H. Kreuzinger: MHD Flow Tailoring in First Wall Coolant Channels of Self-Cooled Blankets; submitted for presentation at the Intern. Symp. on Fusion Nuclear Technology, Tokyo, Japan, April 10-15, 1988.

[3] T.Q. Hua, J.S. Walker, B.F. Picologlou, and C.B. Reed: Three Dimensional MHD Flows in Reactangular Ducts of Liquid-Metal-Cooled Blankets, to be published in Fusion Technology.

N6 Studies of Pebble Beds of Ceramic Compounds

The results of the studies of pebble beds are included in the report on B1 Blanket Design Studies chapter Helium-Cooled Ceramic Breeder Blanket.

RM1 Background Studies on Remote Maintenance

The objective of this task is the development of the remote connecting technique for NET. During the period under review the work was concentrated on the investigation of pipe connectors for water cooling, liquid metal breeder fuelling, gas cooling and gas purging systems, and remote cutting and welding techniques.

Remotely operated pipe connectors

KfK has started pre-tests with selected pipe connectors. The selection has been made in accordance with the results of the Study "Pipe and Vacuum Duct Connections for NET". The KfK-type connectors have been provided in the frame of the KfK R&D program.

Three JET-type connectors have been provided from JET. .At KfK there are several test facilities available for basic tests of pipe connectors.

The remote handling capability of the connectors has been checked in the test facility TINA (Fig. 52).

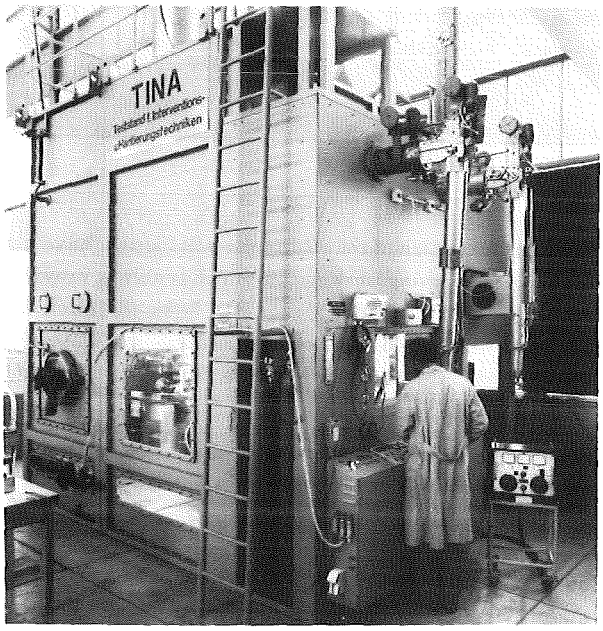

Fig. 52: Test facility TINA

TINA represents a Mock-Up of a hot-cell facility and can be operated under a slight underpressure. The remote handling capability of the different pipe jumper configurations can be demonstrated in the test rig JUTTA. Tightness tests have been performed in the test facility PAULA.

The corrosion tests in the test rig FLATEST have been started with a soft-iron material used as a gasket in between bolted flanges rated to liquid Pb-17Li. First test results will be available by mid 1988.

To get NET related results integral remote handling tests with selected prototypes have to be performed under NET typical geometrical conditions and, if possible, with NET related handling tools. The test facility (Fig. 53) will simulate the upper part of a prototype blanket segment including its auxiliary coolant make-up and supply systems. The multi- purpose facility will provide possibilities to implement all the different designs of blankets under investigation for NET. The performance of lip connections for blanket segments will be tested using the lip welding units currently being developed at KfK.

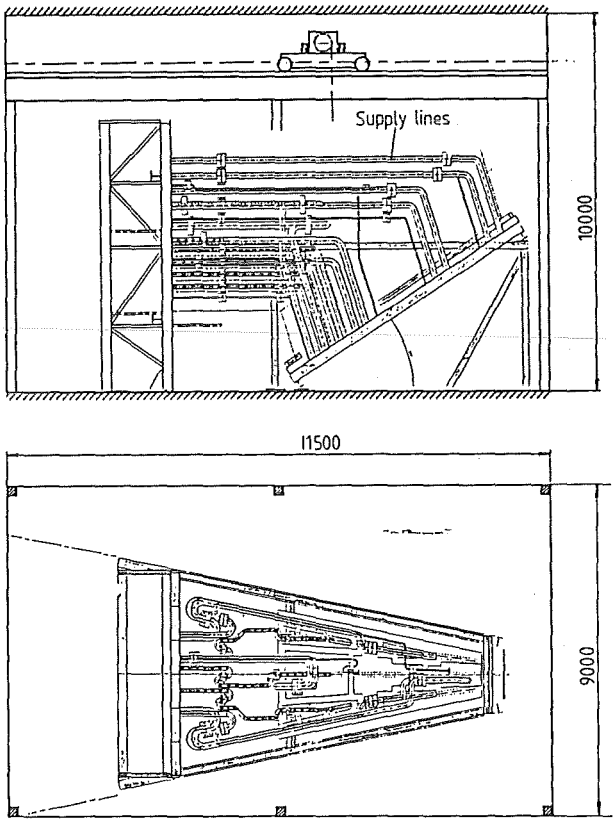

Fig. 53: Test facility BERT for integral test of NET relevant connection technique

The remote handling work will be carried out with a remotely operated overhead bridge crane and an electrical impact wrench attached to the crane hook. The crane hook will be turnable, movement will be radio controlled. TV systems will be provided.

The design of the general arrangement, the layout of the crane, the configuration of the pipe jumpers and the segmentation of the blanket module have been finished.

The order for the detailed design of the crane and the fabrication has been placed to an industrial company. Remote handling operation will be started end 1988.

Development of a remotely operated welding system

Welding will be used as an alternative solution to replace potentially leaky mechanical connectors and for all the connections where mechanical connectors cannot be used.

These areas will be found where large openings have to be closed or large pipe ends or vacuum ducts have to be connected and also inside the vacuum vessel.

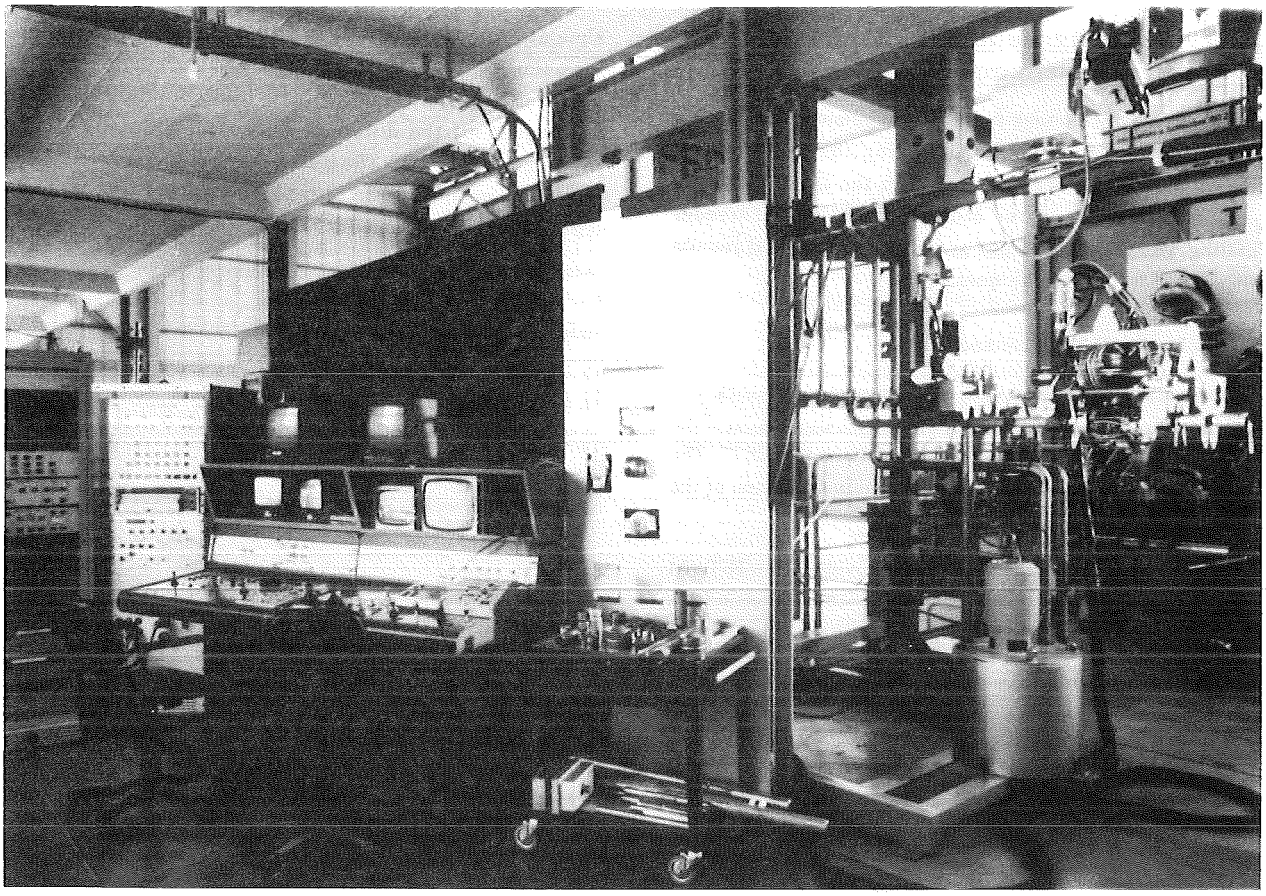

Fig. 54: Test facility for remotely operated welding units

In some extreme cases a combination of mechanical connectors and welded sealing seems to be the only solution to meet the requirements.

As the commercially available welding units do not meet the requirements for high quality under realistic operation conditions of a fusion reactor, KfK started work on a welding/cutting system adaptable to the physical and environmental characteristics of a fusion reactor.

Fig. 54 shows the test facility for remotely operated welding and cutting units as it was at the end of 1987.

Up to now KfK has fabricated and tested a pipe welding unit

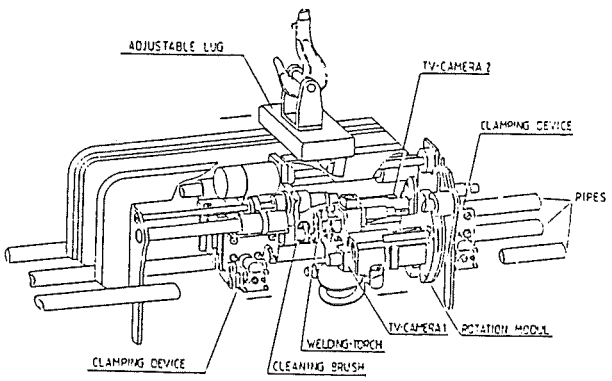

Fig. 55: Remotely operated pipe welding unit

(Fig. 55) for pipe diameters from 30 to 60 mm/OD aswell as the pipe cutting and pipe end preparation. Techniques for the inert gas protection of the root of the weld seam have also been tested. A roving work station which is able to provide a mobile power and signal source has been installed and equipped with cabling and connectors. This station can be transported to the work site so that a number of work units can be supplied.

A new multi-station welding control room has been designed and partly erected. This unit is intended to be used to demonstrate that one welding operator can control more than one welding or cutting operation simultaneously. Presumably such a system will be necessary for planned dismounting and remounting of components to be replaced with a certain regularity. Fig. 56 is an artist picture of the proposed welding system.

The test rig for simultanous operation of different test units will be completed by the end of 1988. For most of the computer control and the remote handling equipment fabrication orders have been placed.

The detailed design of the prototype lip welding unit has been completed. The fabrication of the subcomponents has been started.

The design of pipe welding/cutting units for a pipe diameter range from 100 to 200 mm OD has been started.

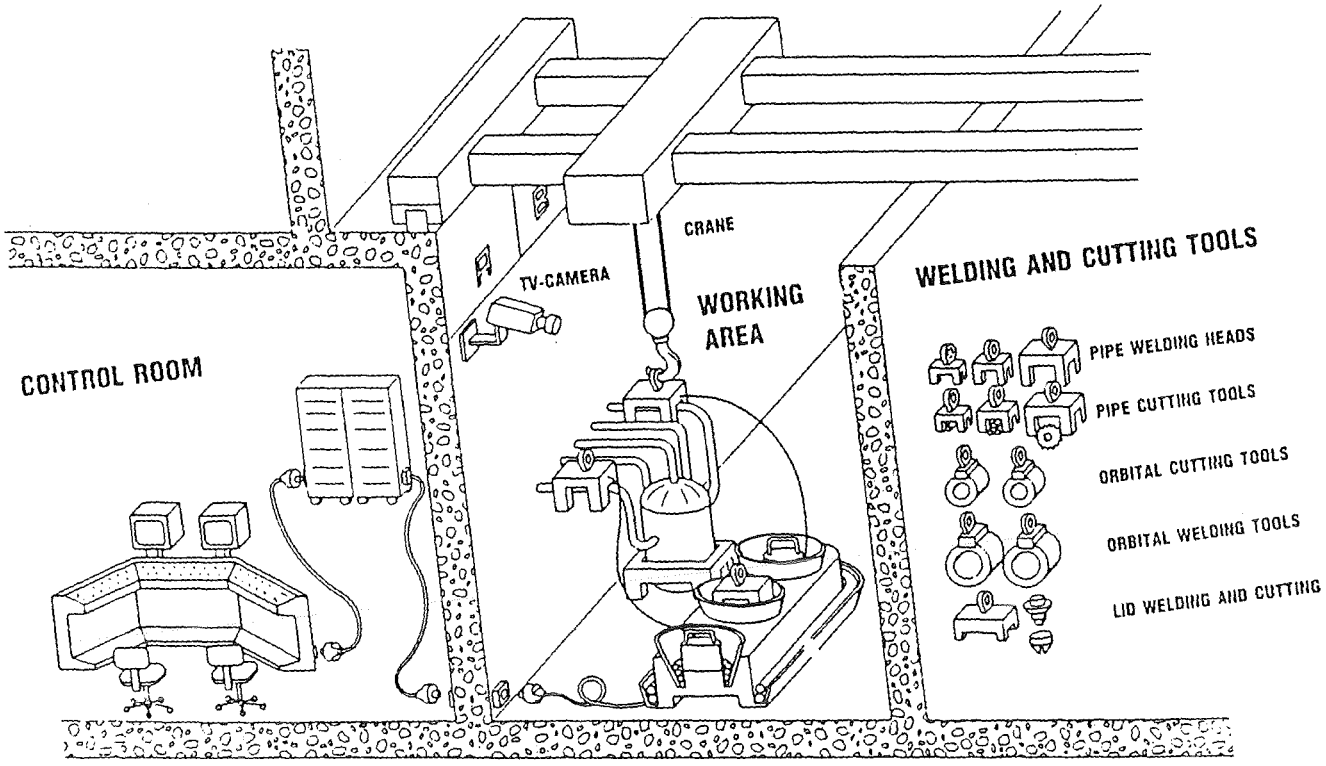

Fig. 56: Remotely operated cutting and welding system

Staff:
L. Gumb
U. Kirchenbauer
A. Schäf
M. Selig
M. Trettin
R. Ullrich

RM2 Mechanical Component Assembly

In order to provide designers and contractors with information KfK cooperates with the NET team in the preparation of a Remote Handling Manual (RHM). It contains a set of General Rules and Design Standards, adapted by NET for components and units of the NET device which require remote handling, and sets guidelines for handling equipment design.

Within the frame of the RM2 contract the work was continued with:

- the review of available fasteners and the definition of a programme to specify and test fasteners in order to settle design standards. An intermediate report will be finished at the end of March 88.
- the definition and specification of attachment devices for the transfer and transport of components.

With the progress of machine design the investigation and standardization of components and the development of remote handling equipment the Remote Handling Manual will be completed according to the time schedule of NET with the beginning of the Detailed Design Phase in 1990.

Staff:
B. Haferkampf
A. Suppan

RM3 Handling Equipment for In-Vessel Components

The investigation of an In-Vessel Handling Unit (IVHU) for inspection, repair and replacement of NET in-vessel components was continued. CEA, CEN/SCK, ENEA, JET, SPAR and KfK cooperate in the development of such equipment. It consists of

- a contained transfer unit (CTU)
- a transport unit based on an articulated boom or an in-vessel vehicle movable on telescopically inserted rails
- various work units with end-effectors attachable to the transporter
- the control system

Out of the 9 sub-items of the RM3 technology programme the following tasks were carried out.

SUB-TASKS 1 and 3: Development of a Conceptual Design and Boom Position Monitoring

In agreement with the NET team the KfK activities were mainly based on the investigation of an articulated boom and the required auxiliary equipment. The study is documented in a final report [1,2] and resulted in the proposal of a reference concept for an in-vessel handling system.

General Architecture

The in-vessel handling system is shown in Fig. 57. It consists of two in-vessel handling units (IVHUs) arranged at opposite sides of the vacuum vessel and of a transport carrier located at one of two additional entry ports. The transport carrier assists the IVHUs by transferring components and equipment to and from the torus. During operating the NET device the entry ports are gastight closed by plugs. They will be handled by means of special plug handling devices. In order to avoid the contamination of the reactor hall the handling equipment is housed in CTUs which are permanently attached to the vacuum vessel. Transport flasks are foreseen to transfer components between the CTUs and storage and service areas, respectively.

In-Vessel Handling Unit

The IVHU is composed of a transport unit (TU) and three different work units remotely attachable to the TU. These are a manipulator unit as a multi-purpose unit and two special work units for the exchange of radiofrequency antennae and divertor plates, respectively.

The TU shown in Fig. 58 consists of the carrier, the trolley moved by means of a motor driven planetary roller spindle and the articulated boom with a total length of approximately 25 m. The 11 links of the boom have box cross sections and are linked by yaw joints. Their axes are split. They are equipped with self-aligning roller bearings and are actuated by planetary roller spindle units arranged at the upper side of the link boxes while the supply lines are routed inside the links. Two drive units in series are actuating one link. Boom and trolley are linked by a combined yaw and roll joint to

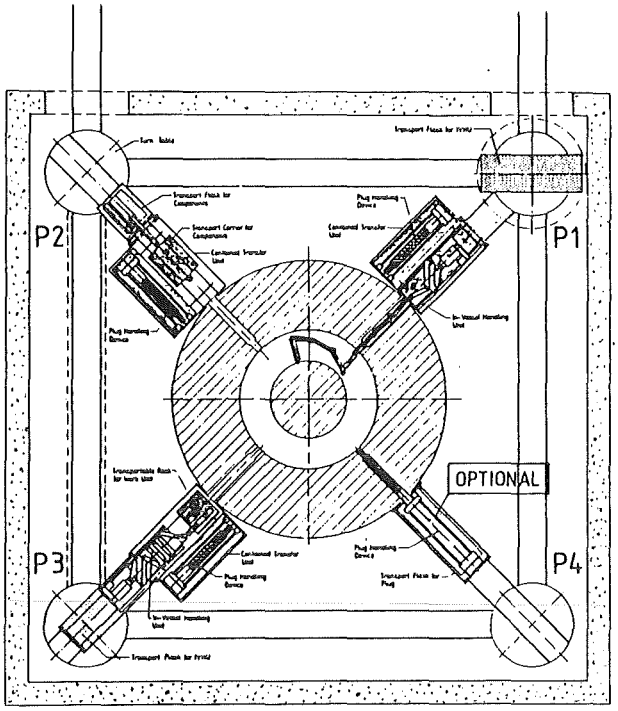

Fig. 57: IHVU-Overview

compensate the angular deflection. The tip of the boom is designed as an end-frame to attach the work units. To compensate the boom deflection the frame is linked by a combination of pitch and roll joint. Vertical displacement will be equalized by telescopic masts integrated in the work units.

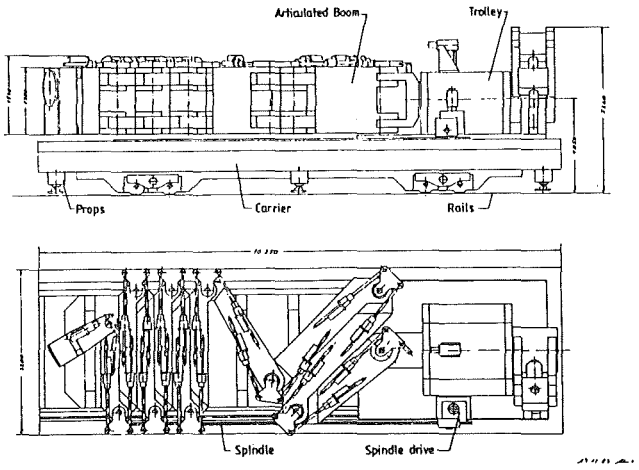

Fig. 58: TU-Scheme

Structural Analysis

Stresses and deformations of the NET boom were analysed for the initial mechanical design version in various kinematic configurations. Some excessive values were noted in certain places which could be reduced to allowable limits by appropriate design changes: Increase of the boom cross-section, design details near the joints in order to smoothen the stress profile, modifications of the joint design. Some alternative designs (e.g. a frame construction) were investigated. As a result of these analyses the boom design was modified and now satisfies the structural requirements.

Work Units

The electrical master-slave manipulator unit (Fig.59) consists of a pair of manipulator arms and two cameras. The maximum load capacity is 50 kg. It has 7 motions with force reflexion. The slave arms and one camera are mounted at a common crossbar which is attachable to the telescopic mast. The unit is rotatable by ±180°.

The divertor handling unit (Fig.60) combines one large gripper to handle the divertor plates, one manipulator to support replacement operations and two cameras. The load capacity of the large gripper is 1000 kg, of the manipulator 100 kg maximum. Together with the telescopic mast they are rotatable by ±180°.

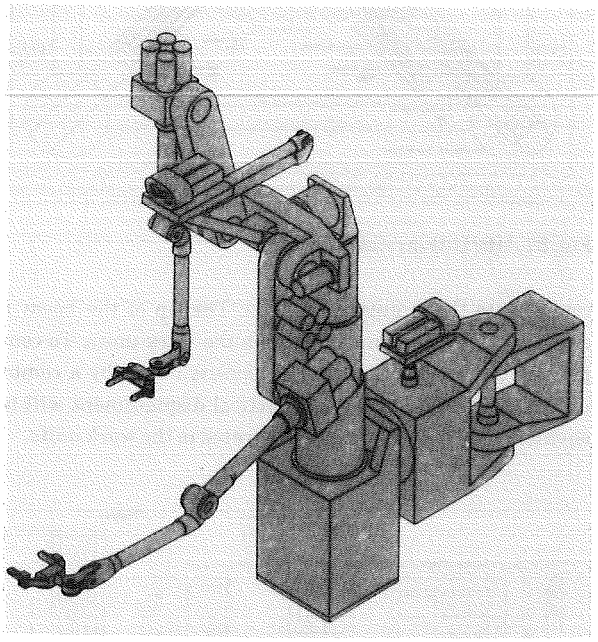

Fig. 59: Manipulator Unit

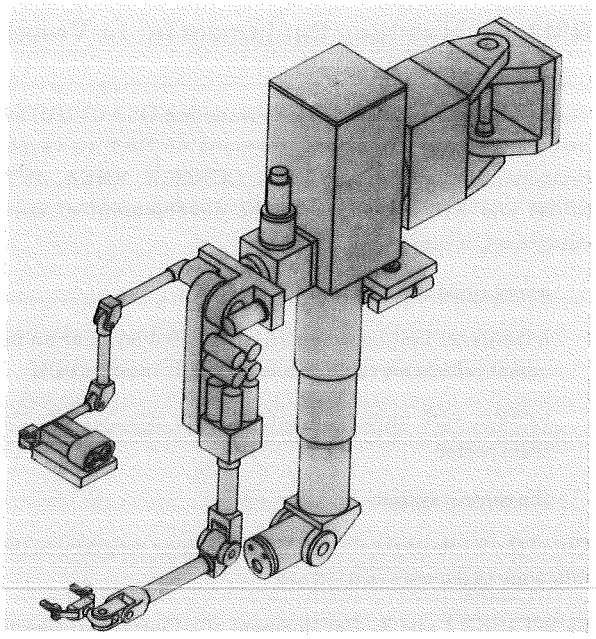

Fig. 60: Divertor Handling Unit

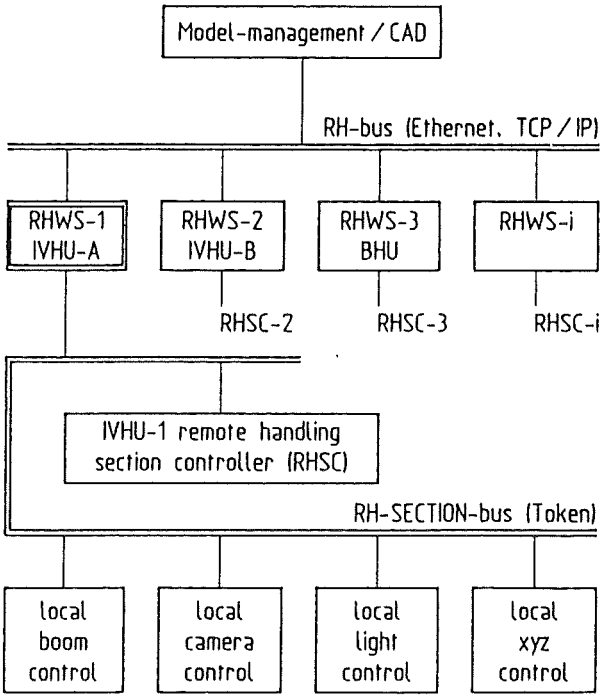

Fig. 61: Overall control system architecture

Control System Specification

The concept study report for the control of the NET in-vessel handling unit was finished [3].

The proposed control system for the in-vessel handling unit is CAD-model based. The simulator model is updated on-line by joint sensor and assembly sensor signals, such that a synthetic scene presentation is available. As main functional modules of the control system the following were indentified: task oriented handling support, teach-in and repeat, integrated control for viewing and lighting, integrated (device independant) input handling, simulation, collision control, position correction, special kinematical, and geometrical handling support, system state management and logging, computer support for the control panel, back-up control. For collision and positioning control loops ultrasonic distance sensors and inclinometers are envisaged. The whole NET control system is partitioned into so-called remote handling sections mainly dedicated to one manipulator. The remote handling sections communicate via a remote handling bus. For in-section communication each section has a section bus. For the task control (supervisory) level of each section a high performance graphic workstation eventually supported by a general purpose workstation is necessary. The motion/path control level will be equipped with a general purpose process computer, which coordinates the local equipment controllers on the drive control level.

Graphics Interface

The implementation of the graphics enhancement to the JET boom control system [4, 5] was successfully finished and documented. The final stage of the synthetic scene presentation is shown in Figure 63. The conceptual design phase for

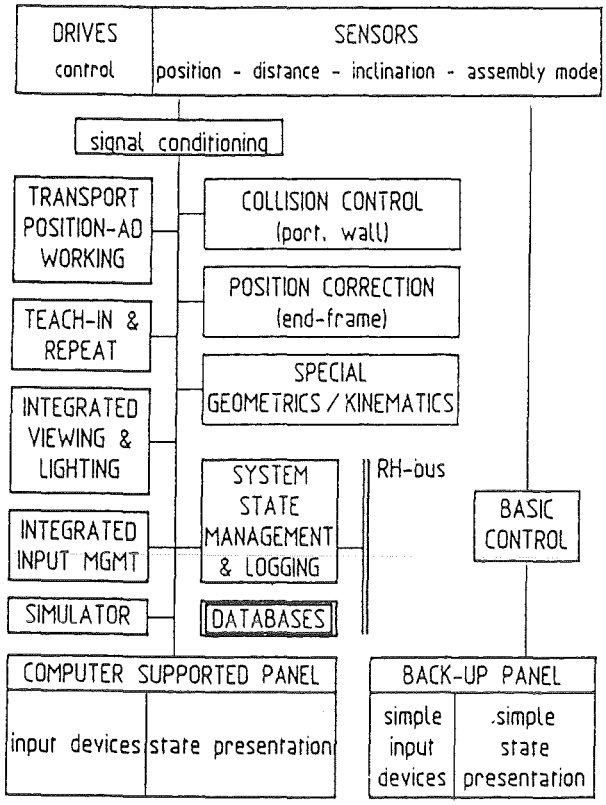

Fig. 62: Functional building blocks of a control section

the JET ex-vessel handling support by graphical simulation was started. Because of the large amount of model data, model generation will be done on the JET CAD-system, for which a post-processor has to be built allowing model transfer to the real-time simulator.

In the CATROB test environment we investigated special aspects of the NET control system: integrated viewing, man-machine cooperation in performing semi-automatic remote work, off-line programming, teaching and program downloading, man-machine interface layout (Figure 64).

With the ROBOT software, running on the Applicon CAD-system kinematic design studies for the KfK-NET boom design were done to control the reach volume of the boom. The threedimensional model of the boom used for this investigation is shown in Figure 65. Models with this degree of detail are envisaged for the NET boom control system. For space occupation studies the torus hall including the remote handling equipment was modelled, too, showing the narrowness of the remote handling space.

The kinematic design studies of the boom will be completed by investigation of the boom dynamics. The appropriate simulation software (MECHANISM-ADAMS) running as a subsystem of APPLICON-BRAVO was installed. First test runs with three links of the JET-boom with gear elasticity controlled by PD-controller were successful.

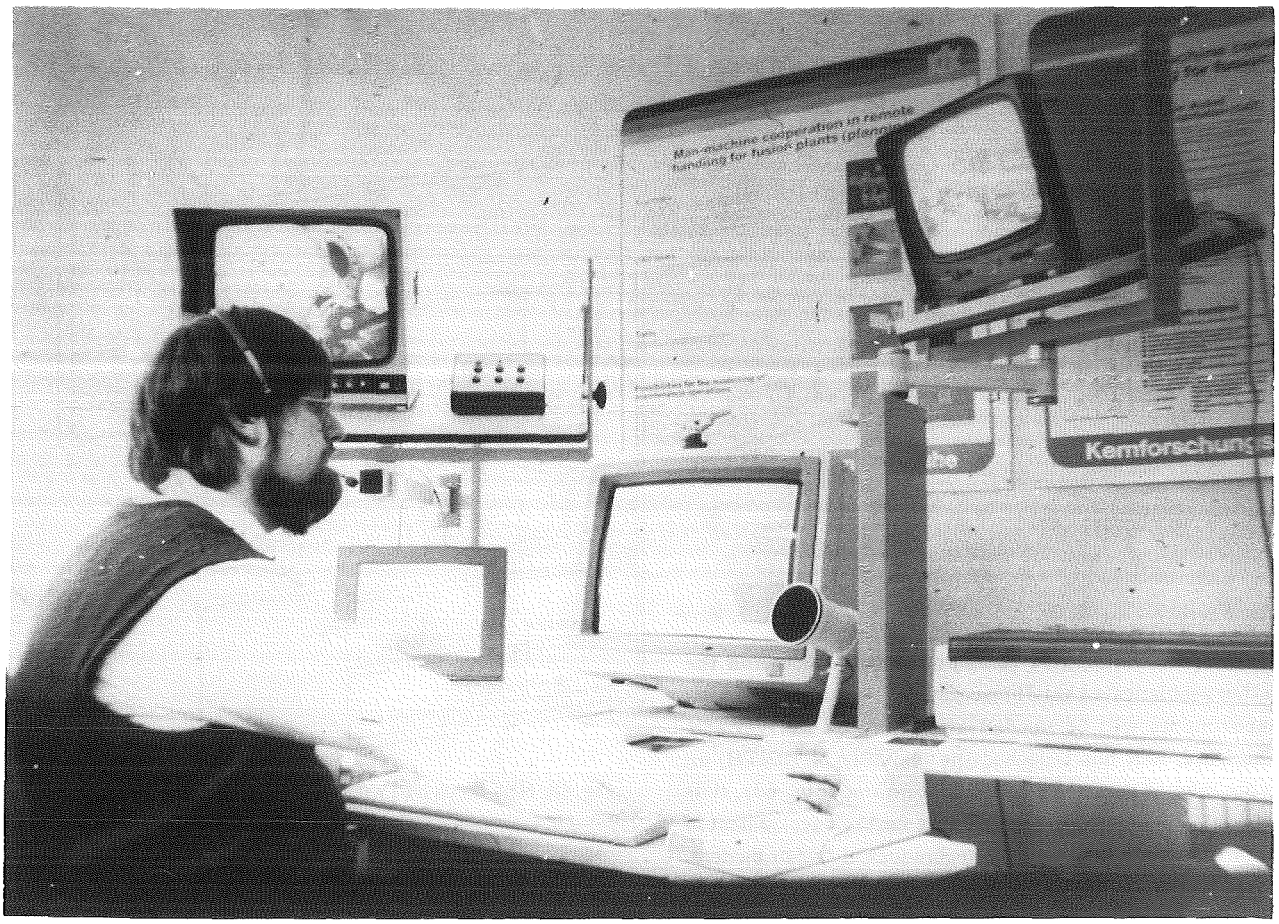

Fig. 63: Experimental man-machine interface set-up: graphics, TV (graphics controlled camera) touch screen, sensor ball, mouse, loudspeaker, microphone

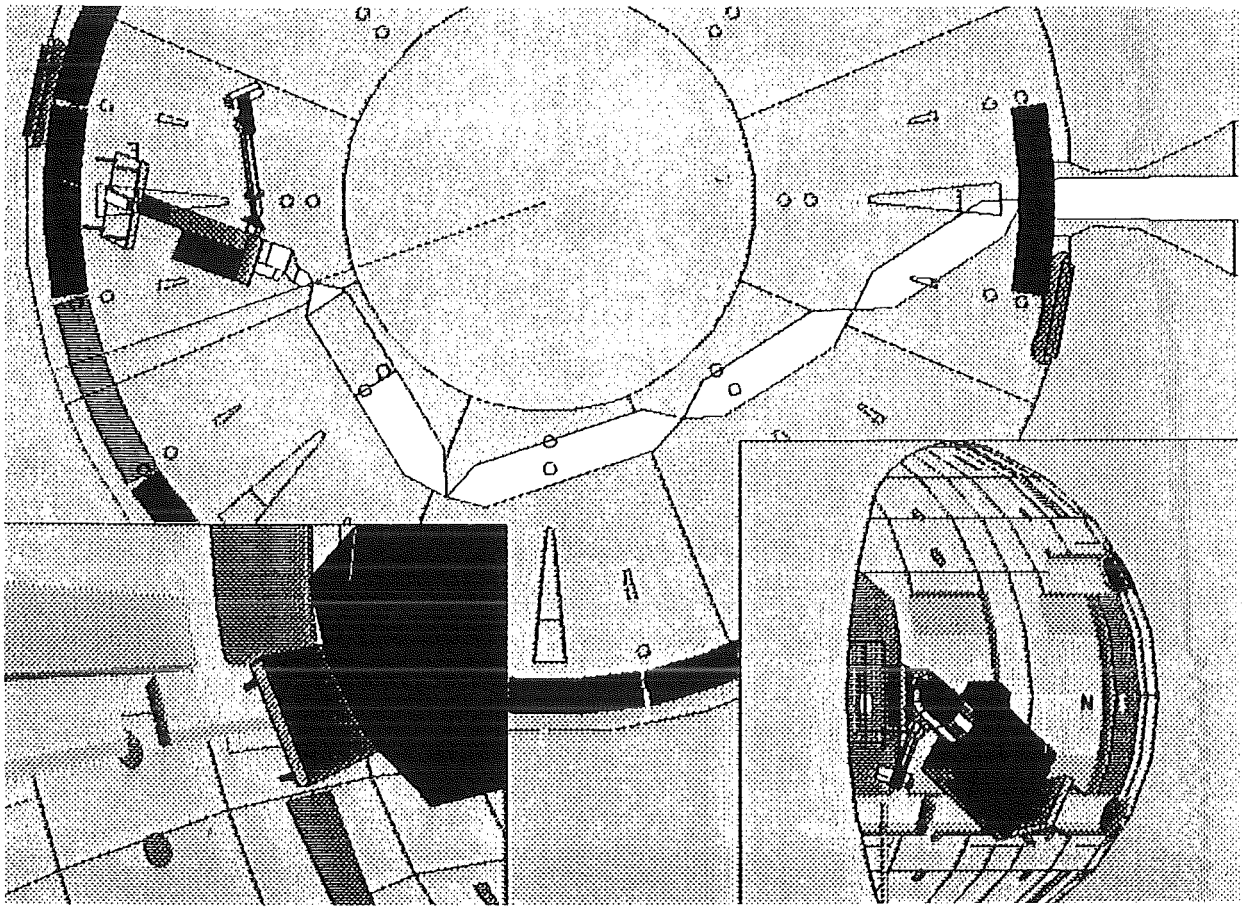

Fig. 64: JET boom simulator display (final stage): top view, side view, camera view; views from arbitrary in-vessel positions are possible

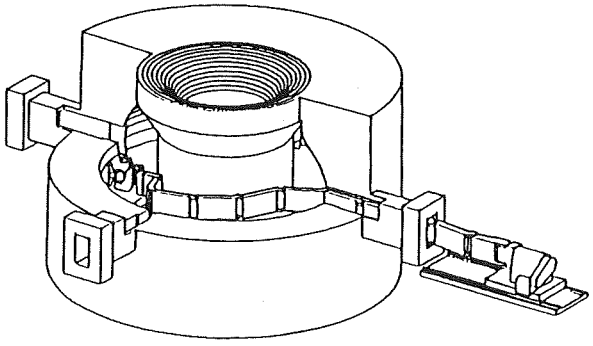

Fig. 65: NET boom model

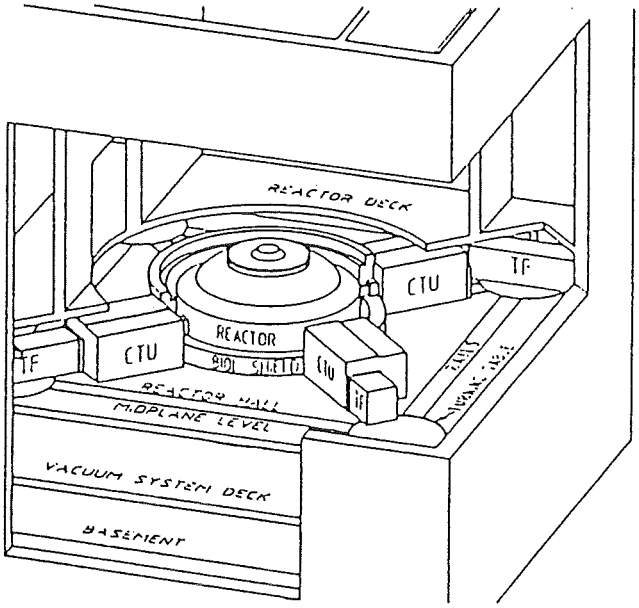

Fig. 66: NET torus hall with remote handling equipment

Test Facility

With respect to the very complex handling tasks and the rather sophisticated handling equipment required, assisting experiments will be needed already in an early stage. Therefore, KfK has launched the planning of EDITH, an experimental device for in-torus handling (Fig. 67). It is scheduled to become the test facility for the development of in-torus remote maintenance techniques of fusion devices. First tasks to be performed in EDITH will be the optimization of TU components, experiments related to the static and dynamic behaviour of the TU and investigations of control systems, man-machine interface and sensors.

SUB-TASK 2: Overall Geometry Measurement

The implementation of the prototype system for ex-vessel geometry measurements is going on as planned.
The following modules are running:

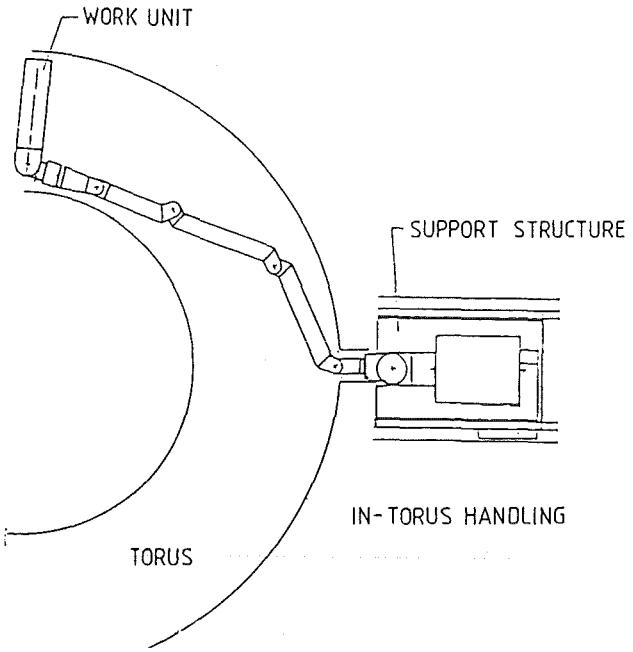

Fig. 67: EDITH-Experimental Device for In-Torus Handling

- postprocessor for interpretation of CAD data (points to be measured and their environment) in IGES data format,
- interactive tele-control of the theodolite, automatic measuring, triangulation computations for resection,
- automatical aiming at nominal point positions,
- preparation and output of results.

The prototype system GMS (Geometry Measurement System) is equipped with a single servo-driven theodolite. Up to now the theodolite is fitted with a laser-eyepiece and aiming points are observed with an external, manually-controlled camera. At present a CCD-camera is being installed on the theodolite periscope and the operator will control the sightings without using an external camera. For surveying without a time consuming levelling procedure it is planned to implement a bundle adjustment algorithm.

For **in-vessel** measurement a concept of theodolite-periscopes was worked out, which is based on triangulation using controllable mirrors in the measuring path.

SUB-TASK 4: Replacement of Protection Tiles

The replacement of protection tiles and the required work unit attachable to the TU for its performance is very dependent on the design of the tiles and their installation at the first wall and the divertor plates, respectively. Due to the lack of this design input it is assumed so far that for the tile replacement the IVHU equipped with the multi-purpose manipulator unit will be used.

Within the frame of the general in-vessel handling investigations and the accompanying ex-vessel handling considerations a family of four electrical master-slave manipulators was defined according to the required load capacity and the environmental conditions. The load capacities are varying from 10 through 300 kg. It is proposed to design the slave arms as modular units and to use for all types the same master arm design. [6]

SUB-TASK 8 & 9: Environmental Conditions

The market survey on sensors which might be utilized in the context of in-vessel handling was continued. The first report on relevant sensors had been issued about a year ago [7]. The survey concentrated on sensors with the potential for operation up to 150°C and $3x10^6$ rad/h over a significant period of time.

While the previous survey had emphasized various kinds of position sensors the present compilation of sensor data includes: strain gauges, force sensors, accelerometers, body-sound microphones, inclinometers, tacho-generators, limit switches, light barriers, reflection-based proximity sensors, fluidic high-temperature distance sensors, thermocouples, resistive thermometers, and pressure sensors.

A report on this survey is being prepared.

Another study [8] concentrated on the availability for gamma radiation hardened sensors, their base materials and semiconductor devices for signal pre-conditioning application. Taking in account a utilization time of 300 hours, an integral gamma dose compatibility of 1 Grad (Si) is required. The given environment conditions and the specific requirements of the system reduce the number of presently available sensors to a small selection of recommendable transducers and detectors and only few radiation hardened and successfully tested original materials to be used for installation into the NET boom.

Besides radiation and temperature compatibility, additional requirements apply to the sensors (inclinometers, tactile and nontactile proximity devices, switches, ultrasonic transducers, optical sensor instrumentation, glass fiber, lenses, cameras) regarding their dimensions, weight and adaptability to the boom. Moreover, it should be possible to replace the sensors conveniently also in cases where additional components have to be installed for cooling and shielding.

The report relates to sensor components whose gamma compatibility is known from publications and from information received from manufacturers. In some individual cases results of irradiations performed recently are available which are representative of the presently achievable resistance of a component or a group of devices.

A survey of all components analyzed for the RM3 remote handling system points out that progress in the availability of radiation hardened instrumentation systems is a critical path item for the design of manipulators and inspection machines for fusion reactors. For a great number of basic materials and especialy for particular semiconductors it is concluded that radiation hardness increased only by a factor of three or less during the last five years, disregarding their marketing demands. On other hand, the development in the field of radiation hardened semiconductors makes clear that the conventional and classic thin-layer technique has reached physical frontiers limits and therefore noticeable

progress can be expected only from specific NMOS, CMOS and Schottky-barrier semi-conductors being developed now and tested individually. It can be concluded that radiation hardened transistors and integrated circuits in some exceptional cases are already available, but a sufficient useful number of multi-purpose discrete semiconductors and medium- scale integrated circuits will be made available only in a few years.

Plastics and glasses play a considerable part in sensorics. Under conditions of gamma radiation a remarkable progress is observed which gives rise to the assumption that usable and applicable materials are already available or will be offered for a broader application in this field before long, fulfilling the requirements of being stable at temperatures above 120°C.

For untested original materials and sensors, a supplementary radiation hardening program is indispensable. It should be established in time to perform the needed tests in an irradiation facility, since the irradiation procedure takes time in the scale of many months and cannot be compressed due to limitations for the allowable gamma transients. According to this objective, a design was started for the preference of distinct sensors being considered for a first gamma irradiation test in the BR-2 reactor at MOL/Belgium, including an on-line measuring instrumentation and control system.

Staff:

K. Becker
J. Benner
G. Böhme
H. Breitwieser
Fr. C. Fischer
B. Haferkamp
E. Holler
J. Hübener
H. Knüppel
B. Köhler
G.W. Köhler
I. Kornelson
R. Krieg
U. Kühnapfel
K. Leinemann
W. Link
G. Müller
J. Reim
H.A. Rohrbacher
E.G. Schlechtendahl
A. Suppan
W. Till
Fr. E. Wehner

References:

[1] Suppan, A., et al. Unpublished Report of the KfK, March 1988

[2] Suppan, A., Hübener, J.: Ivestigations of In-Vessel Handling Concepts for NET.
IAEA Technical Committee Meeting on Robotics and Remote Maintenance Concepts for Fusion Machines, Karlsruhe, 22.-24.2.1988

[3] Leinemann, K., Schlechtendahl, E.G.:
Unpublished Report of the KfK, June 1987.

[4] Kühnapfel, U., Leinemann, K., Schlechtendahl, E.G.: Graphics support for JET boom control. Proceedings International Topical Meeting on Remote Systems and Robotics in Hostile Environments.
Pasco, Wa., March 29 April 4, 1987, S.28-34

[5] Leinemann, K., Kuehnapfel, U., Ludwig, A.: Remote Handling Control with Graphical Man-Machine Interface for NET and JET. IAEA Technical Committee Meeting on Robotics and Remote Maintenance Concepts for Fusion Machines, Karlsruhe, 22.-24.2.1988

[6] Köhler, G.W.: Electric Master-Slave Manipulators for Remote Maintenance in Fusion Plants.
IAEA Technical Committee Meeting on Robotics and Remote Maintenance Concepts for Fusion Machines, Karlsruhe, 22.-24.2.1988.

[7] Kornelson, I.: Unpublished Report of the KfK, December 1986.

[8] Rohrbacher, H.A.: . Unpublished Report of the KfK, Nov. 1987.

S + E 4.1.2 Safety Aspects of the Cryosystem

Under this task safety aspects of the cryostat of NET are investigated. The cryostat surrounds the torus and all coils. It has to maintain high vacuum conditions. To guarantee the integrity of this outer pressure loaded vessel the complicated buckling behaviour has to be studied for normal and accident conditions.Another goals to develop a nondestructive buckling detection device for cryostat experiments. Furthermore the study of the buckling behavior should give a feedback to optimal cryostat design.

In order to investigate the buckling behaviour for different accident situations a simplified strategy [1] to calculate the buckling loads has been developed.

Experimental investigations for code assessment and nondestructive buckling load measurements have been continued. The following two figures show the test facility and

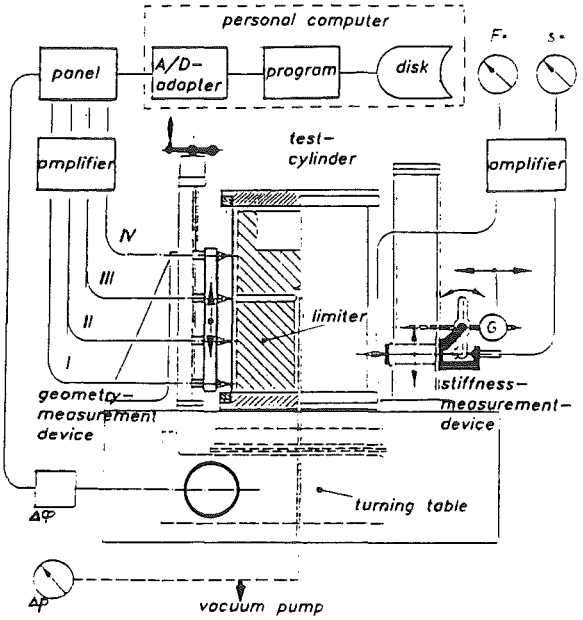

Fig. 68: Buckling test facility for displacement and stiffness measurements

an example of results of deformation measurements of the test cylinder before and after loading in the prebuckling and postbuckling phase. These measurements serve to analyse the influence of geometrical imperfections on the deformation and the buckling load. During prebuckling deformation the imperfection pattern of the cylinder surface is gradually transformed into the regular buckling pattern.

The third figure shows the results of stiffness measurements for different circumferential positions in the middle of the cylinder height. The figure demonstrates the decreasing stiffness due to the increasing buckling load. For a nondestructive determination of the buckling load the sample is loaded by forces smaller than the expected buckling load. Then the resulting curves of the stiffness versus load have to be extrapolated to zero stiffness. This gives a prediction of the buckling load.

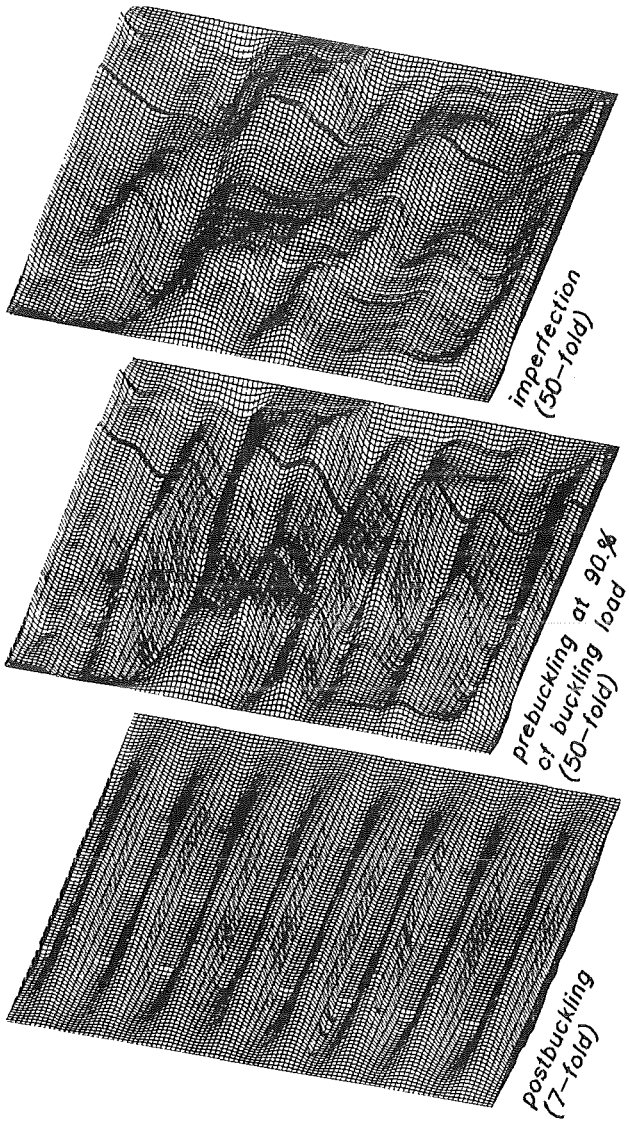

Fig. 69: Radial deviations from the circular cylinder (different scale factors)

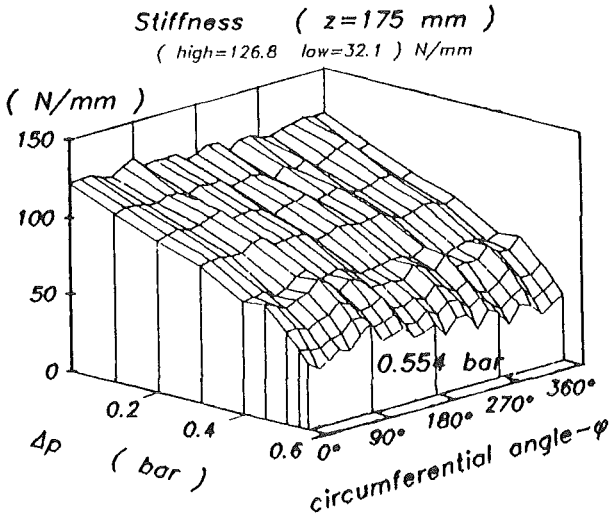

Fig. 70: Load-dependent circumferential stiffness values in the middle of cylinder height (z = 175 mm)

The experiments will be continued with different geometrical and load imperfections.

In the first proposal the cryostat for the NET-reactor was a thin stiffened shell. Meantime an alternative cryostat design is under discussion where the thick biological concrete shielding is combined with the cryostat vessel. In consequence of this design the buckling load of the vessel is far beyond the cryostat loading. However, buckling problems may occur for the inner steel liner which is connected to the concrete shell only at discrete points. Calculations show that for a liner thickness of 1 mm the distance of anchor points should not be more than 25 mm. For a liner thickness of 4 mm the distance is 200 mm, but a thicker liner may produce detrimental electro-magnetical interferences with the coils.

Staff:
B. Dolensky
R. Krieg
T. Malmberg
S. Raff
E. Wolf

Publication:

[1] S. Raff, B. Dolensky, R. Krieg, 'A simplified procedure for elastic buckling analysis'.
Transactions of the 9th SMIRT, Vol. B, p. 569-574, Balkema Rotterdam, Boston 1987

S + E 4.1.3 Safety Aspects of Superconducting Magnets

During operation of superconducting magnet systems disturbances are conceivable which could finally result in the destruction of a magnet. The energy discharged thereby into an electric arc may lead to damage of the surroundings of the magnet. Cause and course of the disturbances, their detection and identification as well as their possibly destructive consequences are to be investigated using the superconducting torus arrangement TESPE-S. Through development of codes and their verification on the TESPE-S experiment an attempt will be made to transfer the results to other larger magnet systems.

In case of destruction by arcing a number of different faults may occur simultaneously, e.g. loss of cooling, loss of vacuum, conductor short circuits. In order to keep theory and experiment transparent, in our experiments such failures are first simulated and built-in in separate experiments, respectively, and initial non-destructive tests are performed. The work includes the faults mentioned above and the generation of electric arcs. At the end of the series of experiments an attempt will be made to demonstrate that a destructive arc in one coil can be mastered safely.

After having performed loss-of-coolant, loss-of-vacuum, short-circuit and first arcing experiments, these latter ones were continued by studying the behavior of the magnet system with an electrical arc short-circuiting one coil or the total system. Out of the 3 experimental techniques for arc initiation, described earlier, we have chosen the following for the major fraction of further investigations: The vaporisation of a thin copper wire between the electrodes of a magnet during discharge of the magnet system that leads to an arc being supported by the discharge voltage across the electrodes, which are placed in a helium-gas filled chamber.

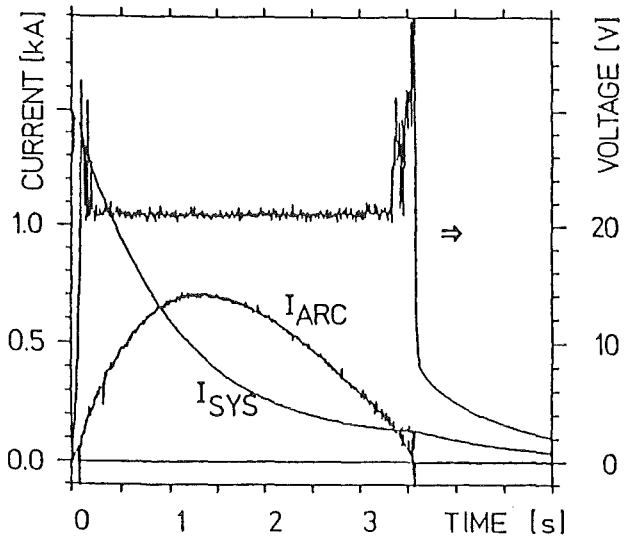

Fig. 71: Arc current, arc voltage and system current vs. time.

For a stationary free burning arc the voltage is fairly constant (Fig. 71) with its height depending on ambient atmosphere and electrode separation. Only at the starting point and also at the end of burning a voltage peak appeared for short periods. The arc current rises from zero to a maximum and falls back to zero. The height of this maximum and the length of the burning period depend strongly on system current and burning voltage.

Experiments with arcs through holes or slits showed the significance of spatial restrictions. Therefore, the next step after the case of a free burning arc was to simulate a closer approach to the geometry of magnet windings. A smaller sized chamber was constructed which could withstand pressure rises up to about 5 bar and to which a small magnetic field could be applied. While these experiments are being evaluated, first results showed a considerable mobility of the arc often hitting the chamber walls with consequent partial destruction. Melted metal sometimes formed electrical bridges short-circuiting the arc which consequently extinguished, but was re-initiated when the metal bridge was vaporised by ohmic heating.

Movement of arcs and 'stopping power' of different materials was studied with an experimental arrangement applying two parallel rails mounted on the electrodes of the magnet system. Due to the interaction of the arc current with its self included field, the arc is accelerated along the rails. Pieces of different materials were placed near the end of the rails to investigate their capability of stopping the arc's movement. These experiments are still being evaluated.

For all these experiments theoretical modelling was started and the MSCAP computer code was used to calculate the behavior of arc current, arc voltage and system current. This code from INEL Idaho is capable of including time-, voltage- and current-dependent voltage supplies, current supplies, resistors, capacitors and inductors. Good agreement between experimental and theoretical results is found.

In continuation of the safety analysis of components of superconducting magnet systems, the fast discharge system of the Large Coil Test Facility remained at the focus of considerations. Calculations, based on the preliminary reliability data base, identify the redundant-logic controllers as the critical components in the design. The controllers are responsible for the logic decisions in case of a demanded current discharge. The uncertainty is originated from the error detection in case of a fault in those components. But besides this, the Common Mode Failure in the controllers and in the power switch system are the dominant factors influencing the overall reliability.

Staff:
P. Duelli
J.S. Herring
K.P. Jüngst
H. Kiesel
H. Kronhardt
G. Obermaier
M. Oehmann
H. Schnauder
J. Seibert
E. Süss
A. Wickenhäuser
H. Yanagi

S + E 5.2.2 Behaviour of Gaseous Tritium in the System Plant/Soil

In the frame of this project several samples of plants exposed to atmospheric HT during the Canadian HT-release experiment in June, 1987, were analyzed for OBT. The same samples will be analyzed in Canada by another method of sample preparation. Results will be compared and introduced into a CFFTP-report.

Though the exposure conditions of plants differed from those during the French experiment, the results can be compared quite well. In most cases it has been shown that the course of the tritium concentration in plants was typical for a pure HTO-contamination. Concerning the influence of HT on the tritium concentration in plants it can only be pointed out, that despite much higher HT-concentration in the air (factor 10^4 more) the effect was not stronger than after a pure HTO-contamination. An exception were soybean plants with higher tritium concentrations in free tissue water and OBT than in other plants. The reason seems to be the intentional inoculation of the seeds with a strain of nitrogen fixing bacteria (Rhizobium japonicum). These bacteria cause the formation of root nodules in leguminouses. Moreover they contain the enzyme hydrogenase which catalyzes the oxidation of molecular hydrogen.

In this case a certain influence of HT on tritium contamination is not excluded.

Detailed results are presented in [1].

Plant contamination with HTO under climatic chamber conditions has been continued. Maize, beans, grass and lettuce have been grown in an HTO environment of about 10^6 Bq/l in atmospheric and soil water. The separation into different organic components is in work.

Perspectives for the Period April - September 1988

Definite start of HT-experiments in the climatic chamber in April 1988.

Staff
S. Diabaté
D. Honig
H. Schüttelkopf

S + E 5.4 Overall Plant Accident Scenarios for NET

Besides the system related safety studies performed under the topics S+E 4 this work concentrates on the interactions of the different systems and the integral behaviour of the plant.

The procedure is that for the main systems severe accidents are postulated. Then the consequences are studied roughly. The question in these studies is whether the initiating failure will have any impact on other systems.

Under the heading of identification of accident sequences based on engineering judgement in the period reported here a first set of 'reference accident' scenarios was agreed in the overall plant accident scenarios working group of NET. These are:

a) Propagation of an arc in a winding of a TF coil.
b) LOCA in the blanket cooling systems.
d) Water ingress into the vacuum vessel.
e) Air ingress into the vacuum vessel.

For some of the accidents listed analyses are already available (e.g. a) and e)) but the accident scenarios have to be specified in more detail to be consistent with the present stage of the NET design. KfK will investigate scenario a) under the S+E topic 4.1.3.

Under the heading of identification of accident sequences based on probabilistic risk assessment a large study analysing the whole plant was initiated by the NET team. The work will be performed in French and Italian laboratories and reported to and discussed with the overall plant accident scenarios working group of NET. The work has to be completed in July 1989 when the present predesign phase is terminated.

Staff:
R. Meyder

S + E 5.5 Development of Safety Guidelines for the Design of NET

This task being performed in the framework of a special working group aims at ensuring advice to NET on safety and environmental guidelines. The group members belong to the following associations: CEA/IPSN, ECN-Petten, JRC-Ispra, KfK-Karlsruhe, RisØ National Laboratory, The NET-Team, UKAEA/SRD.

The discussions of the drafts of different previous contributions within the working group and with members of the NET Team showed that there are partially different opinions especially concerning the extent of the documents, the proposed methods and safety assessment procedure, and the values for radiological dose targets.

From KfK's side a proposal was made for a new structure of the documents with three parts (instead of the previous two): (1) General Safety Related Recommendations, (2) Plant Description and Methodology for Safety Assessment, (3) Specific Safety Related Recommendations, related to the different systems of the plant.

A revised draft of Part 1 was elaborated (Version February 1988). The main contents of these General Safety Related Recommendations deals with safety objectives of NET, fundamental recommendations and radiation protection, proposed radiological dose values including non-ionizing radiation, a short description of methods and safety assessment procedure, and a hint to the safety series of the NUSS programme of the IAEA which may also help to guide the design of NET.

Staff:
W. Kramer
R. Krieg
R. Meyder

T 6 Industrial Development of Large Components for Plasma Exhaust Pumping

On behalf of the Commision of the European Communities (CEC) a working group of CEA and KfK elaborates the specifications and conducts the development of large vacuum components for NET. Two alternative solutions for plasma exhaust gas pumping are pursued in parallel: mechanical pumps and cryopumps. The large components required (high vacuum pumps, roughing pumps, and valves) are not commercially available at present. It is planned to develop them within T6.

Turbomolecular Pumps

Within the framework of the study on turbomolecular pumps investigations have been performed into the loadability of the bearings. The accident consisting in abrupt pressure surge in the torus has proved to be critical with respect to the bearings.

The following two events may result in an accident:
- rupture of a window towards the atmosphere,
- rupture of a coolant water line.

The NET team has estimated the rate of pressure surge for these two cases. In case of rupture of the window (100 cm^2 opening) the pressure in the torus rises to atmospheric pressure within 1000 s. In case of rupture of a water line the pressure rise proceeds much faster; it can be calculated with the formula $P(t) = 0.03\ t$ (P expressed in bar, t in s).

For the critical case of water line rupture the axial bearing force was calculated as a function of time for the vertical single-flow pump design. For about 2130 kg rotor weight the force increases to a maximum of 160 kN within a few seconds. The S2M company has been able to prove that this accident can still be controlled by the active electromagnetic bearings.

In case of failure of the electricity supply of the bearing a dry running roller bearing must accommodate the whole bearing force. No evidence has been provided so far of the performance of dry running, a force accommodating bearings under vacuum. The temperature of dry running bearings increases by about 15 K per second. This problem will not be examined in the current study, but separately.

On account of the problems associated with the sudden pressure surge, double-flow variants have been investigated besides the single flow 50.000 l/s TMP. Due to rotor symmetry the double-flow variants do not exhibit an additional bearing force in an accident of the type described before.

The investigations show that double-flow pumps due to their smaller rotor diameter are also characterized by the more advantageous cutdown pressure (i.e., the pressure at which the pumping speed drops abrutly). Therefore, a double-flow pump attains a higher throughput compared with a single flow pump having the same suction capacity.

Compared with the data calculated for the single flow 50.000l/s TMP and for the double flow 50.000 l/s TMP and 15.000 l/s TMP, the superiority in terms of throughput of the pumps having smaller rotor diameters is very clear. Three 15.000 l/s TMPs each per divertor could be installed in the NET reactor. Besides the gain in throughput, use of pumps with smaller rotors would offer the advantage of the lower development hazard as compared with the large 50.000 l/s TMPs. As a matter of fact, one could profit from experience accumulated with the presently series manufactured rotors having slightly smaller diameters.

TMP Type	single flow 50000 l/s	double flow 50000 l/s	double flow 3x15000l/s
circumferential speed (m/s)	470	470	470
rotor diameter (mm)	1500	1060	600
number of stages	12 (17)	2x12 (2x17)	2x12
rotor weight (kg)	1850 (2130)	800 (1125)	420
pumping speed for helium (m^3/s)	54	42	42
compression ratio for hydrogen	$>5x10^4$ ($>10^7$)	$>5x10^4$ ($>10^7$)	$>5x10^4$
throughput at 10^{-2}mbar (mbarl/s)	60 (90)	85 (120)	150
sudden venting force (N)	10^5 ($1{,}6x10^5$)	0	0
total length (m)	2,5 (2,9)	3,8 (4,5)	1,9
development effort	large	medium	small

Tab. 13: Comparison of TMP data

Gate Valves

A search relating to literature published and patents granted on the design concept of existing all-metal valves has been performed. The results have been summarized in an interim report.

Forepumps

The results of invitations to bid for the forepump study are available. A proposal for awarding contracts has been prepared.

Prototype Testing

Concept studies have been performed with a view to planning a pump station for testing prototypes of the large vacuum components under simulated conditions of NET.

Staff:
H. Haas
M. Lieberknecht
A. Mack
D. Perinić

T7 Optimization of Cryogenic Vacuum Pumping of Helium

The objective of experimental investigations into helium and plasma exhaust cryopumping consists in comparing and asessing in a test series performed on a reduced scale the multitude of possible technical alternatives of helium cryopumping with the aim to achieve design data and operation requirements for the compound cryopumps to be used in the torus vacuum system of a fusion machine.

The best suited technical solutions will be optimized under simulated NET operating conditions. The result of the investigations will be a specification of the active cryopumping surface for the NET plasma exhaust.

Work on this project has been performed so far under a NET study contract.

The planning and design of the TITAN facility have been terminated. This facility will be used for cryopumping tests with sorption panels up to 400 mm diameter. The design documents have been approved for fabrication to proceed.

The TITAN facility has been designed to accommodate two possible accidents: hydrogen deflagration and air ingress. The vessel of the cryopump has been designed to withstand the maximum admissible overpressure during operation of 10 bar. This means that the environment is protected by the vessel wall against the impacts of postulated hydrogen deflagration taking place in the interior of the vessel at the maximum possible overpressure of <8 bar.

The second postulated accident, air ingress during cryogenic operation causes quick evaporation of the cryogens. All three cryogenic vessels have been designed to withstand failure in such an accident and have been protected accordingly.

Calculations on the pressure rise in an accident have been performed for the three cryogenic vessels of the TITAN facility. A maximum heat flow density of 3.8W/cm^2 has been assumed for the not insulated vessel parts. The heat flow density assumed for the superinsulated surfaces is 0.6W/cm^2. Based on these values a maximum evaporation rate of 455 g/s is obtained. The corresponding resistance of flow through two blowdown pipes (16 mm ND) is calculated to amount to 0.625 bar.

The LHe evaporation rate in an accident is 315 g/s for the inner LHe vessel. The resulting resistance of flow through two blowdown pipes (16 mm ND) is 0.407 bar.

The rate of LN evaporation determined for the LN annular vessel is 200 g/s. This gives a resistance of flow through two blowdown pipes (16 mm ND) of 0.322 bar.

Starting from these calculations, the safety valves for the three cryogenic vessels have been designed. Each of the three vessels is equipped with a blowdown pipe to the atmosphere which can be opened via a non-return valve. The second parallel pipe is protected by two safety valves in parallel with discharge into the atmosphere. These are a safety valve ND40 and a rupture disk ND40. The overpressure at which the safety valve responds is 0.5 bar; the rupture disk gets effective at 1 bar.

Heat balance design computations have been performed for normal operation of the TITAN facility in order to determine the maximum time of operation between two LHe refill steps. Considering the large baffle surface, the LHe annular vessel is a critical component.

The following contributions have been taken into account in the computation: enthalpy difference and condensation heat of the gas at the baffle; heat radiation of the environment; heat conduction of the gases; heat conduction via structures.

The following heat output can be calculated for the entire LHe annular vessel with the baffle included:

	10^{-4} mbar 1 mbarl/s	10^{-3} mbar 10 mbarl/s
Baffle	0,458 W	3,216 W
Cylinder jacket	0,166 W	0,194 W
Pipes	0,353 W	0,353 W
Total heat load	0,977 W	3,763W

Table 14

At 10^{-4} mbar 32.3 l Lhe were consumed per day with a filling level left of 125 mm. At 10^{-3} mbar 51.9 l LHe/h are required. The inner LHe vessel can be operated for 72 h at 10^{-4} mbar; at 10^{-3} mbar helium consumption is 0.54 l LHe/h.

The volume of nitrogen required by the LN annular vessel inclusive of the baffle is 1.7 l LN/h at 10^{-4} mbar and 2.1 l LN/h at 10^{-3} mbar. The nitrogen consumed is replaced continuously.

Trial operation of the HELENE facility, which is for helium cryosorption screening tests, has been continued during the period of reporting.

Staff:
H. Haas
J. Hanauer
W. Höhn
B. Kammerer
U. Kirchhof
H. Lukitsch
A. Mack
D. Perinić
D. Zimmerlin

T10A Plasma Exhaust Purification by Means of Cyrosorption on Molecular-Sieves or Alternative Adsorbents

The fuel cycle of a fusion reactor requires simple processes for the removal of impurities from gaseous streams such as the plasma exhaust gas, the solid blanket coolant, the blanket purge gas, etc. One process step considered in this context is cryosorption on molecular sieves or other adsorbents. To evaluate this alternative information is needed on the adsorption of fusion fuel cycle impurities, e.g. hydrocarbons, NH_3, CO, CO_2, H_2O, as well as mixtures of these gases from a He or a hydrogen carrier gas. In the latter case cosorption of hydrogen is of particular concern.

For the experimental study a closed loop, to be installed in a glove box, is presently under construction. The glove box, previously in use for other experiments, has been decontaminated and adapted to the new work. Detailed planning of a cryostat, which will be integrated into the loop, is now completed and presently under construction. The cyrostat will be UHV tight and therefore tritium compatible.

Present efforts concentrate on the development of appropriate analysis of hydrogen isotopes. A small-volume ionisation chamber has been tested and calibrated with trac amounts of tritium. Numerous calibration curves w ith isotopically substituted hydrocarbons and ammonia have been obtained by Fourier Transform Infrared Spectroscopy for single species as well as for gaseous mixtures. Similar calibration studies have also been carried out for CO, CO_2 and H_2O.

In screening experiments employing a flow system water adsorption in therms on geolite SA were determined from break-through curves. The water content in the helium carrier gas was followed with a hygrometer. Regeneration of the geolite was carried out at 400°C by sweeping with very dry helium.

Staff:
U. Tank
H.E. Noppel
R.D. Penzhorn
E. Willin

T10C Plasma Exhaust Gas Purification by Use of Hot Metal Getters

1. Objectives

Investigation of hot metal getters as a process option for the purification of the plasma exhaust gas of a fusion reactor. It is assumed that molecular hydrogen species like HD, DT, D_2, are removed by a Pd/Ag permeator in a first purification step. It is then the task of the getters to recover chemically bound hydrogen isotopes by decomposition of hydrocarbons and water and to remove impurities like N_2, CO, and CO_2 from the He gas stream.
The main program steps are:

A. Inactive tests on various getter metals and alloys (e.g. Zr-AL, Zr-Fe-V, Zr-Co) to study sorption speeds, retention capacities and cracking capabilities as a function of temperature, pressure and presorption.

B. Active tests with tritium to demonstrate the purification efficiency under more realistic operational conditions.

2. Current Progress

The assembly of the PEGASUS facility (cf. Fig.72) tests has been continued as scheduled. The stage A, designed for inactive tests, has been completed by installation of water cooling devices for the turbomolecular pump as well as for 3 SAES getter beds and 2 uranium beds. In addition, an electro-pneumatic control system is now available for some of the most frequently used valves. During the preliminary test period, the electrical insulation of the first getter bed became defective. As a consequence, the getter unit was sent to SAES for repair and the power supply was modified to prevent similar failures in the future.

In the meantime, the design, construction, and acquisition of equipment for experiments with tritium tracers has been continued. The following components have been ordered and are being installed:

- uranium beds U1 and U2;
- gas collection tank B3 for take-up of the test gas prior to tritium restorage in U1 and U2;
- glove box windows supplied with about 100 electrical feedthroughs for heaters, thermocouples, pump and valve controls, pressure gauges, etc.;
- heat removal system for the glove box atmosphere which will be dry air with a pressure difference of -3mbar relative to the laboratory; this system is needed because the internal heat sources (pumps, GC, purifiers, manifold baking devices) may produce up to 10KW of thermal power;
- data processing system for the gas chromatograph (PC-work-station with Baseline 810 interface and software).

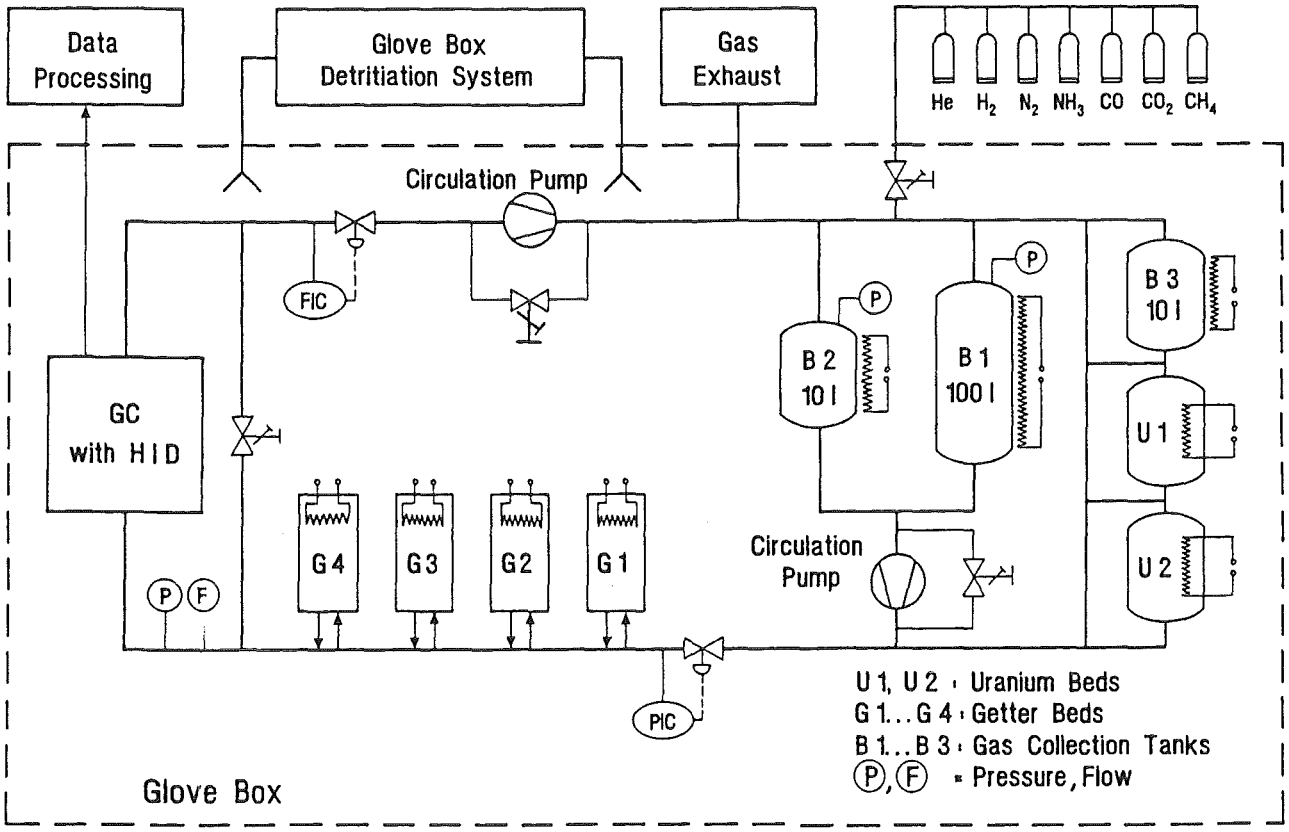

SCHEMATIC DIAGRAM OF THE PEGASUS FACILITY

Fig. 72

In addition, a detritiation system for the glove box atmosphere has been designed and commissioned. This system will continuously remove traces of tritium released from the loop during normal operation; however, it will also be able to retain the total tritium inventory of the box in the case of an accidental release.

Staff:
H. Albrecht
T. Kastner
U. Kuhnes
K. Schuster

3. Plans for the Near Future

- continue and complete preliminary tests of single components;
- start measurement in H_2 absorption/desorption behavior of the SAES purifiers and on getter properties with respect to impurities;
- continue installation of devices for tritium experiments.

T10E Adsorption of DT on Heated Metal Beds other than Uranium

The separation and preparation of the gases D, T, He and impurities from the plasma exhaust are an urgent problem during the operation of the fusion reactor. To employ adequate methods, an exact analysis is important. The relevant gases CO, CO_2, CH_4, H_2O and NH_3 are analysed by gas chromatography and mass spectrometry. These methods fail, however, if the deuterated and tritiated species have to be differentiated. One possibility to measure these molecules is the use of the FT-IR-Spectroscopy.

In the Institute of Radiochemistry calibration curves were made and mixtures of the gases were measured. During the last months the deuterated compounds of methane were analysed and the interaction among them was determined. No isotopic exchange took place between two molecules as well as several compounds (methane-d1, -d2, -d3 and -d4) during the measured time (up to 2 hs). The peaks of the individual methanes were clearly distinguishable. NH_3 and ND_3 were examined as well. New peaks appeared in the spectrum of this mixture and the pure compounds could not be distinguished. Further analyses show that NH_3 and ND_3 exchange immediately and, therefore, all compounds (NH_3, NH_2D, NHD_2 and ND_3) exist simultaneously. The pure compounds ammonnia-d1 and -d2 are not available and, therefore, it is obvious that it is impossible to make calibration curves of these species. For this reason a graphic-mathematic method was developed and tested to determine the concentration of all species.

The figure shows for example the spectrum of a mixture of CHD_3, (200 mbar), CH_4 (106 mbar) and NH_3 (64 mbar) the path length was 10 cm.

Staff:
Dr. R.-D. Penzhorn
Fr. Nolte
Dr. E. Willin

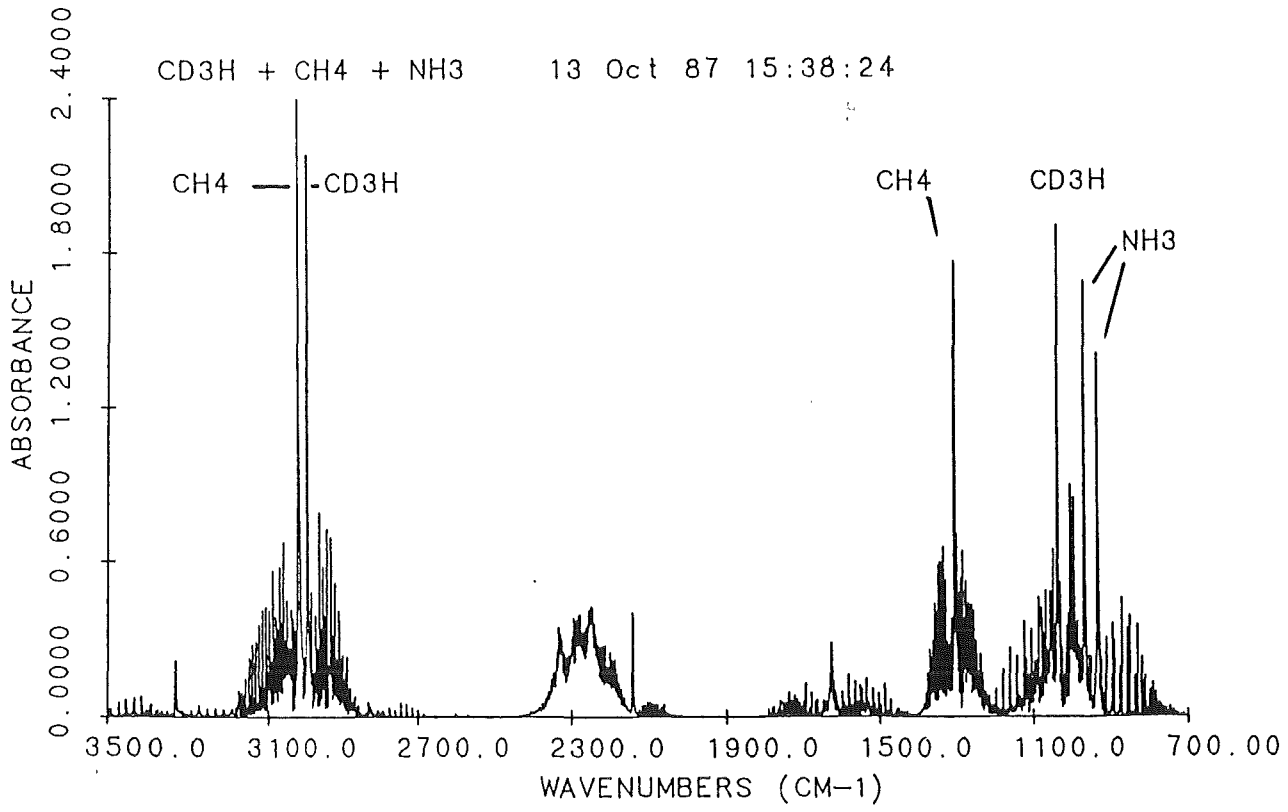

Fig. 73

T10H Catalyst Development Exhaust Purification Process

For the plasma exhaust cleanup of a fusion reactor a process concept based on the hydrogen isotope purification through palladium/silver alloy permeators combined with selective catalytic reaction steps is proposed, which avoids intermediate conversion of purities into water (see Fig. 1).

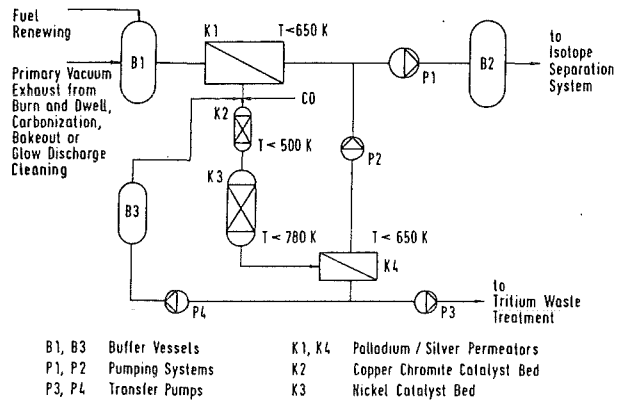

Fig. 74: Fuel cleanup process concept

The main process step consists in the separation of the unburned fuel from the impurities with an array of palladium/silver permeators operated at $575 < T < 650$ K. For a 20 mol/h hydrogen stream (NET design requirements) a total membrane surface of the order of 0.5 m^2 is required.

Hydrogen isotopes associated to water present in the effluent stream of K1 are recovered according to the water gas shift reaction:

$$CO + H_2O = CO_2 + H_2 \qquad (1)$$

Screening tests with a gaseous mixture of typically 2 kPa H_2O and 6 Kpa CO diluted in He up to 100 kPa employing the conversion catalysts

a) $CuO\text{-}ZnO\text{-}Al_2O_3$
b) $Cr_2O_3\text{-}CuO$
c) $Fe_2O_3\text{-}Cr_2O_3$
d) $CoO\text{-}MoO_3\text{-}AL_2O_3$
e) $CuO\text{-}ZnO\text{-}Cr_2O_3\text{-}Al_2O_3$

showed that at 420-520 K thermodynamic equilibrium can only be attained with catalysts b) and e). Of these two, the zinc stabilized copper chromite catalyst is preferred because of kinetic considerations.

Methane and other hydrocarbons decompose reversibly on a nickel catalyst into carbon and hydrogen:

$$CH_4 = C + 2H_2 \qquad (2)$$

Experiments show that methane can be decomposed quantitatively into the elements when the hydrogen liberated by the cracking reaction is continuously removed with palladium/silver permeators. Under these conditions the decomposition reaction of methane was found to be first order in methane and to have an activation energy of about 100 kJ/mol at temperatures below 800 K. The rate for the decomposition of methane was found to be

$k2 \simeq 10^{14}$ molec/$cm^2 \cdot$ sec

To measure the life-time of the catalysts experiments were carried out in a flow system employing partial flow rates that simulate NET process requirements. The results of the experiments can be summarized as follows:

- equilibrium decomposition of methane can be attained at 530°C with less than 10 g catalyst and
- the amount of catalyst required for the decomposition of methane without loss of activity (and without regeneration) is of the order of

  10 g catalyst/mol CH_4.

From the above it is concluded that only about 25 kg of commercially available nickel catalyst are required to clean up the fuel from the total normal burn and dwell period of NET.

The hydrogen permeation rate Q_H (in mol-cm/cm^2-min-$kPa^{1/2}$) through commercial palladium/silver diffusers of 289 or 578 cm^2 surface area was found to be given by the expression

$$Q_H = 1.00 \times 10^{-6} \exp(-1300/RT),$$

which is in good agreement with the results of other investigators, who employed diffusers of less than 10 cm^2 permeation area. The measured hydrogen permeation rate was found to be essentially independent of the type of carrier gas, i.e. N_2, He or CH_4.

In a series of runs the influence of CO, CO_2 and H_2O on the rate of permeation of hydrogen diluted in helium through a permeator of 289 cm^2 surface area was studied at temperatures between 370 and 720 K. The results allow the following conclusions:

- The hydrogen permeation rate is essentially not influenced by water in the concentration range $(2\text{-}10)\cdot10^{-4}$ mol/l ($p_{H_2O} < 2$ kPa) at temperatures between 370 and 670 K.
- Within the temperature range 570-720 K the permeation rate of hydrogen is only slightly reduced by carbon monoxide concentrations up to 8.18·10-3 mol/l ($PCO \leq 20$ kPa). Below 570 K the hydrogen permeation rate decreases with decreasing temperature in the presence of carbon monoxide.
- With respect to the permeation of hydrogen water and carbon monoxide show the same behavior as single components and the mixture.

Staff:
Dr. M. Glugla
Mrs. K. Günther
Dr. R.-D. Penzhorn
Dr. R. Rodriguez

Development of ECRH Power Sources at 150 GHz

A new version of the KfK gyrotron has been tested successfully, achieving an output power in excess of 200 kW in pulsed operation. Particular control of transient beam parameters enabled a stable high power operation in a parameter range, which was previously unaccessible.

The second version of the modular gyrotron includes a new resonator with a cylindrical center section of a length of 10 mm. A new gun section was used to overcome emission problems. All other components are identical with the previous version.

Test operation of this tube showed a quite close correlation between operating frequencies measured at various modes and the frequencies calculated from mechanical measurements after production of the resonator. The measured frequencies of 147.25 GHz for TE 231, 150.25 GHz for TE 031 and 155.28 GHZ for TE 521, respectively, deviated by less than 50 MHz.

The output power in the 100 kW range for all these modes was achieved with the regular starting procedure. The accelerating voltage for the beam was already applied when the beam current started by means of the gun voltage transient. A moderate increase in output power was possible by variation of the magnetic field slope over the resonator length. Unfortunately the imperfect superconducting magnet system (#1) used up to now did not allow further optimization.

Major improvement was achieved by simultaneous transients both in beam and in gun voltage. By this method, the stable operation of the TE 031 mode has been extended into the parameter range of high power oscillation (200 kW), where, with the regular excitation method, the TE 231 mode oscillates at a lower output power. This behaviour coincides with expectations resulting from theoretical mode competition studies. The efficiency of ~ 20% is not yet satisfactory; this is probably related to the beam properities which deviated from the calculated ones. As animprovement, integral outgassing of the next gyrotron version will be provided.

The theoretical mode competition studies have been extended by including harmonic oscillation (excitation at a multiple of the electron cyclotron frequency) in the calculation . As a result, harmonic mode competition must be expected. Harmonic operation of the gyrotron at 150 GHz has been demonstrated using 50% of the nominal magnetic field. Only a moderate output power of about 20 kW has been observed during this test.

In the meantime, the gyrotron experimental set-up has been disassembled for replacement of the superconducting magnet. With the new magnet, the influence of the magnet taper on the gyrotron properties shall be studied.

In addition to the continuing experimental program, a new gyrotron for 140 GHz is under construction. In the modular laboratory version of this gyrotron, an improved gun and a turnable window will be pretested with a view to their later use in the prototype gyrotrons. These prototypes will be integrally brazed tubes for plasma heating application at the W VII AS stellarator. The mechanical design for the first prototype tube was completed recently.

Staff
W. Baumgärtner
H. Budig
G. Dammertz
U. Feißt
P. Grundel
R. Hietschold
G. Hochschild
A. Hornung
B. Jödicke
M. Kuntze
R. Lehm
N. Münch
H. Oppermann
B. Pioscyk
G. Redemann
H. Stickel
R. Vincon
H. Wenzelburger

NET Study Contracts

Availability of the LCT Plant

The experimental phase of the Large Coil Task was successfully completed by opening of the lid of the vacuum vessel on October 9, 87. (Activities are described in M1). Presently all participants are working on the evaluation of the results. A first draft about the assessment of the availability of the LCT plant during the running of the experimental program was submitted to NET.

Staff:
A. Ulbricht
P.N. Haubenreich, ORNL

Study about the NET TF Pancake Test

The final study report about the NET model coil test possibilities was transmitted to NET [1]. The study contract was extended to the following investigations:

1. Test of the OH-conductor together with or in sequence to the TF-conductor (this investigation was proposed by the NET-Team during the pancake meeting in June 1986 and the results of this investigations are included in the final study report for the Cluster and Solenoid Test Facility).
2. Test of the NET-TF-conductor in the existing TOSKA-Facility together with the EU-LCT-coil as a background coil (Twin Test).
3. Test of the EU-LCT-coil at a temperature of 1.8 K up to the limits of the coil and/or conductor. This test should prove not only the operability of large NbTi-TF-coils at this temperature but also the possibility to use a conductor based on the principles of the already tested EU-LCT-conductor for a NET-TF-coil back-up solution.
4. Integration of the 1.8 K EU-LCT-coil test into the Twin Test.

The excellent performance of EU-LCT-coil demonstrated in the LCT test program (Task M1) stimulated ideas to operate the coil at 1.8 K. At this temperature fields from 10 T to 11 T can be obtained. The operation of a large coil comparable with a reactor sized coil is a very interesting goal. Besides this the increasing field at this temperature level stimulated the discussionof a model coil testing facility with only one LCT coil. In a first step the capability of the mechanical system was investigated of withstanding such a load case in single-coil operation. In finite element calculations it was found that a suitable structure will keep the stress levels of the winding and case within acceptable limits. Investigations about shear stress measurement methods described in Task M4 contribute considerably to the confidence that the expected shear stress levels will lead to no damage. Investigations about the electrical and thermohydraulical properties of the coil for high currents are under way. A configuration consisting of a NET model coil and the Euratom LCT coil will be optimized. Final results will be available by mid 88.

[1] J. Erb, A. Günhagen, W. Herz, I. Horvath, K. Jentzsch, P. Komarek, K. Kwasnitza, E. Lotz, S. Malang, C. Marinucci, W. Maurer, G. Nöther, G. Pasztor, A. Peters, A. Roeterdink, C. Sborchia, A. Ulbricht, A. Vogt P. Weymuth, G. Zahn, NET Model Coil test Possibilities, Final Study Report, KfK 4355, November 1987, Kernforschungs-zentrum Karlsruhe.

Staff:
A. Grünhagen
W. Herz
K. Jentzsch
W. Maurer
A. Ulbricht
A. Vogt
G. Zahn

Evaluation of Crack Growth Delay in Multilayer Sheets

Objectives of the contract

Some first- wall (FW) designs which are under discussion for NET make use of brazed connections between cooling tubes or between plates in order to provide a second containment of the coolant. As base material in the physics phase SS 316 L is specified, as a braze BN 5 (NICROBRAZ 30), BN 6, BN 7 (NICROBRAZ 50) have been proposed because of their consistency.

A critical problem in discussing whether brazed tubes may serve as a double containment is the fatigue behavior of small cracks in the tubes, which will exist due to fabrication processes or might arise during operation by overloads caused by plasma disruptions.

Our investigations on fatigue crack growth in brazed layers consist of two parts.

Experimental studies

Crack growth measurements have been performed at two types of specimens (bars and plates) and taking into consideration two different types of brazing.

Theoretical considerations

The mechanism of fatigue crack growth is theoretically described by stress intensity factors, fatigue crack growth in the NET FW is considered and an approximation for an upper limit for the allowable size of an interface crack between brazed coolant tubes is given.

Experimental Results

All specimens had been provided with a starter notch and were exposed to alternate tension and bending loads in a four-point bending machine in order to produce a fatigue-induced crack.

Only in the multilayer bar type specimens (straight crack propagation front) with the higher melting NB 30 brazing solder the brazing seam was penetrated, i.e., the crack could be made to grow into the second sheet.

In the plate type specimens, with the more realistic semi-elliptical surface crack, the crack front could not be made to propagate into the second sheet. All specimens ruptured in the brazing seam, or the crack was stopped in its original direction of propagation perpendicular to the brazing seam, deflected into the brazing seam, but did not stop there.

Crack propagation in brazed sheets made of SS 316 L material was studied. The compounds of two sheets of equal thickness were prepared with two nickel type brazing solders of different melting points. The specimens were available in a bar and a plate form. Of the bar type specimens, five had been prepared with NB30, which melts at 1200°C, and five with NB 50 brazing solder, which melts at 1000°C. In the plate type specimens, three samples of each brazing solder were available.

Numerical results

The fatigue crack growth of an existing crack on the rear part of the FW with a depth of less than 1mm is leading to failure of the structure after 10^4 cycles if the crack is not stopped in the intermediate layer.

Crack propagation at the front side leads to a lifetime of 3 x 10^4 cycles.

If hot spots in the FW with temperatures up to 600°C are admissible an interface crack with a size of up to $2cm^2$ in the intermediate zone can be tolerated. If temperatures in the FW reach 600°C the wall will fail by thermal creep.

Staff:
G. Balzer
E. Diegele
T.Fett
S. Müller

Investigation of the Vacuum and Exhaust Performance of NET

The main objective at present is the simulation of the vacuum performance during dwell time. The intended application of an extended version of the VAKMAP1 code for this purpose proved to be inadequate. To get satisfactory results, the transition period from burntime to dwell time must be treated in more detail. Therefore, the new code under development will allow to investigate in sucessive steps the vacuum performance during burn, transition and dwell times. Besides the gases within the main plasma and the halo, the balance of the gases implanted in the surface layers and the bulk materials of the plasma facing walls are treated.

To define realistic initial conditions for the transition phase the equilibrium conditions of the gas-wall system during burn are determined with a simplified recirculation model. The concentration of the hydrogen isotopes in the material surface layers is limited by preset saturation values. A mixing model is used to calculate the actual fractions of deuterium and tritium implanted.

The transition phase is initiated by stopping fuel injection to the main plasma. This results in a decrease in density of the main plasma and in a corresponding variation of the plasma-wall interaction. If a preset density value is reached, an overall mixing process is initiated within the plasma chamber. In this way, the starting conditions of the subsequent dwell time evacuation process are defined.

For test purposes, representative values are used for all key parameters. These values will be updated later-on on the basis of new results available from the operating fusion devices and other laboratory experiments. At present, the data base in some key areas (e.g. hydrogen-graphite interaction) is still very small.

Upon request of NET, an existing program for the calculation of the gas flow within the exhaust duct from the plasma chamber to the molecular pump was modified for application on an IBM-Personal System/2 computer. Originally, this program was written during development work on VAKMAP1. For given ratios of the emerging gas fractions the program calculates the DT-fraction after recombination at the divertor and for given duct design data the total conductivity of the duct. Furthermore, for a given characteristic of the turbomolecular pump the partial pressures and the total pressure at the gas intake are calculated.

This activity was part of the envisaged strategy aimed at making better use of personal computers in the future. Direct program transfer is guaranted in this way because the computers on both sides are identical.

Staff:
R.A. Müller
F. Engelhardt

CAD Data Exchange between NET and KfK

The design of NET is to a large done by means of computer aided design (CAD) systems. Since NET and KfK use dissimilar CAD systems a neutral CAD data exchange interface IGES (Initial Graphics Exchange Specification) is used for exchange of NET drawing data. Both the NET CAD system MEDUSA

and the KfK CAD system BRAVO3 have IGES pre- and postprocessors which write and read the IGES file. However since the IGES specification is rather ambiguous and the IGES processors are not bug free, it is the objective of the contract to improve the data exchange via IGES between NET and KfK.

A test matrix had been created in the previous step in order to cover all of the MEDUSA elements. The evalution of the IGES files resulting from that test matrix served as a basis for further steps:

- Some MEDUSA elements in particular dimensions were subject of a more thorough analysis.
- A software tool called "Sheet Marker" has been implemented which marks those entities of a MEDUSA sheet which are likely not to be transferred via IGES. This tool covers only those entities which have no direct correspondence in IGES.
- Those entities which theoretically have a correspondance in IGES but nevertheless cause errors in the IGES file have to be treated externally, outside MEDUSA. Thus a software for removal and modification of entities in the IGES file will be developed.
- Both the MEDUSA and the BRAVO3 postprocessors will be analyzed by means of a neutral IGES test library which has been provided by the American National Bureau of Standards.

Staff:
U. Gengenbach
S. Haas
G. Ludwig

Study of a Plasma Exhaust Purification System for NET Based on Catalytic Reduction of Impurities: Phase 1 Conceptual Study

In studies work carried out jointly by the Kernforschungszentrum Karlsruhe (KfK) and Kraftanlagen Heidelberg (KAH) alternative processes for the cleanup of plasma exhaust were assessed with respect to the process requirements for NET.

Altogether seven process concepts were compared under the NET reactor operational conditions normal burn and dwell, carbonization, bakeout and glow discharge. Common to all alternatives is a palladium/silver alloy selective hydrogen permeator, which separates the unburned hydrogen isotopes deuterium and tritium from the fuel ash helium and the hydrogenated as well as non-hydrogenated impurities.

For the recovery of tritium from the bleed gas of the main permeator, i.e. Q2, CQ4, Q2O, CO, CO2, O2, N2 etc. (Q = D,T) and the decontamination of this process gas concepts involving either

- the direct gettering of carbon, nitrogen and oxygen on a hot metal bed followed by a separation of hydrogen and helium via a second permeator or another metal bed,
- the oxidation of all impurities together with residual hydrogen into water and carbon dioxide an oxygen donator solid bed or with oxygen on a noble metal catalyst followed by a combination cryotrap/electrolysis cell or a combination water gas shift reaction with a second permeator or
- the use of selective catalytical reactions for the liberation of deuterium/tritium from water (water gas shift reaction) and hydrocarbons (nickel catalyst) in combination with a second permeator

were examined.

While getters appear attractive because hydrogen isotopes from the impurities are liberated in a single step, problems are expected from the required high temperatures, the large amount of getter needed for high conversion, the potential for getter ignition, the renewal and disposal of spent tritiated getter, etc.

The solid waste problem is mitigated by the oxidation/electrolysis cell option. Important disadvantages of this route are the non-specific oxidation (residual molecular hydrogen, carbon monoxide), the separation water/carbon dioxide, and the high tritium inventory (cryotrap and/or electrolysis cell).

The use of selective catalyst reactions for the recovery of tritium from the impurities in the bleed gas of the main permeator has been investigated at KfK.

According to the KfK process concept water present in the impurity gas stream is decomposed to yield hydrogen on a commercial catalyst using the ater gas shift reaction.

Tritiated methane is cracked on a supported nickel catalyst in combination with a second palladium/silver permeator into carbon and molecular hydrogen at about 500°C. The amount of catalyst required is moderate, it can be further reduced by regeneration of the catalyst.

The selective catalyst process is characterized by low permeation losses, by few and easily controllable process steps, low total gaseous and solid waste, an availability as demanded by the NET process requirements, acceptable inventory and sufficient credibility of funcional predictions to warrant a feasibility study for an extrapolation to NET size dimensions.

The now completed feasibility study supports the choice of a selective catalyst process for NET. in a next step the detailed design of a scaled-up loop experiment will be carried out.

Staff:
Dr. M. Glugla
Dr. R.-D. Penzhorn
Dr. R. Rodriguez
D. Herbrechter (KAH)

CAD Data Exchange for ITER

International collaboration on ITER requires facilities for efficient exchange of CAD data between the partners. NET, Lawrence Livermore Laboratory and Fusion Engineering Center use dissimilar CAD-systems, namely CV-MEDUSA and CV-CADDS 4X. This fact requires the use of a neutral interface for CAD data exchange. Both systems provide such an interface (Initial Graphics Exchange Specification) but its use is not bug free. This is particularly true of complex drawings which will be applicable for ITER. The subject of this contract is to determine the set of entities that can be

transmitted reliably between those two systems. The complementary information i.e.the set of entities that cause problems are catalogued for further analysis.

The project is subdivided into different steps:

a) The first step is to provide to equipment, that means CAD hardware, CAD software including the IGES processors. NET provides access to the MEDUSA system, the CADDS 4X access will be possible at the German Computer vision branch. The connection to LLL and FEDC is realised via public package switching network (X.25).

b) The CAD data exchange requires the establishment and test of procedures for transferring tapes and direct data exchange (via X.25) between LLL, FEDC and NET.

c) The MEDUSA/CADDS 4X fusion drawings are analysed with respect to the elements (e.g. lines, arcs, text, dimensions) that constitute these drawings. The intention is to summarize the relevant entities to be exchanged.

d) To identify which entities cause problems the IGES Pre- and Postprocessors of MEDUSA and CADDS 4X are analysed.

e) For future applications other highlevel data exchange formats are investigated (VDAFS, CAD*I, STEP, SET).

The analysis of Medusa system is in the final stage and the entities of the Medusa system are classified with respect to its usability for transfer purposes. Therefore the main emphasis lies on the analysis of the CADDS 4X system. The result is a classification of the CADDS 4X entity set. The common denominator of those two sets represents the entity set usable for reliable data transfer.

Staff:
W. Reichert
U. Gengenbach
S. Haas

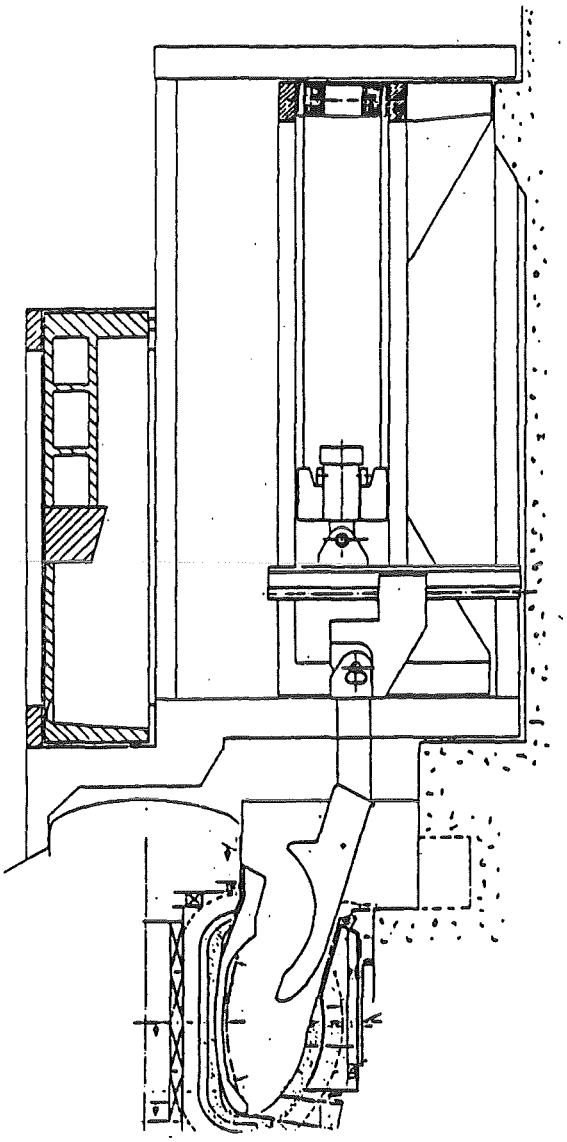

Fig. 75: Blanket Handling Device - Elevation View

NET Blanket Handling Device

Within the frame of the NET contract NET/87-136 KfK started with the investigation of handling concepts for blanket segments which will result in a preliminary specification and pre-design of the required equipment.

In a first step a Requirement Definition Document was elaborated and transmitted to the NET team. To get a basis for the evaluation of a concept which will be pre-designed during 1988, KfK has launched the review of available concepts proposed by CEA and own alternative solutions, The options are studied and compared with respect to safety, reliability, complexity of design, required development, flexibility, required handling time and costs. Results of this review will be documented in an intermediate report and discussed with the NET team in April 88.

One category of solutions are based on the main assembly crane in conjunction with a balancing beam. By means of telescopic rods blanket tilting for replacement will be possible. The balancing might be performed by displacement of attachment points for lifting or by counter weights. More rigid solutions are based on independent handling devices which are movable on rails arranged at the reactor deck. Only lifting will be performed by means of a hoist. Horizontal displacement and blanket tilting are guided (see Fig. 75 and 76).

Safety and reliability are studied taking into account to finalize the handling operations in case of a failure and by estimating the maintenance time for equipment repair. Maintenance times both for component handling and equipment replacement are highly dependent on the different confinement options to avoid the spread of contamination. Considered options are the tight intermediate containment surrounding the complete upper reactor part with all 16 openings, the combination of transport flasks and a contained transfer unit which is attachable in each case to one opening, and the reactor hall with protective steel liners and transport flasks.

The final report in October 88 will include the pre-design of a handling device and auxiliary equipment selected in agreement with the NET team from the reviewed or modified options.

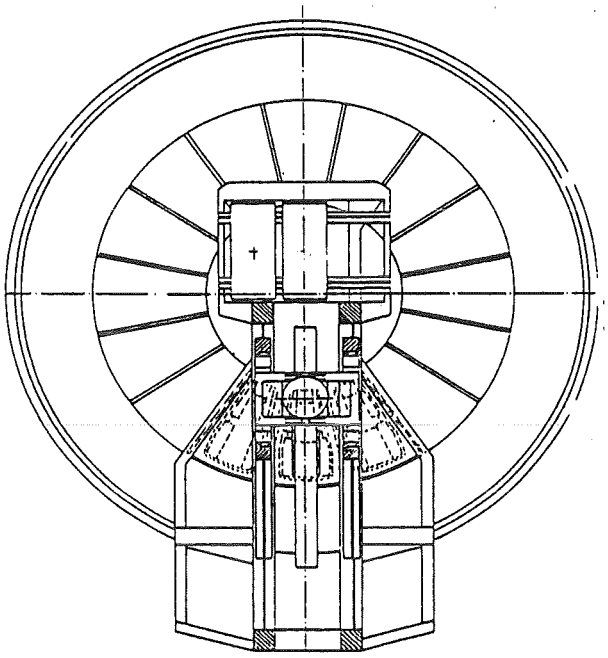

Fig. 76: Blanket Handling Device - Plan View

Staff
B. Haferkamp
J. Hübener
W. Link
A. Suppan

Appendix I: Table of Fusion Technology Contracts

Task Code No.	Title	KfK Departments
B1	Blanket Design Studies	IMF III, INR, IRB, IT
B 2	Development of Computational Tools for Neutronics	INR
B6	Corrosion of Structural Materials in Flowing Pb-17Li	IMF I, IMF II
B 6.3	Fatigue of Structural Material in Pb-17Li	IMF I, IMF II
B9	Tritium Extraction from Liquid Pb-17Li by the Use of Solid Getters	IT
B 11-16	Development of Ceramic Breeder Materials	IMF I, IMF III, INR, IRCH
B 15.3	End of Life of Solid Breeding Materials in Fast Neutron Flux	IMF I, IMF III, INR
M1	The Large Coil Task (LCT)	ITP
M 3	Development of High Field Composite Conductors	ITP
M 4	Superconducting Poloidal Field Coil Development	ITP
M 8	Design and Construction of a Poloidal Field Coil for TORE SUPRA as NET-Prototype Coil	ITP
M 9	Structural Materials Fatigue Characterization at 4 K	ITP
M 12	Low Electrical Conductivity Structures Development	IMF IV, ITP
MAT 1.6	Development and Qualification of Type 1.4914 Base Metal Properties	IMF II
MAT 1.9	Pre- and Post-Irradiation Fatigue Properties of 1.4914 Martensitic Steel	IMF II
MAT 1.11	Post-Irradiation Fracture Toughness of Type 1.4914 Martensitic Steel	IMF II
MAT 2.2	In-Pile Creep-Fatigue Testing of Type 316 and 1.4914 Steels	IMF II, IMF III
MAT 6/ MAT 13	Ceramics for First-Wall Protection and for RF Windows	IMF I
MAT 9.2	Investigation of Fatigue Under Dual Beam Irradiation	IMF II
MAT 18	Development of Low Activation Ferritic-Martensitic Steels	IMF II
N1	Design Study of Plasma Facing Components	INR, IRB, IRE
N2	Shield Design Studies	IMF III
N3	Development of Procedures and Tools for Structural Design Evaluation	IMF IV
N5	Development of Theory and Tools for Evaluation of Magnetic Field Effects on Liquid-Metal Breeder Blankets	IRB
N6	Studies of Pebble Beds of Ceramic Compounds	INR

RM1	Background Studies on Remote Maintenance	IT
RM2	Mechanical Components Assembly	IT
RM 3	Handling Equipment for In-Vessel Components	IDT, IRE, IT
S+E 4.1.2	Safety Aspects of the Cryosystem	IRE
S+E 4.1.3	Safety Aspects of Superconducting Magnets	IDT, IRE, ITP
S+E 5.2.2	Behaviour of Gaseous Tritium in the System Plant/Soil	HS
S+E 5.4	Overall Plant Accident Scenarios for NET	IRE
S+E 5.5	Development of Safety Guidelines for the Design of NET	IRE
S+E 6	Licensing Activities	PKF-PL
S+E 7	Long Term Studies	INR
T 6	Industrial Development of Large Components for Plasma Exhaust Pumping	IT
T 7	Optimization of Cryogenic Vacuum Pumping of Helium	IT
T 10 A	Plasma Exhaust Purification by Means of Cyrosorption on Molecular-Sieves or Alternative Adsorbents	IRCH
T 10 C	Plasma Exhaust Gas Purification by Use of Hot-Metal Getters	IRCH
T 10 E	Adsorption of DT on Heated Metal Beds other than Uranium	IRCH
T 10 H	Catalyst Development Exhaust Purification Process	IRCH
Development of ECRH Power Sources at 150 GHz (This task is part of the Fusion Physics Programme of the EC.)		IDT, IK

Appendix II: Table of NET Contracts

Theme	Contract No.	Working Period
Availability of the LCT Plant	210/85-9/FU-D/NET	10/85 - 12/87
Evaluation of Crack Growth Delay in Multilayer Sheets	253/86-11/FU-D/NET	11/86 - 09/88
Simulation of the Vacuum Performance of NET-DN	254/86-11/FU-D/NET	10/86 - 12/87
CAD Data Exchange between NET and KfK	265/87-3/FU-D/NET	03/87 - 09/88
Study of a Plasma Exhaust Purification System for NET based on Catalytic Reduction of Impurities: Phase 1 Conceptual Study	272/87-8/FU-D/NET	10/87 - 03/88
NET Blanket Handling Device	282/87-10/FU-D/NET	11/87 - 10/88

Appendix III: KfK Departments contributing to the Fusion Project

Kernforschungszentrum Karlsruhe GmbH
Postfach 3640
D-7500 Karlsruhe 1
Telefax/Telecopies (0) 07247/825070
Federal Republic of Germany

Telephone (07247) 82-1
Telex 7 826 484

KfK Department	KfK Institut/Abteilung	Director	Ext.
Central Safety and Security Department	Hauptabteilung Sicherheit (HS)	Prof. Dr. H. Kiefer	2660
Institute for Data Processing in Technology	Institut für Datenverarbeitung in der Technik (IDT)	Prof. Dr. H. Trauboth	5700
Institute for Nuclear Physics	Institut für Kernphysik II (IK)	Prof. Dr. A. Citron	3502
Institute for Materials and Solid State Research	Institut für Material- und Festkörperforschung (IMF)	I. Prof. Dr.W. Dienst II. Dr. K. Anderko III. Prof. Dr.K. Kummerer IV. Prof. Dr. D. Munz	2887 2902 2518 4815
Institute for Neutron Physics and Reaktor Engineering	Institut für Neutronenphysik und Reaktortechnik (INR)	Prof. Dr. G. Keßler	2440
Institute for Reactor Components	Institut für Reaktorbau-elemente (IRB)	Prof. Dr.U. Müller	3450
Institute for Radiochemistry	Institut für Radiochemie (IRCH)	Prof. Dr. H.J. Ache	3200
Institute for Reactor Development	Institut für Reaktor-entwicklung (IRE)	Prof. Dr. D. Smidt	2550
Central Engineering Department	Hauptabteilung Ingenieur-technik (IT)	Dr. H. Rininsland	3000
Institute for Technical Physics	Institut für Technische Physik (ITP)	Prof. Dr. P. Komarek	3500

Appendix IV: Fusion Project Management Staff